DIFFRACTIVE PHOTOPRODUCTION OF HEAVY VECTOR MESONS AT HERA

DISSERTATION

zur Erlangung des Doktorgrades
des Fachbereichs Physik
der Universität Hamburg

vorgelegt von

PETRA MERKEL

AUS HAMBURG

II. Institut für Experimentalphysik
Universität Hamburg

Hamburg
1999

Gutachter der Dissertation:	Prof. Dr. B. Naroska Prof. Dr. W. Bartel
Gutachter der Disputation:	Prof. Dr. B. Naroska Prof. Dr. A. Wagner
Datum der Disputation:	27.10.1999
Dekan des Fachbereichs Physik und Vorsitzender des Promotionsausschusses:	Prof. Dr. F. W. Büßer

Abstract

Diffractive vector meson production is described on the one hand within the phenomenological framework based on Regge theory, and on the other hand by perturbative QCD calculations. Light vector mesons in the photoproduction regime (where no hard scale is present) agree well with non-perturbative Regge based descriptions. Perturbative effects are measured in the presence of a hard scale for light and for heavy vector mesons. The question arises whether in the case of J/ψ and Υ photoproduction the large mass of the quarks in the mesons provides a sufficiently hard scale in order to apply perturbative QCD.

The aim of this thesis is to clarify this question. In the case of the J/ψ, the energy dependence of the cross section, its t dependence (where t is the four-momentum transfer at the proton vertex), and the energy dependence of the t dependence are measured. The parameters of the exchanged trajectory in the diffractive process – the *pomeron trajectory* – is determined. Finally, the Υ photoproduction cross section is extracted.

All these measurements of diffractive heavy vector meson photoproduction at HERA show good agreement with calculations in perturbative QCD as well as with results from Regge based models under the assumption of a second *hard* pomeron. The exchange of just one *soft* pomeron can be ruled out.

Kurzfassung

Diffraktive Vektormeson Produktion wird einerseits beschrieben im Rahmen phänomenologischer Modelle, die auf der Regge Theorie beruhen, andererseits durch perturbative QCD Rechnungen. Leichte Vektormesonen in Photoproduktion (wo keine harte Skala vorhanden ist) stimmen gut mit nicht perturbativen Vorhersagen Regge basierter Modelle überein. In Gegenwart harter Skalen werden perturbative Effekte sowohl für leichte als auch für schwere Vektormesonen gemessen. Daher erhebt sich die Frage, ob im Fall der J/ψ und der Υ Photoproduktion die große Masse der Quarks in den Mesonen bereits eine genügend harte Skala zur Verfügung stellen, um perturbative QCD anwenden zu können.

Das Ziel dieser Arbeit ist die Klärung dieser Frage. Im Fall des J/ψ wurde die Energieabhängigkeit des Wirkungsquerschnitts, seine t-Abhängigkeit (wobei t der Impulsübertrag am Protonvertex ist) sowie die Energieabhängigkeit der t-Abhängigkeit gemessen. Die Parameter der ausgetauschten Trajektorie in dem diffraktiven Prozeß – die *Pomeron Trajektorie* – wurden erstmals mit den Daten eines einzigen Experiments bestimmt. Schließlich wurde der Υ Photoproduktions Wirkungsquerschnitt extrahiert.

Die Messung all dieser verschiedenen Gesichtspunkte diffraktiver schwerer Vektormeson Photoproduktion bei HERA zeigt gute Übereinstimmung mit Rechnungen in perturbativer QCD und mit Ergebnissen Regge basierter Modelle, unter der Annahme eines zweiten. *harten*, Pomerons. Der Austausch ausschließlich eines *weichen* Pomerons kann ausgeschlossen werden.

Contents

1 Introduction **1**

2 Heavy Vector Meson Production **4**

2.1 HERA Kinematics 4

2.1.1 Photoproduction Regime 6

2.1.2 Reconstruction of Kinematic Variables 7

2.2 Regge Theory and the Vector Meson Dominance Model 8

2.2.1 Soft Pomeron Model 11

2.2.2 Two Pomeron Model 13

2.2.3 BFKL Pomeron 13

2.3 Perturbative QCD Calculations 14

2.3.1 Differences between J/ψ and Υ Production 16

2.4 Monte Carlo Models 19

2.4.1 DIFFVM 19

2.4.2 LPAIR 20

3 The H1 Detector at HERA **22**

3.1 Positron-Proton Collisions at HERA 22

3.2 The H1 Detector 23

3.2.1 Tracking System 23

3.2.2 Central Muon Detector 27

3.2.3 Liquid Argon Calorimeter 28

3.2.4 Backward Calorimeter 29

3.2.5 Forward Detectors 30

3.2.6 Luminosity System 31
3.3 Trigger Scheme 31
3.3.1 First Trigger Level L1 32
3.3.2 Second Trigger Level L2 35
3.3.3 Fourth Trigger Level L4 36
3.3.4 Fifth Trigger Level L5 39
3.4 Muon Identification 40
3.4.1 Muon Identification in the LAr Calorimeter 41
3.4.2 Muon Identification in the Instrumented Iron 42
3.4.3 Muon Selection 43

4 Selection of Diffractive J/ψ Mesons **45**
4.1 Selection of Diffractive J/ψ Events 45
4.1.1 Selection of Diffractive Events 45
4.1.2 Run Selection 46
4.1.3 Luminosity 46
4.1.4 Kinematic Region 48
4.1.5 Background 50
4.2 Selected Data Set 51
4.3 Acceptance and Efficiencies 54
4.3.1 Trigger Efficiency 56
4.3.2 Vertex Finding and Track Reconstruction 58
4.3.3 Muon Identification 58
4.3.4 Forward Tagging 60
4.3.5 Summary of Efficiencies 62
4.4 Systematic Uncertainties 62

5 Results for Diffractive J/ψ Production **67**

5.1 Cross Section Results on Elastic J/ψ Production 67

5.1.1 Correction of the Data 67

5.1.2 Extraction of the Elastic J/ψ Cross Section 70

5.1.3 Elastic J/ψ Cross Section as a Function of $W_{\gamma p}$ 71

5.2 The t Distribution 77

5.2.1 Slope Parameter b for Elastic Scattering of J/ψ Mesons 77

5.3 Regge Trajectory for Elastic J/ψ Production 86

5.3.1 Extraction of $d\sigma/dt$ 86

5.3.2 Regge Trajectory 88

5.4 Summary of J/ψ Results 90

6 Diffractive Υ Production **93**

6.1 Selected Data Set 93

6.2 Efficiencies and Systematic Errors 95

6.3 Cross Section 98

6.4 Summary of Υ Results 103

7 Summary and Conclusions **105**

A Detailed Listing of Track Cuts **108**

A.1 Track Selection 108

A.2 Muon Track Selection 109

List of Figures **110**

List of Tables **113**

Bibliography **114**

Chapter 1

Introduction

The understanding of the fundamental forces and the elementary particles is the subject of the field of high energy physics. Within the last 20 years the *Standard Model* has been developed and tested in a multitude of experiments. It provides a satisfactory description of all those processes measured in strong, weak and electro-magnetic interactions, for which it is expected to work.

A special type of interactions, so-called *diffractive* processes have been analysed in hadron-hadron collisions in pre-HERA days. Diffractive events showed many features characteristic of optical diffraction and were described phenomenologically in the framework of Regge theory by the t-channel exchange of an object called *pomeron*. These ideas were successfully applied to diffractive events in photoproduction at fixed target experiments and at HERA.

Diffractive interactions at HERA are investigated both in inclusive and exclusive processes. The measurements deal with e.g. the diffractive structure function, the properties of the hadronic final state or the exclusive production of vector mesons. In the analysis of diffractive heavy vector meson production particularly two features provide an ideal testing ground for diffraction and for perturbative Quantum Chromo Dynamics (pQCD): On the one hand, only pomeron and no meson exchange occurs in J/ψ and Υ (as well as in ϕ) production. This is due to the different quark contents of these vector mesons and the proton (Zweig's rule). On the other hand, the large mass of the constituent quarks provides the hard scale needed for perturbative calculations. A significant amount of theoretical work has been carried out in the last years to understand charmonium production in the framework of QCD, where in a simple ansatz the pomeron is modelled as a system of two gluons.

Photoproduction of ρ mesons at HERA is measured to be well described by the same parameterization of the pomeron as extracted from total cross section measurements. For example the energy dependence of the ρ cross section (see figure 1.1) shows the $\sigma_{\gamma p} \propto W_{\gamma p}^{0.22}$ behaviour as predicted, with $W_{\gamma p}$ being the centre-of-mass energy of the photon-proton system. ω and ϕ photoproduction is not yet precisely measured at HERA energies. Nevertheless, it is found to be compatible with the Regge based models (see figure 1.1).

On the other hand, the energy dependence of the J/ψ photoproduction cross section is measured to be much steeper than in the case of the light vector mesons ($\sigma_{\gamma p} \propto W_{\gamma p}^{\sim 0.8}$, see figure 1.1).

This is interpreted as a signature for perturbative QCD mechanisms. Furthermore, the behaviour of the ρ production cross section in presence of a hard scale, such as the momentum transfer either at the electron vertex, Q^2, or at the proton vertex, t, shows the transition between the non-perturbative and the perturbative regimes. The study of diffractive J/ψ photoproduction might help to clarify the question, whether the high mass of the J/ψ alone – in absence of another hard scale – allows the application of perturbative calculations, or whether non-perturbative mechanisms are still important.

The subject of this thesis is diffractive J/ψ and Υ production, placing particular emphasis on the *elastic* processes, $ep \to eJ/\psi p$ and $ep \to e\Upsilon p$. In the case of Υ production the mass of the b quark should be large enough to allow the process to be fully calculable in perturbative QCD. The comparison of diffractive J/ψ and Υ meson photoproduction can therefore provide an additional probe of the transition region and the universality of the pQCD calculations for heavy vector meson production.

The focus of the measurements presented here is in particular the γp cross section of J/ψ and Υ mesons. The total cross section for elastic Υ meson production is measured, while the higher statistics for J/ψ allow one to study in detail the $W_{\gamma p}$ and the t dependences which can distinguish between the models assuming a pure soft process and the pQCD predictions.

Measuring the exchanged trajectory in terms of Regge theory is a very direct way to study whether elastic J/ψ photoproduction is driven by perturbative or non-perturbative mechanisms. The measurement as presented here is the first measurement of this kind using data from one single experiment only and therefore avoiding normalization problems and different treatment of the separation of the $\gamma p \to J/\psi p$ process from other, contaminating processes.

This thesis is organized as follows: In chapter 2 an introduction to HERA kinematics in general and the reconstruction of variables specifically important for this analysis are given. Afterwards the Monte Carlo generator programs used to correct the data for acceptance and efficiency losses are described. In chapter 3 the electron-proton accelerator HERA together with the main components of the H1 detector are discussed. In addition the trigger scheme as relevant for this analysis and two algorithms for muon identification are given. The identified muons are used to reconstruct the J/ψ via its muonic decay, $J/\psi \to \mu^+\mu^-$. The more technical part of the J/ψ analysis, namely the selection chain, efficiency studies and systematic errors, are discussed in chapter 4. The results on the $W_{\gamma p}$ and t dependence of the cross section, the $W_{\gamma p}$ dependence of the elastic slope parameter, the proton dissociative slope parameter and the exchanged Regge trajectory are presented and discussed in chapter 5. The results are compared with different theoretical predictions, shedding light on the question whether perturbative or non-perturbative effects are dominating.

The Υ photoproduction cross section measurement is performed in a similar way to the J/ψ analysis. However, some small changes are made to account for the different purity of the signal. The selection of Υ mesons, efficiencies and systematic errors are presented in chapter 6. The resulting γp cross section is compared to other measurements and to pQCD predictions. Finally, in chapter 7, an overall summary is given and conclusions are drawn.

In figure 1.1 the total photoproduction cross section, σ_{tot}, is shown, together with the cross sections of various vector mesons (ρ, ω, φ and J/ψ) in photoproduction, $\sigma(\gamma p \to V p)$, for data from fixed target experiments and from HERA, including only results prior to the present analysis.

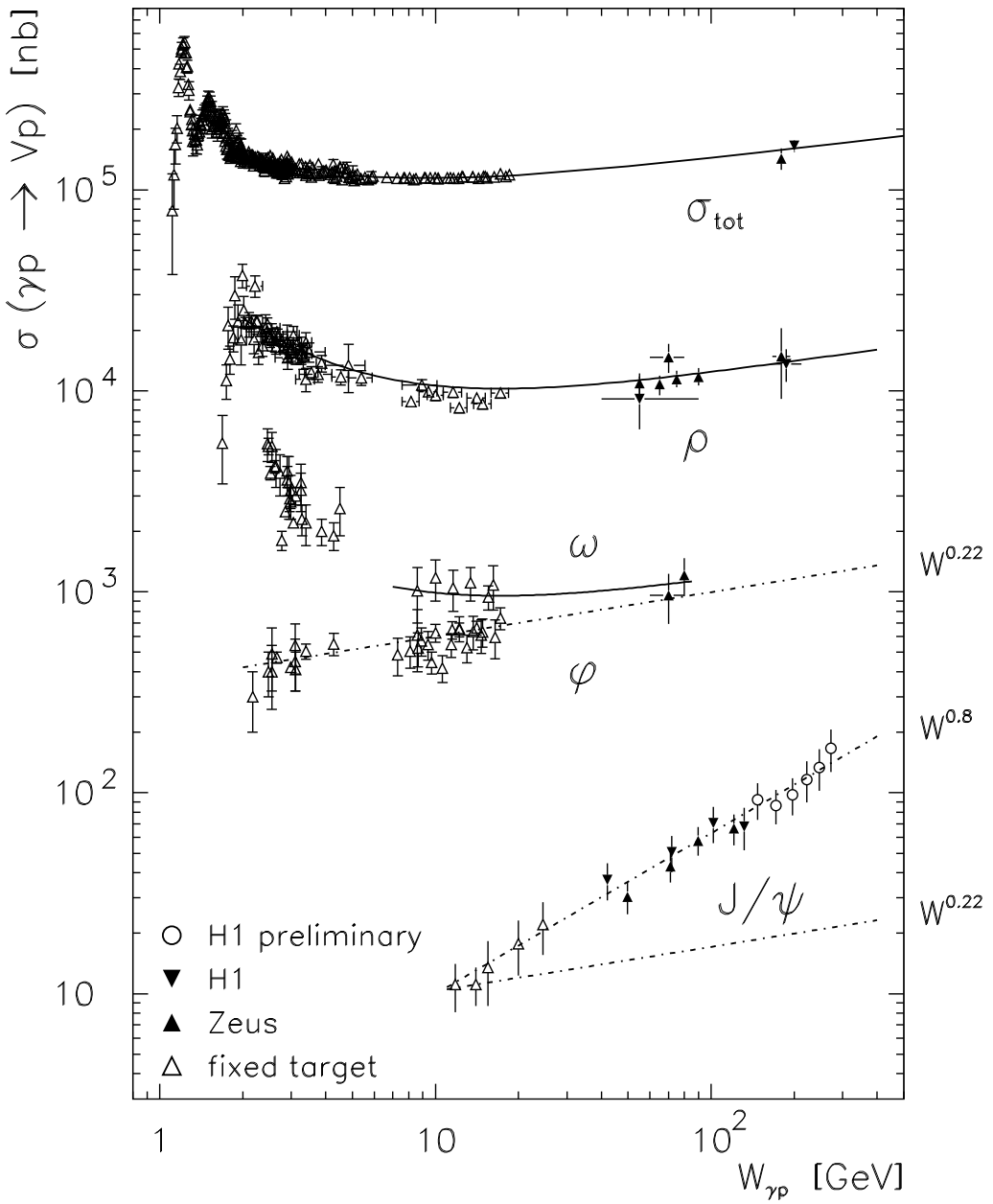

Figure 1.1: Compilation of $\sigma_{\gamma p}^{tot}$ and $\sigma_{\gamma p}$ for various vector mesons prior to the present analysis. The full lines are fits to the total photoproduction cross section, the elastic ρ, and the elastic φ cross section, using Regge parameterizations and assuming single pomeron exchange [1, 2]. The dashed lines visualize a certain energy dependence as indicated on the right hand side.

Chapter 2

Heavy Vector Meson Production

In this chapter, after a brief introduction of HERA kinematics, the diffractive production of heavy vector mesons is discussed in the light of several theoretical models. The basic ideas of these models are briefly explained and predictions for the behaviour of J/ψ and Υ cross sections as functions of kinematic variables are described. Finally Monte Carlo models, which are used to correct the data for acceptances and inefficiencies, are introduced. The term "diffractive" will be used in this thesis both, for pomeron exchange and for the event signature, which is determined by nothing but the decay leptons of the vector meson in the main detector. A more exhaustive overview of J/ψ history and physics can be found in [3] and [4] and of the specific subject of the pomeron in [5] and [6].

2.1 HERA Kinematics

In the basic deep inelastic scattering (DIS) process at HERA the incoming positron couples to an electroweak current, which probes the structure of the proton. Generic diagrams for a) neutral current (NC) and b) charged current (CC) processes are sketched in figure 2.1. The two processes

$$\text{a)} \quad e^{\pm}p \to e^{\pm}X \;\; (\text{NC}) \qquad \text{and} \qquad \text{b)} \quad e^{\pm}p \to \nu_e(\bar{\nu}_e)X \;\; (\text{CC}) \tag{2.1}$$

can be distinguished by the final state electron (NC) or neutrino (CC). Due to the high masses of the Z and W bosons, the exchange of photons is the dominant process. Z^0 exchange is suppressed by a factor $\sim Q^2/(Q^2+M_Z^2)$, and is therefore negligible in photoproduction ($Q^2 \approx 0$) and DIS at low Q^2. Also due to the propagator term charged current contributions are negligible.

With k and p being the four-momenta of the incoming lepton and proton and E_e and E_p their energies, the total centre-of-mass energy $\sqrt{s}$ is given by

$$s = (p+k)^2 \simeq 4 \cdot E_e \cdot E_p \tag{2.2}$$

neglecting the lepton and proton masses. The square of the four-momentum transfer at the electron vertex is given by

$$Q^2 = -q^2 = -(k-k')^2\,, \tag{2.3}$$

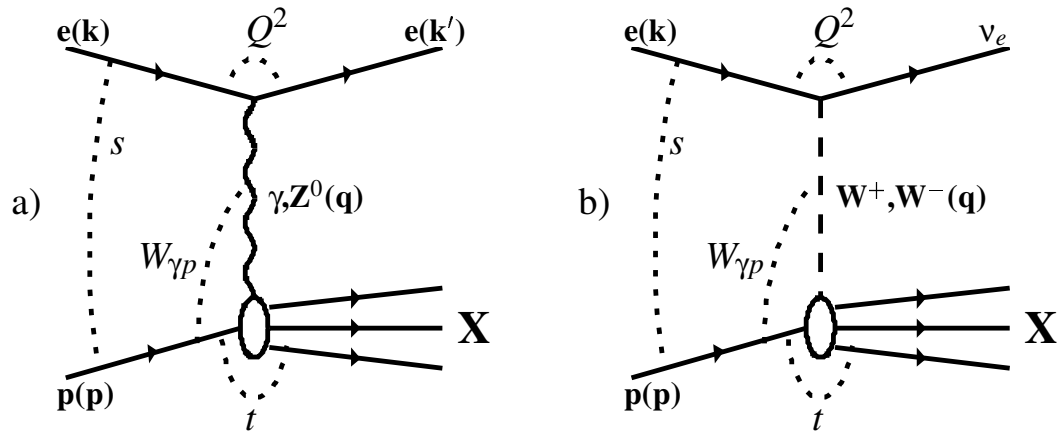

Figure 2.1: Generic graphs for ep collisions: a) neutral current (NC) and b) charged current (CC) deep inelastic ep scattering. The particles' four-momenta are given in brackets.

with q being the four-momentum of the exchanged gauge boson, and k and k' denoting the four-momenta of the incoming and scattered lepton.

At fixed centre-of-mass energy $\sqrt{s}$, the DIS process can be described by two Lorentz scalars. Choosing the dimensionless Bjorken scaling variable x and the inelasticity y as follows:

$$x = \frac{-q^2}{2 \cdot p \cdot q}, \tag{2.4}$$

$$y = \frac{q \cdot p}{k \cdot p}, \tag{2.5}$$

and neglecting the masses of the lepton and the proton, Q^2, x and y are related via

$$Q^2 = x \cdot y \cdot s. \tag{2.6}$$

x denotes the fraction of the proton momentum carried by the parton which couples to the electroweak current, and y corresponds to the fraction of electron energy transferred to the proton in its rest frame.

The square of the invariant mass $W^2_{\gamma p}$ of the hadronic final state X is related to x and Q^2 or y and Q^2 by momentum conservation at the proton vertex:

$$W^2_{\gamma p} = (p+q)^2 = Q^2 \cdot \left(\frac{1}{x} - 1\right) + m_p^2 = y \cdot s - Q^2 + m_p^2. \tag{2.7}$$

Three kinematic regions can be defined: for $x \to 1$ *elastic scattering* takes place ($W^2_{\gamma p} \to m_p^2$); in the limit $Q^2 \to 0$ almost real photons are radiated off the lepton defining the *photoproduction* region; while large Q^2 ($Q^2 \gtrsim 1\,\mathrm{GeV}^2$) and $W^2_{\gamma p} \gg m_p^2$ is the domain of *deep inelastic scattering*.

In the context of diffractive processes a further variable is introduced, the square of the momentum transfer at the proton vertex, t, which is defined as

$$|t| = (p - p')^2, \tag{2.8}$$

with p and p' denoting the four-momenta of the incoming and the scattered proton. In the case of diffractive vector meson production (see figure 2.2) t can be reconstructed via

$$|t| = -t_{min} + \overrightarrow{p_t}^2_{,p} \simeq (\overrightarrow{p_t}_{,e} + \overrightarrow{p_t}_{,V})^2 \,, \tag{2.9}$$

where $\overrightarrow{p_t}_{,p}$, $\overrightarrow{p_t}_{,e}$ and $\overrightarrow{p_t}_{,V}$ are the momentum components transverse to the beam direction of the final state proton, the positron and the vector meson. t_{min} is the minimal momentum transfer which is needed for the reaction to take place. With m_p denoting the proton mass, the minimal momentum transfer in the case of elastic vector meson production – i.e. the scattered proton stays intact – is given by

$$t_{min} = m_p^2 \left(\frac{Q^2 + M_V^2}{W_{\gamma p}^2} \right)^2 \simeq \left(\frac{M_V}{W_{\gamma p}} \right)^4 . \tag{2.10}$$

t_{min} is of the order of $10^{-6}(10^{-4})\,\mathrm{GeV}^2$ for $J/\psi\,(\Upsilon)$ photoproduction at $W_{\gamma p} = 100\,\mathrm{GeV}$.

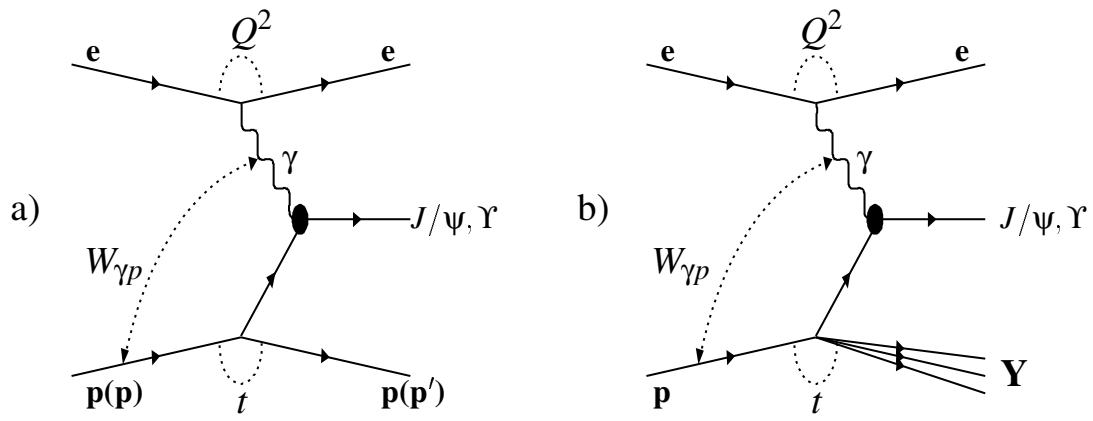

Figure 2.2: Generic graphs for a) elastic and b) proton dissociative vector meson production in ep collisions.

2.1.1 Photoproduction Regime

The analysis presented here is carried out in the *untagged* photoproduction regime ($Q^2 \lesssim 1\,\mathrm{GeV}^2$, $\langle Q^2 \rangle = 0.05\,\mathrm{GeV}^2$), i.e. the scattered positron is not measured in the detector. At such low momentum transfer Q^2 the electrons emit quasi-real photons, which then interact with the proton. The cross sections for the electroproduction ($ep \to eXp$) and the photoproduction ($\gamma p \to Xp$) processes are related via the improved Weizsäcker Williams Approximation (WWA) [7]-[10]. The electron–proton cross section σ_{ep} factorises into the photon–proton cross section $\sigma_{\gamma p}$ and the flux of transversely polarized photons Γ_T:

$$\sigma_{ep} = \int_{y_{min}}^{y_{max}} dy \int_{Q^2_{min}}^{Q^2_{max}} dQ^2 \cdot \Gamma_T(y, Q^2) \cdot \sigma_{\gamma p}(y, Q^2) \qquad \text{with} \tag{2.11}$$

$$\Gamma_T(y,Q^2) = \frac{\alpha_{em}}{2\pi y Q^2} \cdot \left(1 + (1-y)^2 - 2m_e^2 \frac{y^2}{Q^2}\right) \qquad \text{and} \tag{2.12}$$

$$Q^2_{min} = m_e^2 \cdot \frac{y^2}{1-y}\,. \tag{2.13}$$

Defining the integrated flux of transversely polarized photons off the electron as

$$\mathcal{F} = \int_{y_{min}}^{y_{max}} dy \int_{Q^2_{min}}^{Q^2_{max}} dQ^2 \cdot \Gamma_T(y,Q^2)\,, \tag{2.14}$$

a point $(\langle y\rangle, \langle Q^2\rangle)$ – or $(\langle W\rangle, \langle Q^2\rangle)$ – can be found for which

$$\sigma_{ep} = \mathcal{F} \cdot \sigma_{\gamma p}(\langle W\rangle, \langle Q^2\rangle) \tag{2.15}$$

is valid. Equation 2.15 is later on used to extract the photoproduction cross section from the measured electroproduction cross section in order to compare the measurement with theoretical predictions calculated for photoproduction processes.

2.1.2 Reconstruction of Kinematic Variables

The lack of knowledge about the scattered positron also influences the reconstruction of the momentum transfer at the proton vertex, t (compare equation 2.9). Due to the unmeasured $\overrightarrow{p_t}_{,e}$ only a rather poor resolution in t is achieved (see figure 2.3 b and e), while the reconstruction of $\overrightarrow{p_t}_{,V}$ is significantly better (see figure 2.3 a and d).

The reconstruction of the γp centre-of-mass energy, $W_{\gamma p}$, is performed with information from the hadronic final state only, the so-called Jacquet-Blondel [11] method. First y is reconstructed via

$$y = \frac{\Sigma_{had}(E - p_z)}{2E_e}\,, \tag{2.16}$$

where in the numerator the difference between energy and longitudinal momentum is summed for the hadronic final state, while the denominator contains twice the incoming electron beam energy (55 GeV). $\Sigma_{had}(E-p_z)$ is calculated from central tracks and cells in the liquid Argon (LAr) calorimeter and the backward calorimeter, a "spaghetti" type lead-scintillating fibre calorimeter (SpaCal). Tracks starting in inner Central Jet Chamber (CJC1) and fitted to the primary event vertex, with a relative error on the transverse momentum measurement $\sigma_{p_t}/p_t < 0.05$ and transverse momentum $p_t > 100\,\text{MeV}$, are taken into account assuming they are pions. For particles with transverse momenta above 300 MeV, energy deposits in calorimeter cells "behind" the tracks are ignored in order to avoid double counting. The hadronic final state mass $W_{\gamma p}$ is then calculated from y:

$$W_{\gamma p} = \sqrt{y \cdot s - Q^2 + m_p^2}\,. \tag{2.17}$$

The inelasticity y has a mean value of $\langle y \rangle \approx 0.07$ for elastic J/ψ events passing the selection chain described in chapter 4, and the mean Q^2 is $\langle Q^2 \rangle \approx 0.05\,\mathrm{GeV}^2$. The resolution in $W_{\gamma p}$ is shown in figure 2.3 c and f.

The quality of the kinematic reconstruction is displayed in figure 2.3, where reconstructed quantities after the full detector simulation (subscript "rec") are compared to the generated values (subscript "gen"), using the DIFFVM Monte Carlo program, which simulates diffractive J/ψ production (section 2.4.1). In figures a-c, the correlations between reconstructed and generated $p^2_{t,\psi}$, $|t|$ and $W_{\gamma p}$ are shown. In figures d-f the relative resolution in these three variables is given. It is about 16 % in $|t|$ and about 1 % in $W_{\gamma p}$. The quality of the $|t|$ resolution improves with $|t|$, from about 25 % for $|t| < 0.1\,\mathrm{GeV}^2$ to 14 % for $0.5 < |t| < 1\,\mathrm{GeV}^2$. The chosen bin sizes in the analyses later on will be at least two times larger than the resolution.

The hadronic final state mass $W_{\gamma p}$ and the polar angle of the vector meson are strongly correlated. This correlation is transferred to the vector meson's decay muons. In figure 2.4 the polar angle of the decay muons of J/ψ (top row) and Υ (bottom row) mesons is shown from simulated DIFFVM events. The ϑ_μ distributions are given for three different regions in $W_{\gamma p}$. The correlation between both variables can clearly be seen. The chosen acceptance range in the central part of the tracking system ($20^\circ \leq \vartheta_\mu \leq 160^\circ$ for J/ψ and $20^\circ \leq \vartheta_\mu \leq 165^\circ$ for Υ) is marked with vertical lines in each plot of figure 2.4. It limits the accessible range in $W_{\gamma p}$.

2.2 Regge Theory and the Vector Meson Dominance Model

Diffractive processes can be described within the framework of *Regge theory* [12, 13]. It is expected to be applicable if $W^2_{\gamma p}$ is much larger than any other scale involved, such as Q^2, t or quark masses. While Regge-inspired models [16, 17] are able to describe the total photoproduction cross section at HERA energies, discrepancies between the first HERA results on the proton structure function at very small x [14] and on elastic J/ψ photoproduction [15] and the predictions of the Donnachie-Landshoff [18] model based on Regge theory were found. In particular, in the case of J/ψ photoproduction, the energy dependence of the cross section is measured to be much steeper than predicted. Also no experimental evidence exists so far for the energy dependence of the elastic slope parameter, which defines the t dependence of the cross section, as postulated in the soft pomeron model by Donnachie and Landshoff. Models based on pQCD were discussed as an alternative.

The analysis presented here is performed in order to shed further light on the question of the importance of *soft* and *hard* mechanisms in diffractive J/ψ photoproduction. A process is said to be hard if it is driven by parton interactions and is at least in principle calculable in perturbative QCD. In this sense the Donnachie-Landshoff model is a soft model.

"Regge behaviour should not be understood as a substitute for perturbative QCD, but as a constraint on it, and an important task is to understand better how the two coexist." [19]

In the context of the Vector Meson Dominance Model (VDM, [20, 21, 22]) the photon is described as a quantum mechanical superposition of the bare QED photon state $|\gamma_{QED}\rangle$ and a hadronic state $|h\rangle$:

$$|\gamma\rangle = |\gamma_{QED}\rangle + |h\rangle\,, \tag{2.18}$$

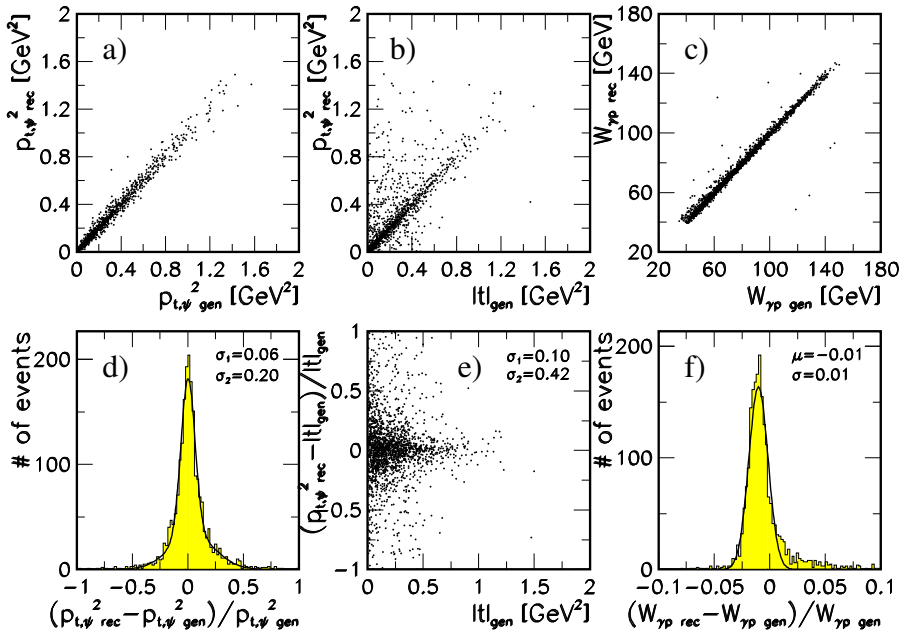

Figure 2.3: Reconstruction of kinematic variables determined from simulated DIFFVM J/ψ events, passing the selection chain described in chapter 4: the square of the transverse momentum of the J/ψ, $p^2_{t,\psi}$ (a,d), the momentum transfer at the proton vertex, $|t|$ (b,e) and the photon-proton centre-of-mass energy, $W_{\gamma p}$ (c,f). In the top row the correlation between generated and reconstructed variables is shown, while in the bottom row the resolution is shown together with the results from fitting one (f) or two (d,e) Gaussians to the data. In e) the resolution is displayed as a function of $|t|_{gen}$.

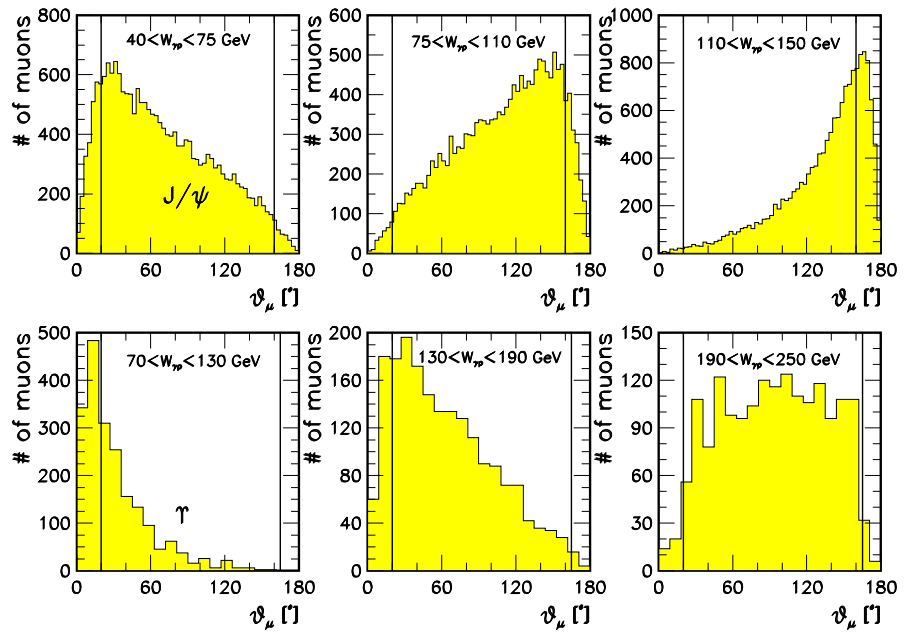

Figure 2.4: Correlation between $W_{\gamma p}$ and polar angle ϑ_μ for simulated elastic J/ψ events (DIFFVM) (top row) and Υ (bottom row) events. Shown is the polar angle of the decay muons for three different ranges in $W_{\gamma p}$. The vertical lines show the ϑ region analysed.

where $|h\rangle$ should have the same additive quantum numbers as the photon, which is the case for vector mesons ($J^{PC} = 1^{--}, Q = B = S = 0$):

$$|h\rangle = \sum \frac{e}{\gamma_V} |V\rangle , \tag{2.19}$$

with γ_V being the VDM coupling constant given by $(\frac{e}{\gamma_V})^2 = \frac{3\Gamma_{ee}}{\alpha_{QED} m_V}$, where Γ_{ee} and m_V are the electronic width and the mass of the vector meson. γ_V is assumed to be Q^2 independent and gives the probability for the transition of the photon to the vector meson. The justification for this picture was given by Ioffe [23], who argued that a photon can fluctuate also into a $q\bar{q}$ pair like it can fluctuate into an e^+e^- pair.

The sum in equation 2.19 is only performed over the diagonal elements ($\gamma^{(*)} \to V^{(*)} \to V$), neglecting off-diagonal contributions like $\gamma^{(*)} \to V^{(*)} \to V'$, where V' is a radially excited vector meson. These missing off-diagonal contributions are thought of as being responsible for the failure of VDM in the case of photoproduction of charmonium [24].

The idea of VDM as expressed in equation 2.18 is that the real and virtual photons fluctuate into a vector meson which then scatters off the proton (see figure 2.5). The proton can either stay intact (elastic vector meson production; figure 2.5 a) or dissociate (diffractive proton dissociation; figure 2.5 b). The transition between photon and vector meson is translated into the relation of the photon-proton cross sections:

$$\sigma(\gamma p \to V p) = \frac{4\pi\alpha_{QED}}{\gamma_V^2} \cdot \sigma(V p \to V p) . \tag{2.20}$$

For larger Q^2 values ($Q^2 \gtrsim m_V^2$) the vector meson propagator effect influences the photon proton cross section as follows:

$$\frac{\sigma_{\gamma p}^T(Q^2)}{\sigma_{\gamma p}^T(0)} = \frac{m_V^2}{m_V^2 + Q^2} , \tag{2.21}$$

$$\frac{\sigma_{\gamma p}^L(Q^2)}{\sigma_{\gamma p}^L(0)} = \xi \frac{Q^2}{m_V^2} \frac{m_V^2}{m_V^2 + Q^2} \tag{2.22}$$

for transversely and longitudinally polarized photons, respectively. The ratio of both contributions is then:

$$R(Q^2) = \frac{\sigma_{\gamma p}^L(Q^2)}{\sigma_{\gamma p}^T(Q^2)} = \xi \frac{Q^2}{m_V^2} , \tag{2.23}$$

where ξ is a phenomenological parameter of order 1, which takes into account that the Vp cross sections, σ_{Vp}, for transverse and longitudinal vector mesons could be different.

Within Regge theory diffractive processes at high energies are described by pomeron exchange. The characteristic of diffractive processes is the lack of colour flow between the scattered proton (or its dissociated remnant) and the hadronic final state (in this case the vector meson). This is explained by the exchange of a colourless object, the pomeron. These objects are thought of as

being poles of the partial waves as a function of the momentum in the complex plane, all lying on linear trajectories in this plane. The poles are determined by the possible bound and resonant states [12]. The linear trajectories, $\alpha(t) = \alpha_0 + \alpha' \cdot t$, are each defined by a particular intercept, α_0, and a slope, α'.

In this picture the $W_{\gamma p}$ and t dependence of the J/ψ production cross section at high energy is determined by the intercept α_0 and the slope α' of the pomeron trajectory:

$$\frac{d\sigma_{\gamma p}}{dt} = \left.\frac{d\sigma_{\gamma p}}{dt}\right|_{t=0, W_{\gamma p}=W_0} \cdot e^{-b|t|} \cdot \left(\frac{W_{\gamma p}}{W_0}\right)^{4(\alpha_0-1)}, \tag{2.24}$$

with

$$b = b(W_0) + 2\alpha' \ln\left(\frac{W_{\gamma p}^2}{W_0^2}\right). \tag{2.25}$$

2.2.1 Soft Pomeron Model

In Regge theory, the elastic scattering process is described by the exchange of a superposition of Regge trajectories; the cross section is a sum of all contributions of each single trajectory. Since the cross section for the exchange of trajectories with an intercept smaller than one ($\alpha_0 < 1$) decreases with increasing centre-of-mass energy, at HERA energies only the pomeron trajectory ($\alpha_0 \gtrsim 1$) contributes in the case of vector meson production. The pomeron trajectory was postulated in 1961 [25] in order to describe the rise of the elastic and total cross sections measured in hadron-hadron scattering at large centre-of-mass energies. An intercept larger than one and vacuum quantum numbers ($I = S = B = 0, P = C = G = +$) were needed [13]. The new trajectory was called the pomeron, since a scattering process dominated by pomeron exchange fulfils the Pomeranchuk Theorem [26]; according to this theorem, the total cross section for the scattering

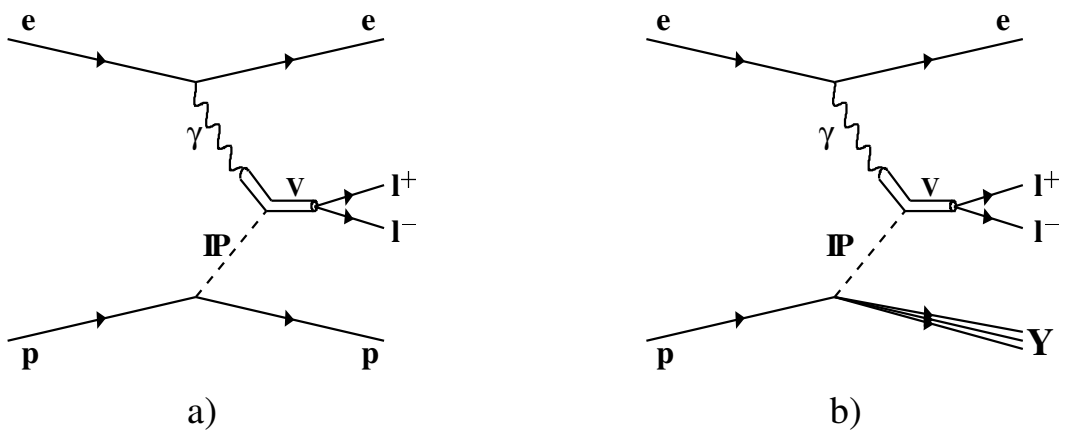

Figure 2.5: Vector meson production in Regge theory and the Vector Meson Dominance Model for a) elastic vector meson production and b) the proton dissociative process.

of particles and their anti-particles off a third particle should become equal at high energies. In contrast to those trajectories with an intercept of less than one (called reggeons), which can be related to observed particles (ρ, ω, f_2, a_2), no particle is known to lie on the pomeron trajectory[1].

Donnachie and Landshoff [17] performed a fit to $pp, \bar{p}p, \pi^- p, \pi^+ p, K^- p, K^+ p$ and γp data. They obtained a universal value for the intercept of the pomeron of

$$\alpha_0 = 1 + \varepsilon = 1.0808 \tag{2.26}$$

and a slope value of

$$\alpha' = 0.25\,\mathrm{GeV}^{-2}\,. \tag{2.27}$$

Together with the reggeon's intercept $\alpha_0 = 1 - \eta = 1 - 0.4525$ the energy dependence of all hadronic total cross sections and the total γp cross section can be parameterized as follows:

$$\sigma_{tot} = X s^{\varepsilon} + Y s^{-\eta}\,, \tag{2.28}$$

where the first term corresponds to pomeron and the second to reggeon exchange.

The main features predicted by the soft pomeron model of Donnachie and Landshoff are summarized in the following:

- From equation 2.24 follows an exponentially falling $|t|$ distribution, $\frac{d\sigma}{dt} \propto e^{-b|t|}$. The elastic slope parameter b can be interpreted as a geometrical measure for the size of the scattering objects in analogy to optical diffraction [27]: $b = (R_p^2 + R_v^2)/4$. With the proton radius $R_p \simeq 4\,\mathrm{GeV}^{-2}$ and measured elastic slope parameters in J/ψ production of $b \simeq 4 - 5\,\mathrm{GeV}^{-2}$, the J/ψ at HERA energies behaves almost point-like. This is not the case for ρ photoproduction ($b \simeq 10\,\mathrm{GeV}^{-2}$). The slope parameter for J/ψ production with proton dissociation is significantly smaller ($b \simeq 2\,\mathrm{GeV}^{-2}$).

- From equation 2.25: a non-universal, $W_{\gamma p}$ dependent elastic slope parameter, which increases logarithmically with energy. This effect is also known as *shrinkage* of the elastic (or forward) peak and provides a distinctive feature with respect to predictions within perturbative QCD, where b is thought of as being universal (see section 2.3).

- From equation 2.24 follows a slow increase of the cross section with energy, $\sigma_{\gamma p} \propto W_{\gamma p}^{0.22}$ ($\sigma_{\gamma p} \propto W_{\gamma p}^{0.32}$ without shrinkage). This is in strong contrast to the measured energy dependence of J/ψ production at HERA energies, $\sigma_{\gamma p} \propto W_{\gamma p}^{\sim 0.8}$ [15].

- In the case of proton dissociation, the same $W_{\gamma p}$ dependence of the cross section is expected as in the elastic case. In addition, the cross section is expected to fall like $1/M_Y^{2(1+\varepsilon)} \simeq 1/M_Y^2$ [27], with M_Y denoting the mass of the dissociated system, which is confirmed by experimental data [28].

[1] In [19] Donnachie and Landshoff fitted two 2^{++} glueball candidates to their *soft* and *hard* pomeron trajectories.

2.2.2 Two Pomeron Model

The data of various processes measured at HERA, such as the proton structure function F_2 for $x < 0.7$, the charm structure function and the elastic J/ψ photoproduction cross section deviate from the predictions of the soft pomeron model, but they are all in agreement with the assumption that there is a second pomeron, with an intercept of about $\alpha_{0_h} \simeq 1.4$. As one of the simplest assumptions, Donnachie and Landshoff [19] treat each of the two pomerons as a simple pole in the complex momentum plane, so that the contribution from each is a simple power of $W_{\gamma p}$ (or s, see equation 2.28). In addition to the two terms with powers ε and $-\eta$ in equation 2.28 a third term is added, which they call hard pomeron exchange (ε_h). Fits to γp cross section and F_2 data for $x < 0.07$ and $Q^2 < 10\,\mathrm{GeV}^2$ are performed yielding an intercept of the hard pomeron of $\alpha_{0_h} = 1 + \varepsilon_h = 1.418$. A systematic error on this result of about $\varepsilon_h \pm 0.05$ is estimated by the authors, preferring the upper end of this range as suggested by the presently available charm data ($F_2^{c\bar{c}}$).

Whatever the explanation of the hard pomeron might be, it is interesting that the mass scale that determines how rapidly its contribution to F_2 rises with Q^2, is considerably larger than the corresponding soft pomeron scale. Nevertheless, it may well be that even the hard pomeron is non-perturbative and that it is just a glueball trajectory [19]. The fact that the J/ψ photoproduction cross section rises much more steeply with energy than predicted by the soft pomeron model suggests that the slope of the hard pomeron trajectory may be small ($\alpha'_h \simeq 0.1\,\mathrm{GeV}^{-2}$). The resulting *hard* pomeron trajectory is then:

$$\alpha_h(t) \simeq 1.4 + 0.1 \cdot t\,. \tag{2.29}$$

2.2.3 BFKL Pomeron

Within the framework of the BFKL formalism a pomeron is postulated which is the perturbative QCD equivalent of the soft pomeron. An introduction to the BFKL formalism can be found elsewhere [30]. Here only the so-called BFKL pomeron [29] is introduced. It is an asymptotic ($x \to 0$) of the scattering amplitude in perturbative QCD in a certain kinematic region, where the logarithmic scale is large, $\alpha_s \ln(1/x) \gg 1$, and the virtualities of the incoming particles are more or less the same.

The highest eigenvalue of the BFKL equation is related to the intercept of the pomeron. In leading order (LO) it turns out to be rather large, $\alpha_{0_{BFKL}} = 1 + 12\ln(2\alpha_s/\pi) \simeq 1.55$ for $\alpha_s = 0.2$. Since the running of the QCD coupling constant α_s is not included and the allowed kinematic range of LO BFKL is not known, next-to-leading order (NLO) calculations are important. Recently the NLO corrections to the BFKL resummation of energy logarithms became available [31], and found to be large. Within non-Abelian physical schemes together with the BLM scale setting [32] the resulting NLO BFKL pomeron intercept is about $\alpha_{0_{BFKL}} \simeq 1.165$. In [29] no statement is made about the slope of the trajectory. For comparison with the data of this analysis it is assumed to be zero. The resulting BFKL pomeron trajectory is then:

$$\alpha_{BFKL}(t) \simeq 1.165\,. \tag{2.30}$$

2.3 Perturbative QCD Calculations

In perturbative QCD diffractive vector meson production is described by the exchange of a colourless two-gluon system (see figure 2.6) in leading logarithmic approximation (LLA), which uses the whole system of LLA ladder diagrams instead of the simple two-gluon pomeron. The amplitude is proportional to the gluon density in the proton, $\mathcal{A} \propto xg(x, Q^2_{eff})$, and the diffractive cross section to its square:

$$\sigma_{\gamma p} \propto [xg(x, Q^2_{eff})]^2 . \tag{2.31}$$

Therefore diffractive J/ψ production may be a good way to extract the gluon density in the proton as proposed by Ryskin in [33]. First attempts in leading order are described by using previous HERA and fixed target experiment results [34, 35]. But due to non-perturbative QCD effects, which are not yet under control, the related measurement is not performed in the present analysis.

Assuming that the exchanged pomeron is a gluon ladder (see figure 2.7), the transition from soft to hard processes can be understood within the following picture: During the trip from the virtual photon vertex down to the proton, the average transverse momentum, k_T, of the gluons gets smaller, the configuration larger, and at the proton vertex the low k_T region is reached governed by non-perturbative QCD. The average k_T of the partons in the process can be estimated by the slope of the exchange's trajectory since $\alpha' \propto 1/\langle k_T \rangle$. The question whether this transition is present might be answered by the determination of the pomeron trajectory in a given process. For a hard process $\alpha' \ll 0.25\,\mathrm{GeV}^{-2}$ would be expected [5].

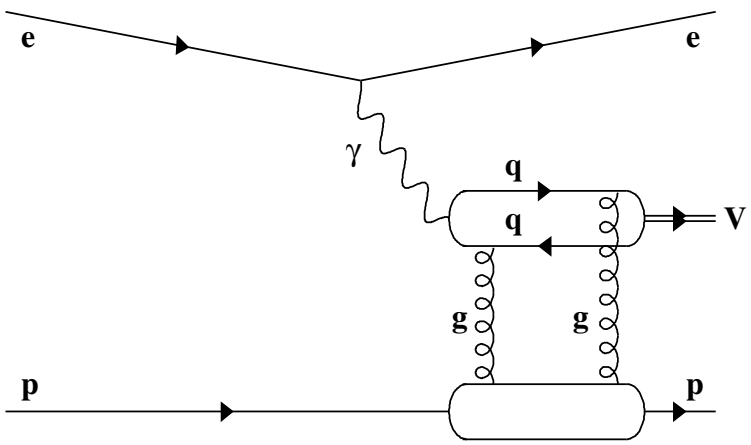

Figure 2.6: Leading order graph for elastic vector meson production in pQCD based models. Calculated, but not shown, are all four possible combinations of the two gluons coupling to the two quarks.

One basic concept of the description of diffractive vector meson production within perturbative QCD is the factorization of the process into three parts due to the QCD factorization theorem [36] and the large longitudinal coherence length associated with high energy (small x) diffractive processes [37, 38]:

- The fluctuation of the photon into a $q\bar{q}$ pair *long before* the interaction.
- The interaction between the $q\bar{q}$ pair and the proton on a *short* time scale ($x \ll 0.06$).
- The formation of the vector meson *long after* the interaction.

In order to apply perturbative QCD, the effective Q^2_{eff}, which provides the relevant scale in the process, has to be much larger than Λ_{QCD}. Therefore these calculations are applicable either in electroproduction at significant Q^2 values or, in photoproduction, for heavy vector mesons such as J/ψ, $\psi(2S)$ and Υ. While Ryskin has chosen Q^2_{eff} as $Q^2_{eff} = \frac{Q^2+m_V^2}{4}$, Frankfurt et al. have performed a rescaling, which leads to a significantly larger effective scale [39].

As shown in [38], for sufficiently large Q^2_{eff}, the process is dominated by $q\bar{q}$ configurations where the quark and antiquark are separated by a small transverse distance only. In the LLA only terms of the order $\alpha_s \ln(Q^2_{eff}/\Lambda^2_{QCD})$ are taken into account. The photon-proton cross section at $t = 0$ is in leading order [39]:

$$\left.\frac{d\sigma_{\gamma^{(*)}p}}{dt}\right|_{t=0} = \frac{12\pi^3\Gamma_{ee}m_V^3}{\alpha_{em}(Q^2+4m_q^2)^4} \cdot \left|\alpha_s(Q^2_{eff})(1+i\beta)xg(x,Q^2_{eff})\right|^2 \cdot \left(1+\varepsilon\frac{Q^2}{m_V^2}\right) \cdot C(Q^2), \quad (2.32)$$

where m_q is the pole mass of the quarks inside the vector meson (m_V), and x is given by

$$x = \frac{Q^2+m_V^2}{W^2_{\gamma p}}. \quad (2.33)$$

β denotes the relative contribution of the real part of the amplitude of the scattering of the $q\bar{q}$ pair off the parton in the proton:

$$\beta = \frac{\mathrm{Re}\mathcal{A}}{\mathrm{Im}\mathcal{A}} \simeq \frac{\pi}{2}\frac{\partial \ln(xg(x,Q^2_{eff}))}{\partial \ln x}, \quad (2.34)$$

which is small in case of J/ψ production, but of the order of one for Υ mesons. $C(Q^2)$ is a Q^2 dependent correction factor:

$$C(Q^2) = \left(\frac{Q^2+4m_q^2}{Q^2+4m^2_{run}}\right)^4 \cdot \left(\frac{\eta_V^2}{3}\right) \cdot \mathcal{T}(Q^2) \cdot \frac{\mathcal{R}(Q^2)+\varepsilon\frac{Q^2}{m_V^2}}{1+\varepsilon\frac{Q^2}{m_V^2}}. \quad (2.35)$$

Several Q^2 dependent corrections with respect to the asymptotic expression are taken into account in the term $C(Q^2)$:

- m_{run} is the running mass of the quarks in the vector meson, given by

$$m^2_{run}(Q^2_{eff}) = m_q^2\left(1-\frac{8\alpha_s(Q^2_{eff})}{3\pi}\right). \quad (2.36)$$

- η_V is a leading twist correction, taking into account the difference between the vector meson *decaying* into an e^+e^- pair and diffractive vector meson *production*.

- $\mathcal{T}(Q^2)$ takes into account effects related to the Fermi motion of the quarks in the vector meson [38, 42].
- The factor $\mathcal{R}(Q^2)$ parameterizes the relative contribution of the production of transversely polarized vector mesons as compared to the naive prediction, and $\varepsilon = \frac{1-y}{1-y+y^2/2}$ is the polarization parameter ($\varepsilon = 1$).

The effective scale Q^2_{eff}, at which the gluons are sampled, is related to the dominant $q\bar{q}$ transverse distances in the respective quark loops. The value in J/ψ photoproduction, used in [39], is $Q^2_{eff} \simeq 5.1\,\mathrm{GeV}^2$. The corresponding scale for Υ production is significantly larger [43], see table 2.1.

	J/ψ	$\Upsilon(1S)$	$\Upsilon(2S)$	$\Upsilon(3S)$
$Q^2_{eff}\,[\mathrm{GeV}^2]$	$\simeq 5.1$	$\simeq 40$	$\simeq 60$	$\simeq 75$

Table 2.1: Effective scales, Q^2_{eff}, for J/ψ, $\Upsilon(1S)$, $\Upsilon(2S)$ and $\Upsilon(3S)$ mesons, as used for cross section predictions in [39, 43].

The overall correction factor $\mathcal{C}(Q^2)$ for J/ψ photoproduction at HERA is of the order of $\mathcal{C}(Q^2) \simeq 0.1$ and $\mathcal{C}(Q^2) \simeq 0.5$ at $Q^2 = 100\,\mathrm{GeV}^2$. The largest single contribution is the Fermi motion suppression factor. While the influence on the cross section as a function of $W_{\gamma p}$ is mainly a change of the normalization, the Q^2 spectrum becomes significantly harder. In the case of Υ photoproduction the finite Q^2 correction factor is about $\mathcal{C}(Q^2 = 0) \simeq 0.3$, calculated with the same method as for J/ψ production (see figure 10 in [39]).

A large uncertainty in the prediction of the cross section is due to the uncertainty of the quark pole mass m_q. Varying m_q from $1.3 - 1.7\,\mathrm{GeV}$ changes the normalization of $\sigma_{\gamma p}$ by about a factor of two at $W_{\gamma p} = 90\,\mathrm{GeV}$. The choice of the gluon density function has a significant influence both on the shape and on the normalization of the cross section. In order to compare the measured J/ψ cross sections with the predictions later on (section 5), the cross section predicted by [39] is calculated for different parton densities, each adjusted by the choice of a certain charm quark pole mass, in order to fit the data in absolute magnitude.

In perturbative QCD models as presented here, a certain – but very weak – energy dependence of the slope parameter b is also predicted. Frankfurt et al. [39] find values for α' (see equation 2.25) of the order of $0.005 - 0.1\,\mathrm{GeV}^{-2}$ depending on x and t, which has to be compared to the larger value of $\alpha' = 0.25\,\mathrm{GeV}^{-2}$ in the case of the soft pomeron. They expect an elastic slope parameter $b = 4 - 5\,\mathrm{GeV}^{-2}$, almost independent of $W_{\gamma p}$.

2.3.1 Differences between J/ψ and Υ Production

When the first HERA results on diffractive Υ photoproduction became available [40, 41], the predictions based on the same assumptions as for J/ψ production [39] were about two standard deviations below the data. Since then, new calculations have been performed by two different

groups [43, 44] taking into account mainly two novel effects, which turn out to be much more important than in the case of the J/ψ meson. On the one hand, the relative contribution of the real part of the amplitude is much larger for Υ than for J/ψ production, and on the other hand, the effect of skewed dynamics of the exchanged two-gluon system is more important for Υ mesons. Each effect accounts roughly for a factor of two in the cross section. In addition, a strong correlation between the mass of the vector meson and the energy dependence of the cross section is found. In particular, a considerably stronger rise with energy is predicted for Υ mesons ($\sigma_{\gamma p} \propto W_{\gamma p}^{\sim 1.7}$) than that found in J/ψ production ($\sigma_{\gamma p} \propto W_{\gamma p}^{\sim 0.8}$). Martin et al. [44] have also calculated a correction factor of 1.2 accounting for NLO effects [44].

Real Part of the Amplitude

At HERA energies Υ mesons are produced at large effective scales compared to J/ψ mesons (see table 2.1) and at relatively high x ($0.001 \lesssim x \lesssim 0.02$). Therefore the real part of the amplitude is large. It is calculated using a fit to the energy dependence of the imaginary part and dispersion relations. In the case of J/ψ production the ratio of real to imaginary parts of the amplitude, $\beta = \frac{\mathrm{Re}\mathcal{A}}{\mathrm{Im}\mathcal{A}}$, was calculated using the approximate solution of the dispersion relation (see equation 2.34). This is only appropriate at small x and fairly low scales, but in the case of Υ production it is necessary to include an additional sub-leading power in $1/x$ or equivalently in $W_{\gamma p}^2$. The effective difference between the recalculated β [43] and the one from equation 2.34 is given in table 2.2 as a function of $W_{\gamma p}$. It is most pronounced for smaller values of $W_{\gamma p}$.

$W_{\gamma p}$ [GeV]	80	130	180	230	280
β_{old}	0.94	0.82	0.77	0.75	0.73
β_{new}	1.12	0.87	0.79	0.74	0.71

Table 2.2: Contribution of the real part of the amplitude for $\Upsilon(1S)$ production for the CTEQ4L parton density at an effective scale of $Q_{eff}^2 = 40\,\mathrm{GeV}^2$, calculated by Frankfurt et al. [43].

Martin et al. [44] give a correction factor on the cross section due to the real part of the amplitude of 1.43 at $W_{\gamma p} = 120\,\mathrm{GeV}$ and 1.36 at $W_{\gamma p} = 160\,\mathrm{GeV}$ for the MRS(R2) parton distribution.

Skewed Parton Densities

Recently, there has been considerable progress in calculating and understanding skewed parton distributions, which probe new non-perturbative information about hadrons and are a generalization of conventional parton distributions [45]. They are relevant for hard processes such as deeply virtual Compton scattering, diffractive photoproduction of dijets and photo- and electroproduction of heavy vector mesons.

The gluon emitted by the proton carries the proton momentum fraction x'' from the proton, while it has only the momentum fraction x with $x \ll x''$ when coupling to the quark. The returning

gluon carries $x-\xi$ at the quark-gluon vertex and $x''-\xi$ at the proton-gluon vertex. Because the momentum fraction x and the difference in momenta of outgoing and returning gluon are of the same order of magnitude ($x \approx \xi$), the two gluons couple to the partons in the proton at different x values. With the coupling of the two gluons to the quark-antiquark pair, skewed parton density functions are probed at the vector meson level.

The skewedness, ξ, is given by the difference in momentum fractions carried by the outgoing (x) and returning ($x-\xi$) gluons (see figure 2.7), defined by:

$$x = \frac{m_{q\bar{q}}^2 + Q^2}{W_{\gamma p}^2 + Q^2}, \qquad x - \xi = \frac{m_{q\bar{q}}^2 - m_V^2}{W_{\gamma p}^2 + Q^2}, \tag{2.37}$$

$$\xi = \frac{m_V^2 + Q^2}{W_{\gamma p}^2 + Q^2}, \tag{2.38}$$

with $m_{q\bar{q}}$ denoting the mass of the intermediate $q\bar{q}$ state. From equation 2.38 the different influence of skewed dynamics in the case of J/ψ and Υ production can be seen ($\xi \propto m_V^2$). In the kinematic range of the analysis presented here, even though the mean $W_{\gamma p}$ value is much higher in the case of Υ production ($\langle W_{\gamma p} \rangle = 160\,\text{GeV}$) than for J/ψ ($\langle W_{\gamma p} \rangle = 90\,\text{GeV}$), the skewedness ξ is about a factor of two larger for Υ mesons. It is of the same order of magnitude as the momentum fraction x itself. For photoproduction at HERA, $\xi = \frac{m_V^2}{W_{\gamma p}^2}$ lies in the range $0.0011 \lesssim \xi \lesssim 0.017$ for Υ mesons and is about one order of magnitude smaller for J/ψ production.

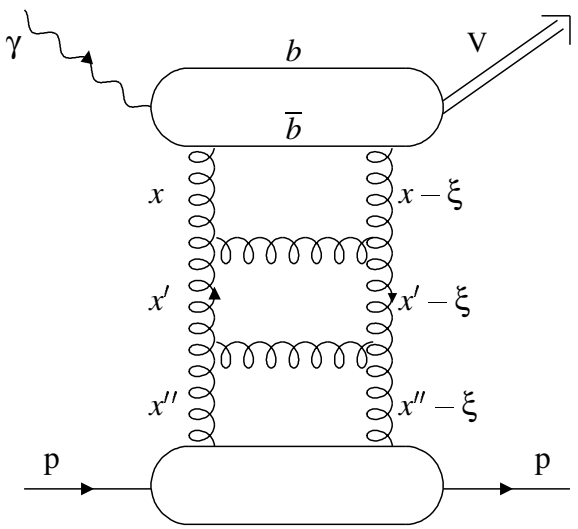

Figure 2.7: Diagram for the exchange of a gluon ladder.

Replacing the conventional gluon densities by the skewed distributions changes the cross section by an overall factor of about 2.6 (Frankfurt et al.) or 2.0 (Martin et al.), respectively. The

correction is almost negligible for ρ production, and leads to about 10 % enhancement of the J/ψ amplitude [43], but is much more important for Υ photoproduction since the scale Q^2_{eff} and the value of x are much larger.

2.4 Monte Carlo Models

For the correction of the data, simulated events are used. The Monte Carlo generators deliver four-momenta of all particles in a given process with lifetimes longer than typically 8 ns. These generated events are tracked through the detector with help of a GEANT [46] based program. Then the detector and trigger response is simulated and finally the same reconstruction software as for real data is applied, taking detector noise into account by means of randomly triggered events from special runs. Two different Monte Carlo generators are used in the present analysis: DIFFVM for the simulation of elastic and proton dissociative J/ψ and Υ events and LPAIR, which simulates non-resonant QED lepton pair production. In this section both generators will be introduced and their physics input will be discussed.

2.4.1 DIFFVM

The DIFFVM [47] Monte Carlo generator was originally written to simulate diffractive vector meson production in ep scattering at HERA within the framework of Regge theory and the VDM (compare section 2.2). Both elastic and proton dissociative vector meson production can be simulated. Since many parameters can be adjusted freely, DIFFVM can be used as a largely model independent tool describing diffractive vector meson production which uses the basic ideas and terminology of Regge theory.

The emission of the photon from the incoming electron is treated within the equivalent photon approximation. Depending on y and Q^2, the angle and energy of the scattered electron are calculated. The emitted photon has a certain helicity, which is relevant for the angular distribution of the vector meson's decay particles and the Q^2 dependence of the cross section. Emission of additional photons (initial or final state radiation) is not implemented.

The transition of the photon to the virtual vector meson is modelled according to the VDM. The Q^2 dependence of the cross section for transversely polarized photons $\sigma^T_{\gamma p}$ is parameterized with

$$\sigma^T_{\gamma p} = \sigma_{\gamma p} \cdot \left(\frac{1}{1+\frac{Q^2}{\Lambda^2}} \right)^n , \tag{2.39}$$

with the free parameters n and Λ. Within the VDM these two parameters are chosen to be $n = 2$ and $\Lambda = m_V$, where m_V is the mass of the produced vector meson. For longitudinally polarized photons the cross section $\sigma^L_{\gamma p}$ is given by

$$R(Q^2) = \frac{\sigma^L_{\gamma p}}{\sigma^T_{\gamma p}} = \frac{\xi \cdot \frac{Q^2}{\Lambda^2}}{1+\chi \cdot \xi \cdot \frac{Q^2}{\Lambda^2}} , \tag{2.40}$$

where ξ is a constant factor of order 1, and χ is a purely phenomenological parameter, which limits R to the asymptotic value $1/\chi$ for $Q^2 \gg \Lambda^2$. For $\Lambda = m_V$ and $\chi = 0$ this reduces to

$$R(Q^2) = \xi \cdot \frac{Q^2}{m_V^2}, \tag{2.41}$$

and the cross section ratio is proportional to Q^2.

The dependence of the cross section on $W_{\gamma p}$ and t is parameterized according to Regge theory:

$$\frac{d\sigma}{dt} = \left.\frac{d\sigma}{dt}\right|_{t=0, W_{\gamma p}=W_0} \cdot e^{-b|t|} \cdot \left(\frac{W_{\gamma p}}{W_0}\right)^{4\varepsilon}, \tag{2.42}$$

with

$$b(W_{\gamma p}) = b(W_0) + 2\alpha' \ln\left(\frac{W_{\gamma p}^2}{W_0^2}\right), \tag{2.43}$$

where $b(W_0)$ is the slope parameter at some specific $W_{\gamma p}$, and $\varepsilon + 1$ and α' are the intercept and the slope of the exchanged pomeron trajectory. In the DIFFVM Monte Carlo generator, all these parameters can be chosen freely.

In the case of proton dissociative vector meson production, the cross section is proportional to $1/M_Y^{2(1+\varepsilon)}$, with M_Y being the mass of the dissociated system. In DIFFVM $1/M_Y^{2(1+0.08)}$ is used. Within the DIFFVM generator the dissociated system is treated as one of the nucleon resonances N(1440), N(1520), N(1680) or N(1710) for masses $M_Y < 1.9\,\text{GeV}$, which decay subsequently according to [48], while for larger masses a quark and a diquark are fragmented according to the Lund string fragmentation within the JETSET Monte Carlo program [49].

The main steering parameters which were used for event simulation in the present analysis are summarized in table 2.3.

	ε	n	Λ	ξ	χ	α'	b_{el}	b_{pd}
J/ψ	0.225	2.5	m_ψ	1.0	0.0	0.0	$4.0\,\text{GeV}^{-2}$	$1.6\,\text{GeV}^{-}2$
Υ	0.425	3.0	m_Υ	1.0	0.0	0.0	$4.0\,\text{GeV}^{-2}$	$1.6\,\text{GeV}^{-}2$

Table 2.3: Steering parameters used for J/ψ and Υ event simulation with the DIFFVM generator.

2.4.2 LPAIR

For the simulation of non-resonant background events the Monte Carlo generator LPAIR [50] is used. It generates elastic and proton dissociative events containing lepton pairs originating from multi-peripheral two-photon QED processes, $\gamma\gamma \to \mu\mu$, as sketched in figure 2.8 a and b respectively.

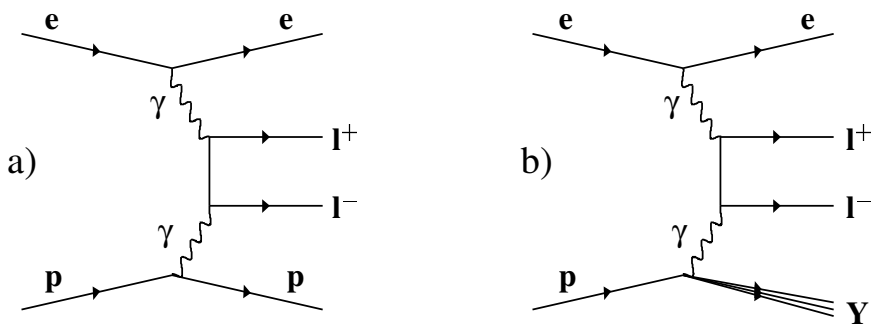

Figure 2.8: Graphs for QED two-photon processes as simulated with the LPAIR generator: a) elastic and b) dissociative multi-peripheral diagram for non-resonant lepton pair production.

These graphs describe the dominant source of background for diffractively produced J/ψ and Υ mesons. Further diagrams such as the Cabibbo-Parisi effect, the Compton-like or the Drell-Yan processes (see figure 2.9), in which the initial or final electron or one quark out of the proton radiates a photon, which then produces a lepton pair, are not considered in the LPAIR generator. Their contributions are expected to be negligible in the phase space covered by this analysis.

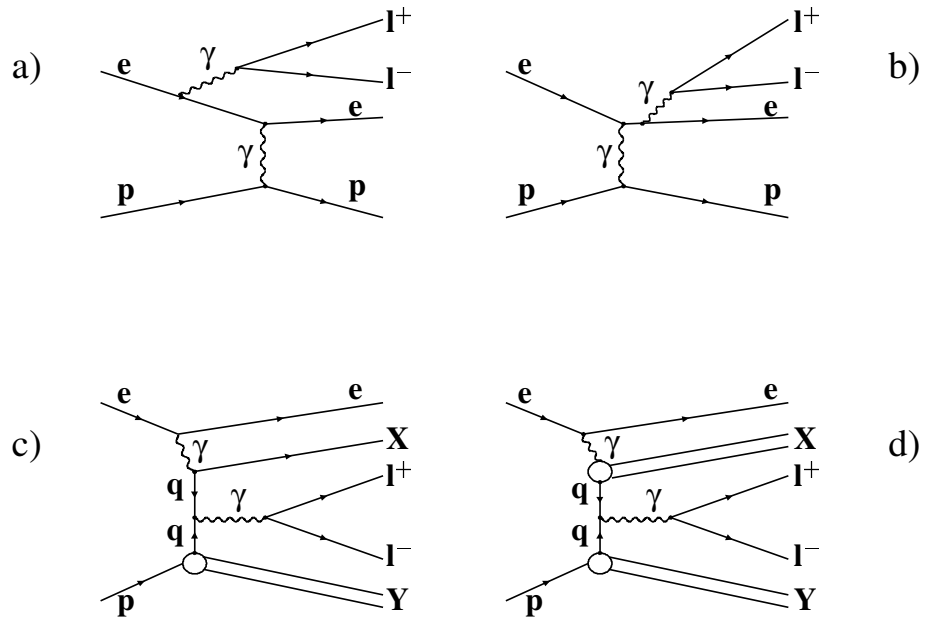

Figure 2.9: Graphs for QED two-photon processes not simulated with the LPAIR generator: a) Cabibbo-Parisi effect, b) Compton-like graph, c) point-like and d) resolved Drell-Yan process.

The LPAIR Monte Carlo is only used in the context of the b slope measurement. Since the t dependence of the QED two-photon cross section is steep compared to that of the J/ψ cross section, the simulated events are used to correct the t distribution for non-resonant background. In the case of the cross section measurement and the determination of the Regge trajectory the background is determined from the mass spectrum in the data without the need for simulated events.

Chapter 3

The H1 Detector at HERA

The data for this analysis come from e^+p collisions in HERA[1], at the DESY[2] laboratory in Hamburg. HERA collides positrons (or electrons) and protons at a centre of mass energy of 300 GeV. The data were collected by the H1 detector, a general purpose detector with almost hermetic calorimetry, precise tracking inside a solenoidal magnetic field, good lepton identification, and a fast four level trigger system. A detailed description of the H1 detector can be found elsewhere [51].

In this chapter the components of the experiment relevant for the present analysis are described, including the accelerator performance, tracking, calorimetry, and the muon and luminosity systems. The trigger chain and the two methods of muon identification used in subsequent chapters are also discussed.

3.1 Positron-Proton Collisions at HERA

A schematic overview of the HERA storage ring is shown in figure 3.1. Within two independent accelerators - one for protons and one for positrons - with a total circumference of 6.4 km, protons are accelerated up to beam energies of 820 GeV and positron beams are operated with 27.5 GeV. For the analysis presented here only positron-proton data are used from the years 1994 to 1997 in case of the Υ analysis and from 1996 to 1997 in case of the J/ψ analysis, respectively. In 1998 and 1999 electrons and protons have been collided and the proton beam was operated with 920 GeV. When the beams have reached their final energy, they are tuned to collide at very small angles in the interaction regions of the H1 and ZEUS experiments. The available centre-of-mass energy is $\sqrt{s} \approx 300$ GeV. This is one order of magnitude larger than the energies achieved so far in fixed target lepton-nucleon scattering experiments, and it is equivalent to a fixed target experiment operating with an electron beam of approximately 50 TeV.

The positron and proton beams are packed into 189 and 180 bunches, respectively, with a short bunch crossing interval of 96 ns (10.4 MHz). A small number of non-colliding bunches (*pilot*

[1] HERA=Hadron Electron Ring Accelerator
[2] DESY=Deutsches Elektronen Synchrotron

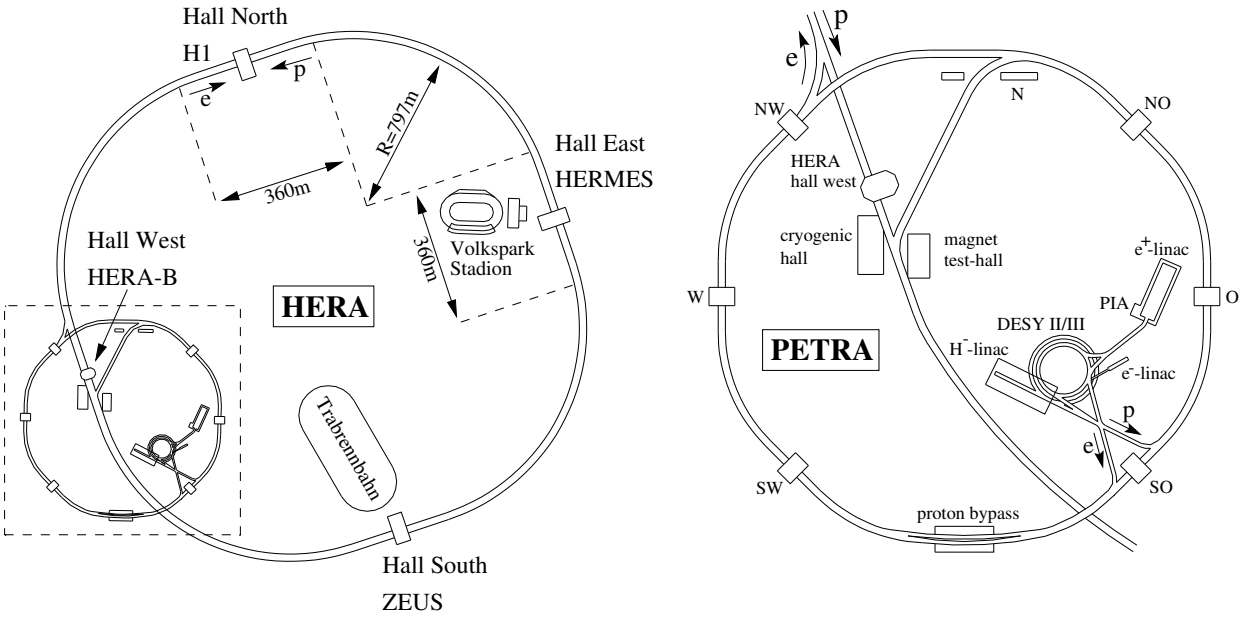

Figure 3.1: The storage ring HERA and its pre-accelerators at DESY. In addition the four experiments H1, ZEUS, HERMES and HERA-B are shown at the four interaction regions.

bunches) is usually preserved as a means of studying beam induced background arising from interactions of the beam with the residual gas in the beam pipe, or with its wall. The proton beam lifetime is rather large, of the order of 100 h, while the electron beam lifetime of about 10 – 20 h limits the typical duration of luminosity runs to less than 15 h. The integrated luminosity produced in the years 1992 to 1999 is shown in figure 3.2. The rise of the beam currents and HERA performance during the last years is clearly visible.

3.2 The H1 Detector

The H1 detector is a typical multi-purpose collider experiment consisting of several subdetectors. A specific feature of H1 is its enhanced instrumentation in the proton direction taking into account the asymmetric beam energies and boosted final states. A schematic view of the detector is shown in figure 3.3.

The main H1 detector has the approximate dimensions $12 \times 15 \times 10\,\mathrm{m}^3$ and weighs about 2800 t. The righthanded H1 coordinate system is shown in figure 3.3, it is chosen such that the z-axis is in the direction of the outgoing proton beam, called the forward direction.

3.2.1 Tracking System

The H1 tracking system consists of jet and drift chambers, multiwire proportional chambers as well as silicon detectors, which are integrated into a Forward Track Detector (FTD) and

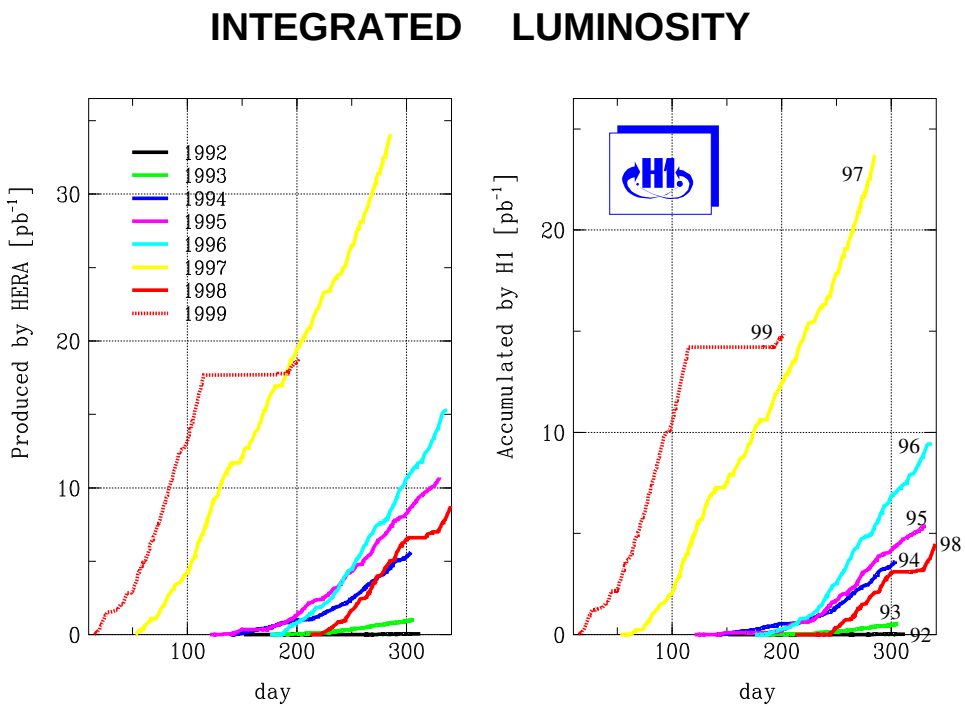

Figure 3.2: Integrated luminosity produced by HERA and measured in H1 for the years 1992-1999.

a Central Track Detector (CTD) (see figure 3.4). For this analysis only the CTD is used. It consists - radially from inside out - of the Central Silicon Tracker (CST), the Central Inner Proportional Chamber (CIP), the Central Inner z-Drift Chamber (CIZ), the inner Central Jet Chamber (CJC1), the Central Outer z-Drift Chamber (COZ), the Central Outer Proportional Chamber (COP) and the outer Central Jet Chamber (CJC2). While four of these chambers are used for track reconstruction (CJC1, CJC2, CIZ and COZ), the multiwire proportional chambers (CIP and COP) provide information for trigger purposes.

The six cylindrical chambers of the CTD are concentrically arranged in an aluminium tank. They provide a good momentum, angular and vertex resolution as well as a charge determination from the particle tracks. The CTD covers a polar angular range of $15^\circ \lesssim \vartheta \lesssim 165^\circ$.

Central Jet Chamber CJC

The track reconstruction in the central part of the H1 detector is performed using mainly the information of the inner and outer Central Jet Chambers (CJC1 and CJC2). CJC1 is built of 30 drift cells with 24 sense wires each, whereas CJC2 consists of 60 drift cells containing 32 sense wires each. The active length in z is 220 cm and the radial dimensions are 22.4 cm (CJC1) and 29.6 cm (CJC2) respectively.

The sense wires of the chambers are strung parallel to the beam axis (z-direction) to give accurate resolution in the $r\varphi$-plane. The drift cells are tilted by about 30° with respect to the radial direction (compare figure 3.5), so that the ionization electrons of high energy particles drift

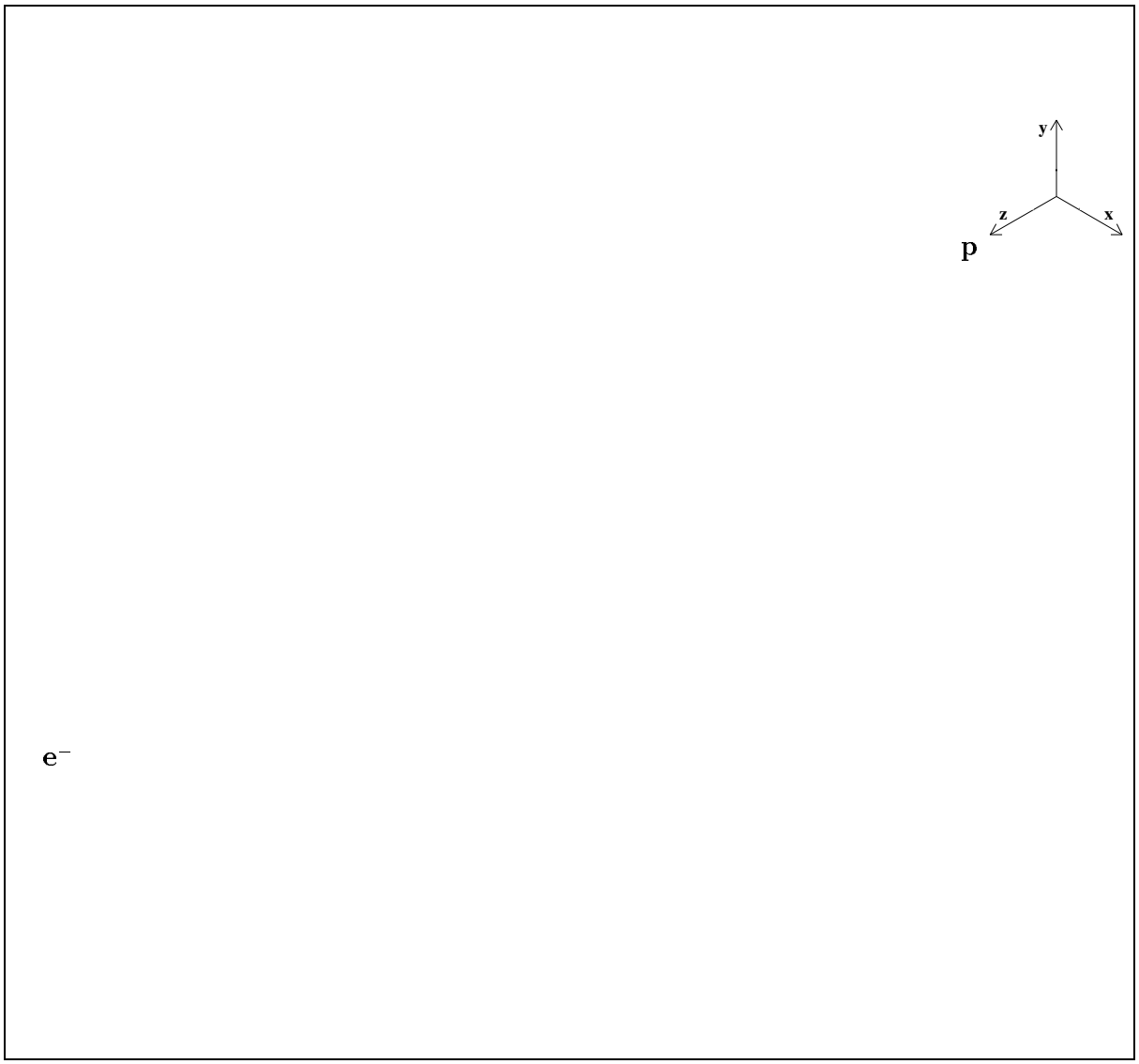

1 Beam pipe and beam magnets
2 Central tracking chambers
3 Forward tracking chambers
4 Electro-magnetic calorimeter (lead/liquid argon)
5 Hadronic calorimeter (steel/liquid argon)
6 Superconducting coil ($B = 1.15\,\mathrm{T}$)
7 Compensating magnet ($B = 4.83\,\mathrm{T}$)
8 Helium cryogenics
9 Muon chambers
10 Instrumented iron (iron slabs and streamer tube detectors)
11 Muon toroid magnet ($B = 1.6\,\mathrm{T}$)
12 Backward drift chamber and calorimeter
13 Plug calorimeter
14 Concrete shielding
15 Liquid argon cryostat

Figure 3.3: Schematic view of the H1 Detector. The H1 coordinate system is defined in the top right corner.

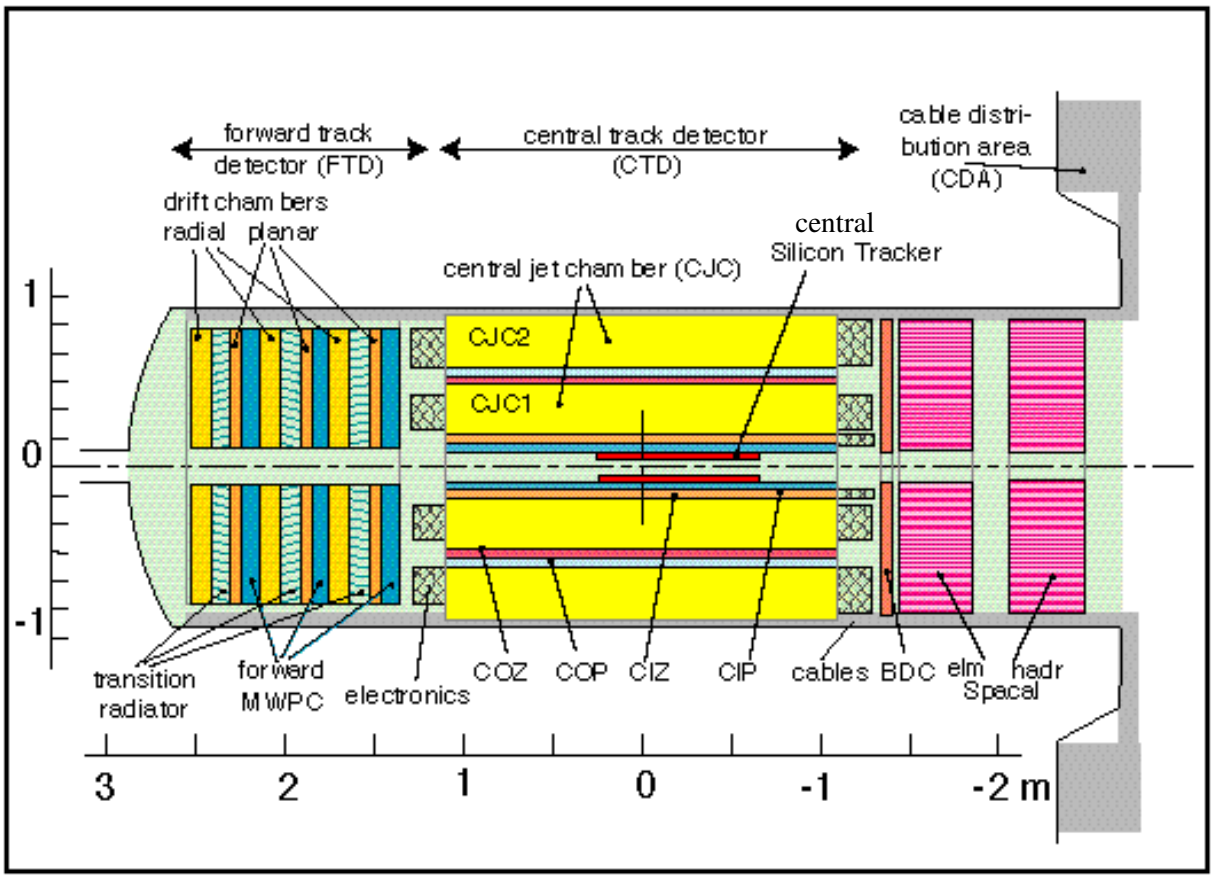

Figure 3.4: Schematic side view of the tracking system. In addition to the Forward Track Detector (FTD) and the Central Track Detector (CTD) the backward calorimeter SpaCal is also shown.

approximately perpendicular to the particle's direction of flight. This results in optimum track resolution and solves drift ambiguities caused by mirror track segments, which do not continue in neighbouring cells. Also the effect on the drift direction introduced by the presence of a magnetic field, the so-called *Lorentz angle*, is compensated by the tilt of the drift cells.

The spatial resolution of the CJC in the $r\varphi$-plane is measured to be $\sigma_{r\varphi} = 170\,\mu$m and the momentum resolution is $\sigma_{p_t}/p_t^2 = 0.01/\text{GeV}$. The sense wires are read out at both ends thus allowing determination of the z-coordinate by the means of charge division. But since the z-resolution achieved with this method is only $\sigma_z = 22\,$mm, the measurement of the z-coordinate is mainly performed with the z-drift chambers CIZ and COZ.

Central Inner and Outer z-Drift Chambers CIZ and COZ

The two thin drift chambers sandwiching the inner Jet Chamber, CIZ on the inner side and COZ on the outer side of CJC1, allow a satisfactory resolution of the z measurement ($\sigma_z \approx 300\,\mu$m). These chambers cover the polar angular range $16^\circ \lesssim \vartheta \lesssim 169^\circ$ (CIZ) and $25^\circ \lesssim \vartheta \lesssim 156^\circ$ (COZ). The CIZ consists of 15, the COZ of 24 similar rings, which are arranged along the beam axis,

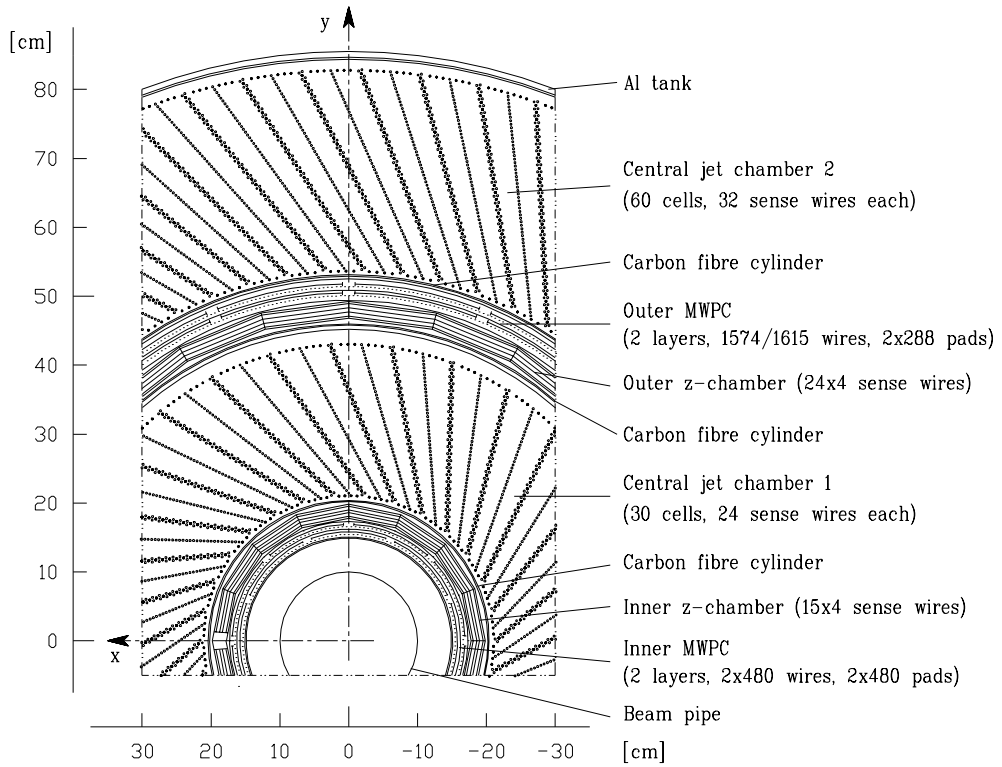

Figure 3.5: Schematic radial view of the Central Tracking Detector CTD, showing the Inner and Outer z-Drift Chambers, the Inner and Outer Multiwire Proportional Chambers and the two Jet Chambers in detail.

each ring containing four sense wires. The sense wire planes of the CIZ are tilted by 45° with respect to the radial direction, while those of the COZ are oriented perpendicular to the beam axis.

Central Inner and Outer Proportional Chambers CIP and COP

The Central Multiwire Proportional Chambers CIP and COP are cylindrical double layer chambers, located inside of the CIZ and outside of the COZ respectively. The CIP, covering a polar angular range of $8° < \vartheta < 172°$, consists of pad cathodes, which are 60-fold segmented in z and eight-fold in φ. Both layers are rotated by 22.5° against each other in order to achieve an effective 16-fold segmentation. The pads of the COP are 18-fold in z and 16-fold in φ. They provide a fast timing signal with a better time resolution than the HERA bunch crossing interval of 96 ns. The signals are used for fast level one and level two trigger decisions (see section 3.3.1). A four-fold coincidence of pads of both double layer chambers leads to a first estimation of the z-position of the vertex.

3.2.2 Central Muon Detector

The instrumented iron of the H1 detector is – besides being the return yoke for the magnetic flux – used as the Central Muon Detector (CMD). It is divided into four regions: the backward end-

cap ($130^\circ \lesssim \vartheta \lesssim 171^\circ$), the backward and the forward barrel ($35^\circ \lesssim \vartheta \lesssim 130^\circ$) and the forward endcap ($4^\circ \lesssim \vartheta \lesssim 35^\circ$). For readout and trigger purposes the entire detector is separated into 64 modules (see figure 3.6). Each module consists of ten 7.5 cm thick iron plates sandwiching ten layers (3-12; including one double layer) of streamer tubes (see figure 3.7). On the inside and outside of the iron six additional layers (0-2,13-15) complement the track measurement and muon identification. Layers 3, 4, 5, 8 and 12 are used for trigger purposes.

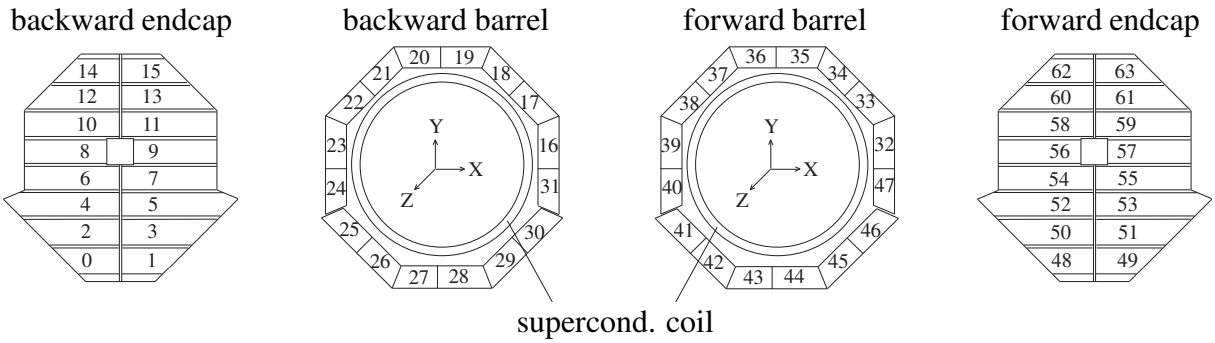

Figure 3.6: The four parts of the Central Muon Detector (backward endcap, backward barrel, forward barrel and forward endcap) divided into 64 modules.

The individual streamer tubes have a cross section of 1 cm $\times$ 1 cm and are of different length depending on the size of the module to which they belong. 8 of these tubes form an profile, two profiles build an element (1 cm $\times$ 16 cm) and several elements form a plane, which is equipped on the outside with strip or pad electrodes. The elements are oriented such that the sense wires are strung parallel to the x-axis in the endcaps and in the z-direction in the barrel region. The strip electrodes are glued perpendicular to the sense wires strung within the tubes in order to provide a two-dimensional measurement. They are 17 mm wide, while the pads are of the size of 25 cm $\times$ 25 cm in the endcaps and 50 cm $\times$ 40 cm in the barrel. The pad electrodes are used to gain calorimetric information on the particles.

The wires and strips are read out digitally. Tracks are reconstructed with information from 16 wire layers, five strip layers and eleven pad electrodes. A spatial resolution of $\sigma_{wire} \approx 3-4$ mm for the wire and $\sigma_{strip} \approx 10-15$ mm for the strip coordinates is achieved. The momentum resolution is only about $\sigma_{q/p} \gtrsim 30\,\%$ for particles in the barrel. In practice the momentum determination for muons is done with the help of linked tracks in the tracking system and not with the Central Muon Detector measurement. More information on the Central Muon Detector and the track reconstruction can be found in [52, 53].

3.2.3 Liquid Argon Calorimeter

The liquid argon calorimeter (LAr calorimeter) is used in this analysis for muon identification. It covers a large polar angle region ($4^\circ \lesssim \vartheta \lesssim 153^\circ$) and is complemented in the backward direction by a backward calorimeter (BEMC until 1994 and SpaCal since 1995) for the detection of the scattered electron[3]. The LAr calorimeter consists of an electro-magnetic and a hadronic part

[3] In the LAr calorimeter itself, the scattered electron is only detected at large Q^2 values (equivalent to large scattering angles).

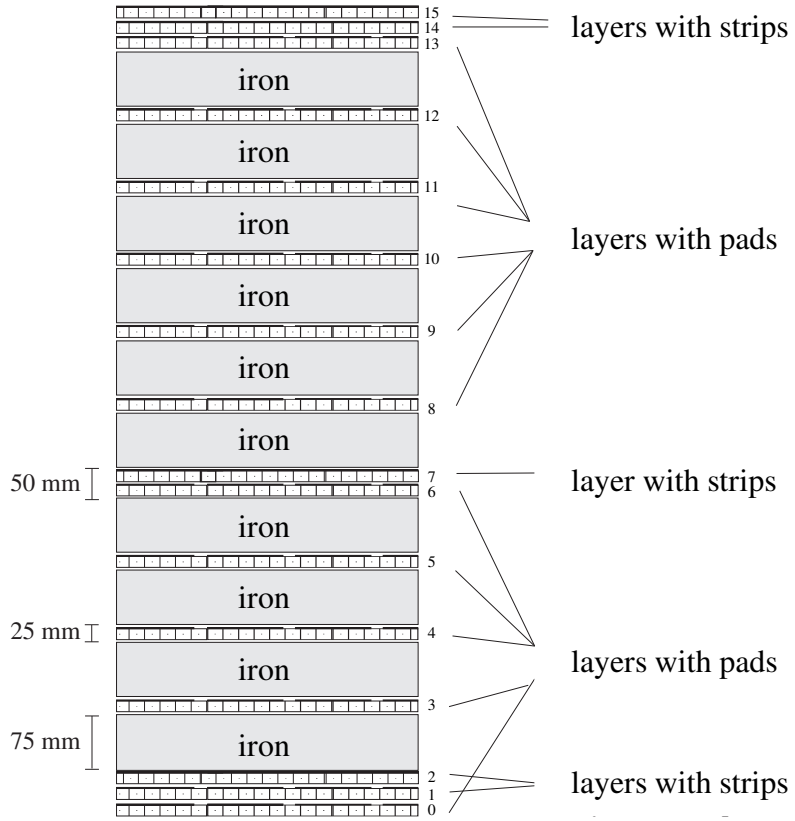

Figure 3.7: Schematic structure of the instrumented iron with its ten layers of streamer tubes equipped with strips or pads (3-12) in between ten layers of iron. On the inside and outside of the iron six additional strip layers (0-2,13-15) complement the track measurement. Layers 3, 4, 5, 8 and 12 are used for trigger purposes.

with lead or high-grade steel absorbers respectively. The depth of the electro-magnetic calorimeter varies with ϑ between 20 and 30 radiation lengths, X_0, while the width of the hadronic calorimeter lies between five and eight interaction lengths, λ. A schematic side view of the LAr calorimeter is given in figure 3.8.

The calorimeter consists of about 45000 electronic channels, with the highest granularity in the forward direction. The energy resolution is $\sigma_E/E \approx 12\,\%/\sqrt{E[\mathrm{GeV}]} \oplus 1\,\%$ in the electromagnetic part and $\sigma_E/E \approx 50\,\%/\sqrt{E[\mathrm{GeV}]} \oplus 2\,\%$ for the hadronic measurement. The H1 LAr calorimeter is a non-compensating calorimeter, which means that the response to hadrons and electrons or photons with the same energy is different. Therefore the measured energy for hadrons is corrected offline. More information about the LAr calorimeter can be found in [54].

3.2.4 Backward Calorimeter

In the backward direction the LAr calorimeter is complemented by a backward calorimeter which is used in this analysis for the exclusion of events with higher Q^2 (see section 4.1.4). In 1994 the Backward Electro-magnetic Calorimeter BEMC allowed the rejection of electroproduction only down to $Q^2 \approx 4\,\mathrm{GeV}^2$. It was a lead-scintillator sampling calorimeter with a depth

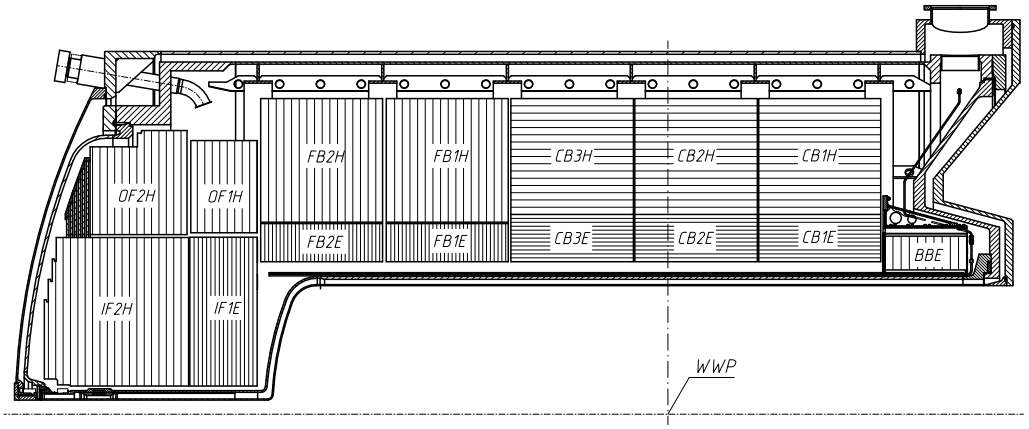

Figure 3.8: Side view of the upper part of the LAr calorimeter divided into electro-magnetic (dark shaded) and hadronic (light shaded) and inner forward (IF), outer forward (OF), forward barrel (FB), central barrel (CB) and backward barrel (BB) parts.

of 22.5 radiation lengths and covered a polar angular region of $151^\circ \lesssim \vartheta \lesssim 177^\circ$. Its energy resolution was determined to be about $\sigma_E/E \approx 10\,\%/\sqrt{E[\mathrm{GeV}]} \oplus 1\,\%$.

In 1995 the BEMC was replaced by the SpaCal, a "spaghetti" type lead-scintillating fibre calorimeter [55, 56, 57]. It covers a polar angular region up to almost $\vartheta = 178^\circ$ and the photoproduction regime can be defined down to $Q^2 = 1\,\mathrm{GeV}^2$. The SpaCal is divided into an electro-magnetic section with a radiation length of $X_0 = 0.91\,\mathrm{cm}$ and a hadronic section with an interaction length of $\Lambda = 25\,\mathrm{cm}$. The electro-magnetic part consists of small cells ($4\,\mathrm{cm} \times 4\,\mathrm{cm}$) resulting in a high spatial resolution and an extremely low noise level (3 MeV). The energy resolution of the SpaCal is about $\sigma_E/E = 7.5\,\%/\sqrt{E[\mathrm{GeV}]} \oplus 1\,\%$ in the electro-magnetic part and $\sigma_E/E \approx 30\,\%/\sqrt{E[\mathrm{GeV}]} \oplus 7\,\%$ in the hadronic calorimeter.

3.2.5 Forward Detectors

In order to separate elastic diffractive from proton dissociative diffractive processes (see section 4.1.1), detector components in the forward direction are used, in which the proton remnant may be detected indirectly. These are the forward part of the LAr calorimeter (below $\vartheta = 10^\circ$), the Proton Remnant Tagger and the Forward Muon Detector.

The **Proton Remnant Tagger** (PRT) consists of seven pairs of scintillators situated around the beam pipe 24 m in front of the interaction region in direction of the proton beam. Each scintillator pair is operated in coincidence mode and shielded with lead. The polar angular acceptance of the PRT is $0.06^\circ \lesssim \vartheta \lesssim 0.17^\circ$ and it can tag the proton remnant, Y, with an efficiency of $\sim 50\,\%$ down to masses of $M_Y \approx 1.6\,\mathrm{GeV}$.

The **Forward Muon Detector** (FMD) complements the CMD in the forward direction, covering polar angles $3^\circ \lesssim \vartheta \lesssim 17^\circ$. It is a spectrometer consisting of six double layers of drift chambers, three on either side of a toroidal magnet providing a field of $1.5 - 1.75\,\mathrm{T}$. The dissociated proton remnant produces signals in the pre-toroidal layers of the FMD with an efficiency of about 70 % down to remnant masses of $M_Y \approx 3\,\mathrm{GeV}$.

3.2.6 Luminosity System

The luminosity system of H1 is used for a fast online relative luminosity determination and to control the electron beam steering and monitoring by HERA, as well as for the absolute luminosity measurement after applying offline corrections [58]. It is located close to the beampipe downstream in the direction of the electron beam as shown in figure 3.9. It consists of an Electron Tagger (ET) at -33 m and a Photon Detector (PD) at -103 m. The luminosity is measured during the data taking by the Bethe-Heitler process $ep \to ep\gamma$ [59], which has a large and well known cross section and is insensitive to the internal proton structure. The final luminosity is measured using only the photon.

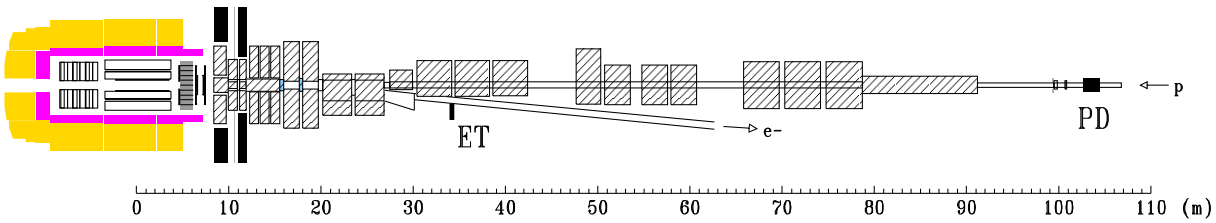

Figure 3.9: The H1 luminosity system, consisting of an Electron Tagger at -33 m and a Photon Detector at -103 m behind the interaction zone in the electron direction.

As a signature of a Bethe-Heitler event, the scattered electron in the ET and the outgoing photon in the PD are required simultaneously. The main background are bremsstrahlung processes with the residual gas in the beampipe ($eA \to eA\gamma$). These events are estimated to contribute at the level of 10 % of the $ep \to ep\gamma$ rate [58] and can be subtracted using data from the electron pilot bunches, which do not interact with corresponding proton bunches.

The luminosity is then given by

$$\mathcal{L} = \frac{R_{tot} - (I_{tot}/I_0)R_0}{\sigma_{vis}}, \tag{3.1}$$

where R_{tot} is the measured total rate of bremsstrahlung processes, R_0 the measured bremsstrahlung rate in the pilot bunches, I_{tot}/I_0 the ratio of the corresponding beam currents and σ_{vis} the visible part of the Bethe-Heitler cross section, allowing for acceptance and trigger efficiencies.

3.3 Trigger Scheme

Due to the small cross sections in ep physics, large beam currents and a high bunch crossing rate are needed. In parallel large background rates from synchrotron radiation, proton–gas interactions, proton–wall interactions and cosmic muons are present. The total rate of background events is about a factor 1000 higher than genuine ep interactions. On the other hand, bunch crossings with a rate of 10.4 MHz happen much faster than the entire detector can be read out. Therefore H1 uses a partially pipelined four level trigger system (L1, L2, L4 and L5) in order

to minimize dead time. Trigger levels L1 and L2 are online hardware triggers, while L4 is an online software trigger and L5 is an offline software classification, where already the entire detector information is available. The outline of the multi-level trigger scheme together with the relevant rates and decision times is given in figure 3.10.

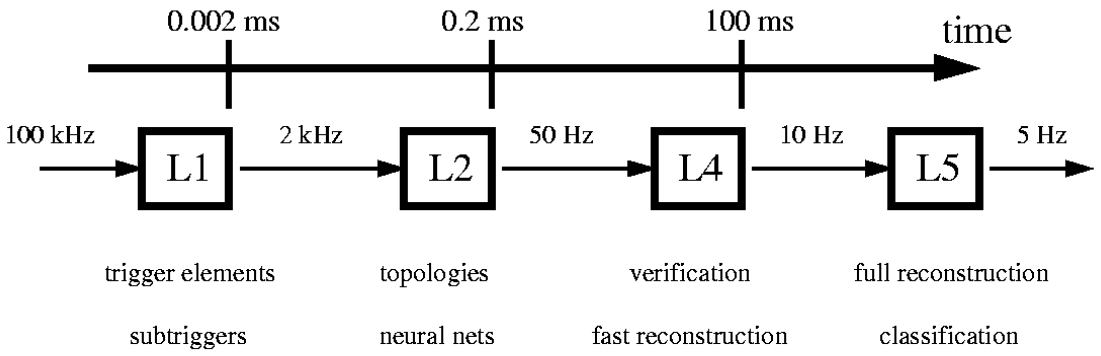

Figure 3.10: Trigger levels used during 1994 to 1997 data taking. Shown are typical rates and decision times for each level. The given keywords are explained in the text.

3.3.1 First Trigger Level L1

The first level trigger L1 is pipelined in order to collect data from all different subdetectors. The output from all subsystems is stored in pipelines for 24 bunch crossings (2.3 μs). Trigger information from the subdetectors are combined to give 128 *subtriggers*. If an event fulfils one out of these 128 trigger conditions, an *L1 keep* signal is sent to all different subsystems, the pipeline is frozen and the detector information is read out. The resulting dead time between the L1 keep signal and the complete readout lasts typically $1-2$ ms per event. The L1 trigger reduces the rate by roughly a factor of 50. The 128 subtriggers are composed of 192 trigger elements delivered by various subdetectors. Those trigger elements and subtriggers which are essential for the analysis presented here will be described in the following.

For an analysis a high statistics data sample is desirable, but existing triggers for heavy vector mesons in photoproduction have relatively low efficiencies ($20-70\%$) since they are based on lepton signatures or on the topology of these events or they are heavily downscaled. Therefore it is essential to combine several triggers in order to achieve a higher trigger efficiency and thus obtain more events. On the other hand this set of triggers should be chosen to have a stable trigger setting and to have independent triggers for the determination of trigger efficiencies.

In the J/ψ analysis events are accepted which are triggered by one out of two different L1 triggers (`s34` or `s54`), and in the Υ analysis by at least one of six (`s15`, `s18`, `s19`, `s22`, `s34` and `s54`) depending on the year (table 6.1). The exact definitions of all six triggers are given in table 3.1.

The two triggers used in the J/ψ analysis have been relatively stable both in definition and in rate (see figure 3.11) during the data taking periods 1996 and 1997. The purpose of the different L1 subtriggers is given in the following:

$J/\psi, \Upsilon \to \mu\mu$	
s34	Mu_Bar $\wedge$ DCRPh_Ta $\wedge$ DCRPh_TNeg $\wedge$ DCRPh_THig $\wedge$ (zVtx_small $\vee$ zVtx_Cls) $\wedge$ (zVtx_small $\vee$ zVtx_sig)
s54	Topo_BR $\wedge$ DCRPh_TNeg $\wedge$ DCRPh_THig $\wedge$ zVtx_Cls
$\Upsilon \to \mu\mu$	
s15	(Mu_Bar $\vee$ Mu_ECQ) $\wedge$ DCRPh_THig $\wedge$ zVtx_sig
s18	Mu_ECQ $\wedge$ DCRPh_Ta $\wedge$ (zVtx_small $\vee$ zVtx_sig)
s19	Mu_Bar $\wedge$ DCRPh_Ta $\wedge$ (zVtx_small $\vee$ zVtx_sig)
s22	Mu_BEC $\wedge$ (zVtx_small $\vee$ zVtx_sig)

Table 3.1: Full definitions of L1 subtriggers used for the J/ψ and Υ analyses. Each subtrigger used here is composed out of different trigger elements from the specific subdetectors. For all the subtriggers in addition several veto conditions are applied, mostly concerning the timing of the event.

s15 inclusive muon trigger with one muon candidate anywhere in the detector, one high momentum track candidate and a reconstructed vertex

s18 inclusive muon trigger with one muon candidate in one of the endcaps of the CMD, one central track candidate and a reconstructed vertex

s19 inclusive muon trigger with one muon candidate in the barrel of the CMD, one central track candidate and a reconstructed vertex

s22 inclusive muon trigger with one muon candidate in the backward endcap of the CMD, no track candidate required and a reconstructed vertex

s34 inclusive muon trigger with one muon candidate in the barrel of the CMD, one central track candidate with a curvature corresponding to a negatively charged particle, one high momentum track candidate and a reconstructed vertex corresponding to a low track multiplicity

s54 topological trigger with two back-to-back track candidates, one central track candidate with a curvature corresponding to a negatively charged particle, one high momentum track candidate and a reconstructed vertex

Muon Trigger

For the muon trigger information from all 64 modules of the Central Muon Detector is collected. Only five of the 16 layers of the instrumented iron are used for trigger purposes (see section 3.2.2). While in the barrel of the CMD two out of the inner four layers have to be hit

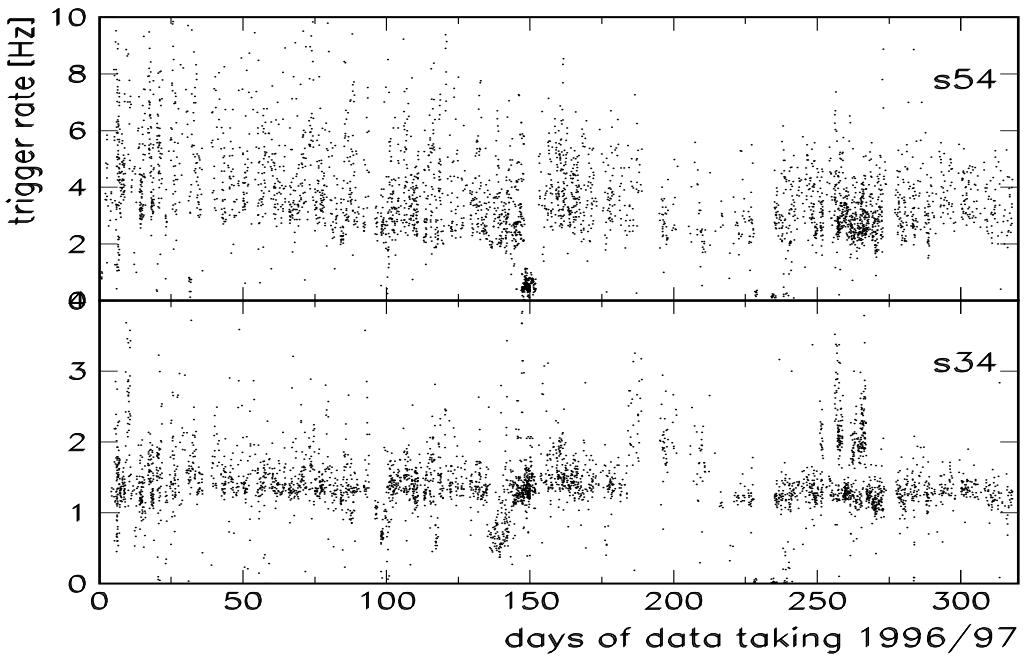

Figure 3.11: L1 trigger rates for J/ψ triggers `s54` and `s34` over the entire 1996/1997 data taking period. Note that the L1 rates still have significant contributions from cosmic background.

within one module in order to set the trigger element, in the endcaps three out of five layers are required (with some further restrictions near the beam pipe due to a higher background level).

Central Drift Chamber Trigger

The central drift chamber trigger (`DCRPhi` trigger) is able to find tracks of charged particles in the $r\varphi$-projection. Ten out of the 56 wire layers of CJC1 and CJC2 are used for trigger purposes. About 10000 predefined masks are compared to the digitised hits thus defining four different types of trigger elements: low momentum track candidates ($0.45 \lesssim p_t \lesssim 0.8\,\text{GeV}$) and high momentum track candidates ($p_t \gtrsim 0.8\,\text{GeV}$) for negative and positive charges.

z-Vertex Trigger

The z-vertex trigger provides a rough estimate of the z-position of the event vertex. For this purpose the pad signals of the multiwire proportional chambers CIP, COP and the first forward proportional chamber FPC are combined into *rays*. A ray is defined as the coincidence of four pad signals that can be connected by a straight line in the rz-plane. The number of these rays enters a 16 bin wide histogram, where each bin is related to the origin of its respective rays along the z-axis. The resulting 16 histograms (one for each φ sector) are combined to give the z-vertex histogram. It covers a range of $\pm 44\,\text{cm}$ in z around the nominal interaction point. The bin with the most entries is expected to contain the interaction vertex of the ep collision (see figure 3.12).

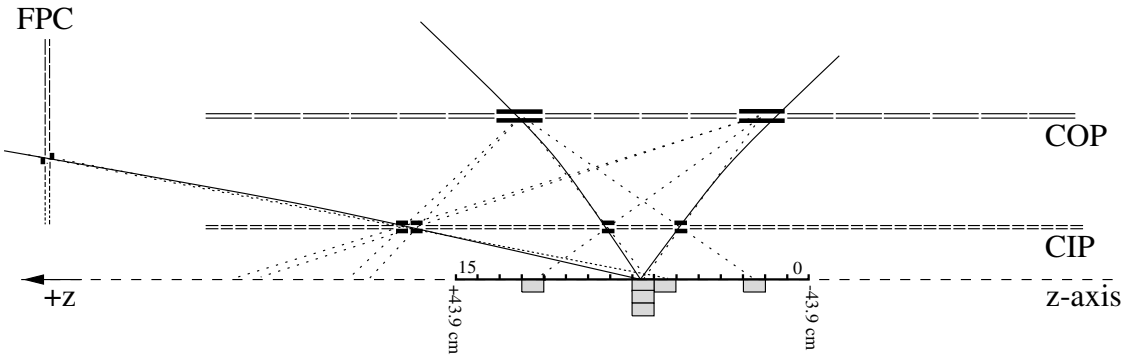

Figure 3.12: The z-vertex histogram in the rz-view for one φ sector is shown. Rays originating from genuine particles are indicated by full lines, while the dotted lines indicate the wrong combinations.

Topological Trigger

The trigger element `Topo_BR` is built from the *rays* of the proportional chambers, which have already been used with a finer granularity to fill the z-vertex histogram. These so-called *big rays* are defined in 16 φ and 14 ϑ bins. Two big rays in roughly opposite directions are required to set the topological trigger element `Topo_BR`.

3.3.2 Second Trigger Level L2

On the second level of the H1 trigger scheme events accepted by certain L1 subtriggers are validated by means of two different strategies: the L2 topological trigger and the L2 neural network trigger. While the former is programmed to be sensitive to topological features of specific final states, the latter consists of neural networks, which are designed and trained to separate distinctive physics channels from background in a multi-dimensional space defined by dedicated input quantities.

In the first half of the 1996 data taking period, additional L2 conditions, namely neural network triggers, were applied for `s54`. One of two different neural nets (`n2`$\vee$`n4`) has to accept events triggered by `s54`. The neural networks are trained with J/ψ candidates from the beginning of 1996. They are designed to be sensitive to the *back-to-back* in $r\varphi$ topology of these events as well as to muon signatures in the instrumented iron or the LAr calorimeter and on the low multiplicity structure of diffractive heavy vector mesons. They were trained to distinguish these events from general DIS events and non-ep background, while they do not reject background from cosmic showers efficiently due to the similar event structure. A major part of the remaining background is subsequently rejected on the fourth trigger level L4. The exact definitions of the input quantities for the neural nets are given in table 3.2. Information on the efficiency of this trigger level for heavy vector mesons as analysed here is provided in section 4.3.1.

The definitions of the input quantities for the neural nets are as follows:

CJC: TRHINEG=number of φ sectors with at least one high momentum ($p_t > 0.8\,\mathrm{GeV}$) track candidate with a curvature corresponding to a negatively charged particle

TRHIPOS=same as TRHINEG but for positively charged particles
TRLONEG=same as TRHINEG but for low momentum particles ($0.4 < p_t < 0.8\,\text{GeV}$)
TRLOPOS=same as TRLONEG but for positively charged particles
TRTOT=total number of trigger masks set

z-vertex: CPVSUM=total number of entries in the z-vertex histogram
CPVPOS=position of the histogram bin with the largest number of entries
CPVMAX=number of entries in the CPVPOS bin

LAr: LARIFE=total energy in all modules of the inner forward part of the LAr calorimeter
LARFBE=total energy in all modules of the forward barrel part of the LAr calorimeter
LARCBE=total energy in all modules of the central barrel part of the LAr calorimeter

CMD: IRONFB=number of hit modules in the forward barrel part of the instrumented iron
IRONBB=number of hit modules in the backward barrel part of the instrumented iron
IRONTOT=total number of hit modules in the instrumented iron

input quantities for used neural nets	
CJC information	TRHINEG, TRHIPOS, TRLONEG, TRLOPO (`n2` and `n4`) TRTOT (only `n2`)
z-vertex information	CPVSUM, CPVPOS, CPVMAX (`n2` and `n4`)
LAr information	LARIFE, LARFBE, LARCBE (`n2` and `n4`)
CMD information	IRONFB, IRONBB, IRONTOT (`n2` and `n4`)

Table 3.2: Input quantities for the two L2 neural nets filtering `s54` events. Information is used from those subdetectors on which the L1 trigger decision was already based.

The rate reduction on the second trigger level for events with `s54` as an L1 trigger is about 60 % for the 1996/1997 data taking periods.

3.3.3 Fourth Trigger Level L4

The fourth trigger level is realized as an asynchronous software trigger with complex event reconstruction and selection algorithms. A fast version of the final H1 reconstruction program is run, allowing for more detailed event information than on the previous trigger levels.

In this section an overview of the L4 scheme is given which has to be passed by all events; the layout of this scheme is sketched in figure 3.13. Each triggered event fulfilling one or more L1 and L2 trigger conditions has to pass the *trigger verification* on L4, where L1 trigger elements are mimicked in order to verify the L1 decision on the basis of more detailed and more precise detector information. If the L1 decision is confirmed by this trigger verification, an event is kept if it fulfils either one of the *hard scales* or if it is recognized by one of the *finders* which are devoted to special final state signatures. Events which are not saved by one of these two

branches are downscaled according to a Q^2 *dependent scheme*[4]. For a more detailed description of this trigger level see [60, 61].

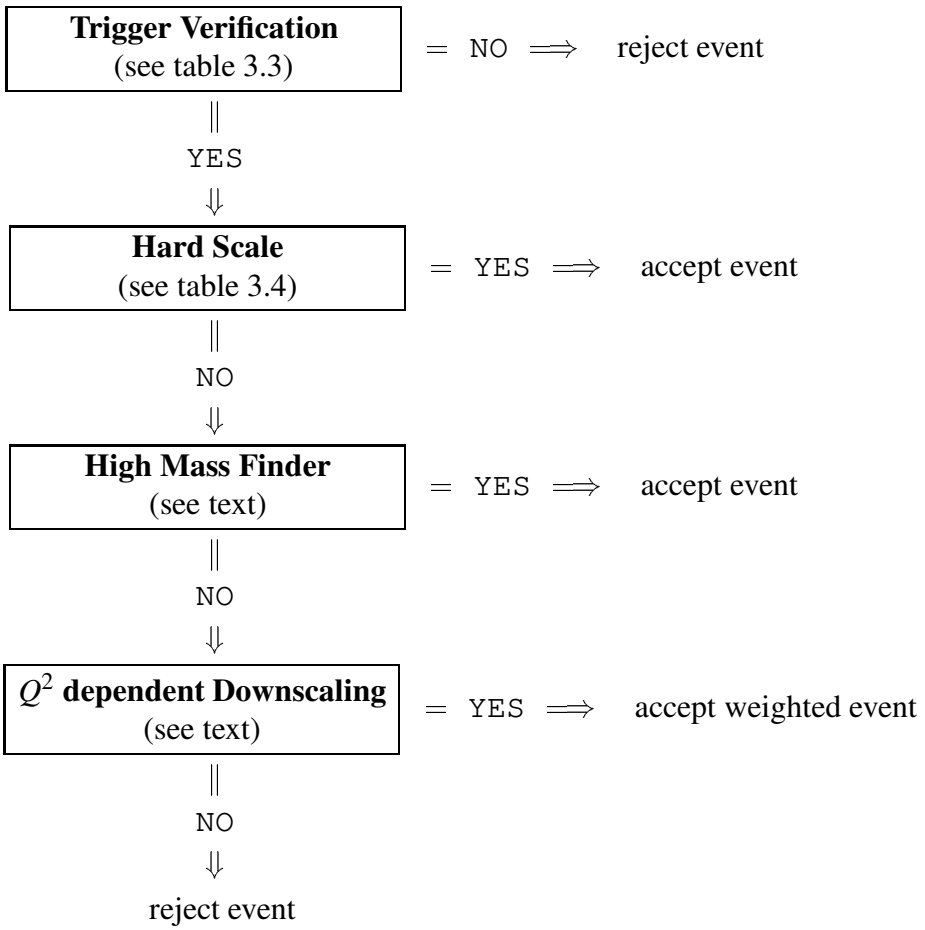

Figure 3.13: Schematic illustration of the L4 scheme including the steps which are important for this analysis. After the last step only weighted events are kept, where the weight reflects information about the number of similar rejected events.

Trigger Verification

The trigger verification requires some global event quantities to be fulfilled as well as distinctive features such as track multiplicities and muon signatures, already applied on the first trigger level. The reconstructed event vertex has to lie within 50 cm of the nominal interaction point (in z-direction). A *beam-gas* finder as well as a *cosmic* finder are applied as veto conditions in order to reject non–ep background. Finally, certain L1 conditions (trigger elements) are mimicked depending on which L1 trigger is set for the event considered.

If all conditions for a certain trigger are fulfilled it is verified, otherwise it is reset. After the

[4]These steps are only valid for 1997 data taking onwards; until 1996 only the trigger verification had to be passed for an event to be kept.

trigger verification step at least one L1 trigger has to be verified in order to process the event further. Otherwise, if all triggers are reset, the event is rejected. An overview of the trigger verification for the L1 trigger elements used in the present analyses is given in table 3.3.

When a track, measured in the central drift chambers, fulfils the following criteria it is defined as a *good* central track with respect to the trigger verification on L4: more than eight hits associated with the reconstructed track, the first hit of the track lies within a radial distance to the beam axis (R_{start}) of less than 30 cm, a radial track length (L_{radial}) of at least 10 cm and a distance in the xy-plane to the nominal vertex of $|d_{ca}| < 4$ cm is found.

Trigger Verification	
z-vertex position	
s15 - s54	a reconstructed central vertex
Mu_ECQ, Mu_BEC, Mu_Bar	
s15 - s34	the data bank containing reconstructed tracks in the instrumented iron (ITKR) has to be present, this means that at least one track has to be found in the CMD
Mu_Bar	
s19, s34	one *matched* muon with $\Delta\vartheta < 0.2$ rad
DCRPh_THig	
s15 - s54	at least one *good* central track (definition see text) with a reconstructed curvature corresponding to a transverse momentum of more than 0.6 GeV
DCRPh_Tc	
s19, s22	at least three *good* central tracks
DCRPh_TNeg	
s19, s22	at least one *good* central track corresponding to a negatively charged particle

Table 3.3: Trigger verification as applied on L4 to the L1 triggers used here. In addition to global event features (see text) the conditions described are required in order to mimic the main L1 trigger elements indicated (see also table 3.1).

Hard Scale Selection

Hard scales are based on event properties which show that a hard subprocess was potentially involved in the respective event, e.g. particles with a high momentum, high energy jets or a large momentum transfer Q^2. Those hard scales which save vector mesons decaying muonically in photoproduction are listed in table 3.4.

Hard Scale Selection
one track with $p_t > 2\,\text{GeV}$
one *matched* muon with $\Delta\vartheta < 0.2\,\text{rad}$ and $p_t > 1\,\text{GeV}$

Table 3.4: Hard scale selection on L4 for muonic decays of vector mesons in photoproduction.

A *matched* muon means that a combination of a central drift chamber track and a track reconstructed in the iron detector is found with an angular difference of $\Delta\vartheta < 0.2\,\text{rad}$ and $\Delta\varphi < 0.5\,\text{rad}$. If at least one of the two hard scale conditions is fulfilled the event is kept and sent to the offline event reconstruction and classification (L5), otherwise the event is subjected to dedicated *finders*.

High Mass Finder

If an event is not rejected by the trigger verification and if it is not accepted by one of the hard scales, the decision of several dedicated *finders* is calculated until one of them accepts the event. If none of the finders recognizes the event as belonging to the physics class it is looking for, the event enters a prescale scheme by which it is downscaled according to its Q^2. The majority of muonically decaying heavy vector mesons is saved either by the *high p_t track hard scale* or by the *high mass finder*.

The *high mass finder* for the central region uses the full CJC reconstruction software. A loop over *good* central tracks (definition see table 3.5) is performed and for each pair of tracks the invariant mass, M_{tt}, is calculated. If a combination is found with an invariant mass of at least 2 GeV, the event is accepted by the *high mass finder*.

Events that do not fulfil either the *hard scale* or the *high mass finder* are downscaled according to their Q^2. For photoproduction events of this type the downscale factors are rather high (about 40). Events which pass L4 only by the downscaling scheme are assigned a weight accordingly. But since the cuts which have to be fulfilled on the different trigger levels are almost completely repeated and mostly sharpened in the offline analysis, no event with a weight greater than one is found in the final data sample. The fourth trigger level can therefore to a good approximation be considered as 100% efficient for the present analysis.

3.3.4 Fifth Trigger Level L5

The fifth trigger level, which is an event classification performed offline, comprises a full event reconstruction as well as a classification scheme which assigns all events accepted by L4 to one or more predefined physics classes. Events which cannot be classified are rejected. The L5 selection for heavy vector mesons splits the data into three different classes, one for the muonic decays (class 24), one for the electronic decays (class 17) and a third one without lepton identification (class 18) for efficiency determination. In this analysis only those events

Good Central Track Criteria – High Mass Finder	
$R_{start} < 45\,\text{cm}$	
$\lvert Z_{vertex}\rvert < 40\,\text{cm}$	
$\lvert d_{ca}\rvert < 2\,\text{cm}$	
$N_{hits} > 9$	if $25^\circ < \vartheta < 160^\circ$
$N_{hits} > 4$	if $\vartheta < 25^\circ$ or $\vartheta > 160^\circ$
$L_{radial} > 10\,\text{cm}$	if $25^\circ < \vartheta < 160^\circ$
$L_{radial} > 5\,\text{cm}$	if $\vartheta < 25^\circ$ or $\vartheta > 160^\circ$

Table 3.5: Given are the criteria for tracks being *good* central tracks as required by the *high mass finder*, with R_{start} being the radial distance between the beam axis and the first hit on the track, N_{hits} the number of hits associated with the track and L_{radial} the track length in the $r\varphi$-plane.

are taken into account which are assigned to one of these three classes[5], and all cuts applied on L5 are repeated later on to ensure full consistency. With the help of simulated J/ψ events the efficiency of the fifth trigger level classification for the selected heavy vector mesons is determined to be 100%. For a loose selection only eight events out of 20000 were found which were not classified.

3.4 Muon Identification

The principle of muon identification in the central H1 detector is to look for a vertex fitted track in the inner track chambers, which can be linked either to an energy deposition in the LAr calorimeter compatible with that of a minimal ionizing particle or to a reconstructed track in the instrumented iron detector. In order to achieve a good background suppression of misidentified hadrons certain quality criteria have to be fulfilled by measured tracks, clusters and links. The linking procedure and the identification criteria are described in the following. How many and how well decay muons have to be identified in the final analyses is different in the case of J/ψ and Υ mesons and depends on the type of measurement. This is described in detail in section 3.4.3.

The two different muon identification methods become efficient at different muon momenta. In the case of J/ψ mesons decay muons identified in the LAr calorimeter have a mean momentum of 1.8 GeV, whereas the identification of muons in the iron gets efficient at about 2 GeV with a mean momentum of 3 GeV. Typical distributions of the momenta of decay muons from heavy vector mesons are shown in figure 3.14.

For tracks in the central region of the H1 detector many performance, efficiency and systematic studies have already been performed. Therefore the knowledge of precision of certain variables

[5] The selection of the electronic decay channel is used for a systematic comparison with the muon selection at some points of the analysis.

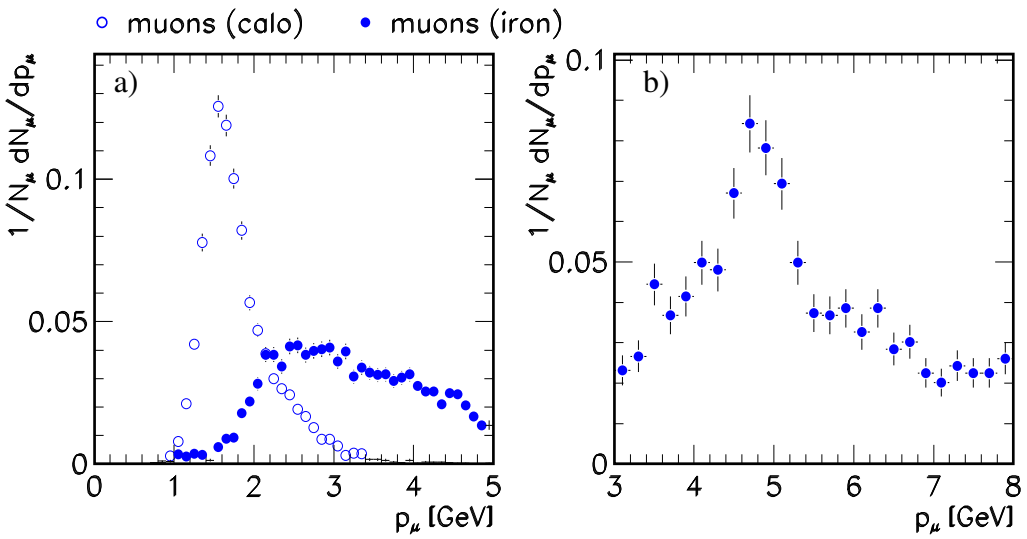

Figure 3.14: Typical reconstructed momenta of decay muons from a) J/ψ and b) Υ mesons. The muons are identified in the instrumented iron or in the calorimeter. The events are from a DIFFVM Monte Carlo passing a loose selection.

like angles and momenta is rather high [62, 63]. For a more detailed description of the muon identification see [64, 65, 66].

3.4.1 Muon Identification in the LAr Calorimeter

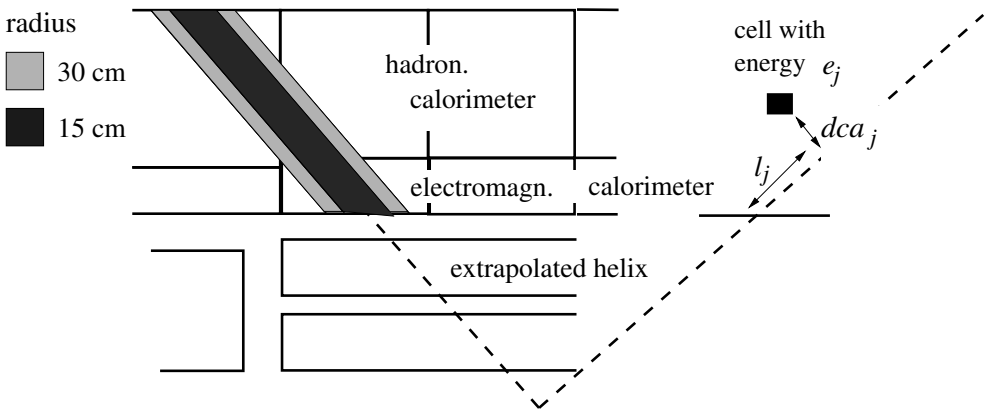

Figure 3.15: Schematic illustration of muon identification in the LAr calorimeter.

Tracks measured in the central tracking system (inner tracks) are extrapolated into the LAr calorimeter taking into account the bending in the magnetic field, energy loss due to ionisation and multiple scattering. Two concentric cylinders with radii of $R_A = 15\,\text{cm}$ and $R_B = 30\,\text{cm}$ are constructed around the extrapolated tracks; the deposited energy in these cylinders has to fulfil certain criteria. The radii are chosen such that muons deposit almost all their energy within

the inner cylinder and that hadronic showers initiated by pions (which constitute the majority of the background) are contained within the outer cylinder. For illustration of this method see figure 3.15. All energies used here are on the "final" energy scale, which already contains dead material correction, topological noise suppression and reweighting of hadronic energy deposits to compensate for the different calorimeter response for electrons or photons and hadrons.

The exact criteria for muon identification in the LAr calorimeter are listed below:

- Energy must be deposited (above noise level) in at least three cells of the LAr calorimeter within $R = 40\,\text{cm}$ around the extrapolated track .
- The outermost calorimeter cell within the cylinder R_A must have a certain minimum distance l_j from the impact point of the extrapolated track.
- The sum of distances l_j between the track impact point and all involved hadronic cells within R_A has to be large. This ensures that the particle has penetrated the calorimeter far enough so that the majority of pions with low momenta is rejected, although muons with momenta below 1 GeV are also suppressed.
- The deposited electro-magnetic energy within R_A and the sum of electro-magnetic and hadronic energy within R_B have to be small enough in order to reject further pionic background. For these sums only cells with at least 0.01 GeV energy deposition are taken into account.

All four cut values depend on the reconstructed polar angle of the inner track in order to take the detector geometry into consideration. They are also optimized to account for a weak momentum dependence. Finally, a weighted sum of all individual deviations of the cut quantities from the cut values is calculated. This sum then defines how well a particle is identified as a muon; they are classified into four groups: not a muon, *badly identified* (quality 1), *medium* (quality 2) or *well identified* (quality 3) muon. Depending on the background situation in a specific analysis channel these categories are used.

3.4.2 Muon Identification in the Instrumented Iron

Inner tracks measured in the Central Track Detector are extrapolated into the Central Muon Detector similar to the method described in the previous section. These tracks have to fulfil certain quality criteria:

- The curvature κ has to be small enough (large momentum particle) to ensure that the particle can reach the muon detector:

$$|\kappa| < \frac{0.003\,\text{cm}^{-1}}{\sin\vartheta}\,,$$

  depending on the polar angle ϑ of the track.

- The angular differences between the inner track (subscript c) and the outer track reconstructed in the instrumented iron (subscript μ) have to fulfil the following requirements:

$$|\vartheta_c - \vartheta_\mu| < 0.25\,\text{rad} \qquad \text{and} \tag{3.2}$$

$$-\frac{\pi}{2} < q \cdot \sin(\varphi_\mu - \varphi_c) < 0.2\,. \tag{3.3}$$

  Bending due to the magnetic field is taken into account by this asymmetric cut. The angles ϑ_μ and φ_μ are defined by a straight line between the first measured point in the Central Muon Detector and the event vertex. q denotes the charge of the muon (± 1) measured in the inner trackers.

For each pair of inner tracks (drift chamber) and outer tracks (instrumented iron) a χ^2 is calculated as follows:

$$\chi^2 = \left(\vec{X}_e - \vec{X}_m\right)^T V^{-1} \left(\vec{X}_e - \vec{X}_m\right) \text{ with } V = V_e + V_m,$$

with the components of $\vec{X}_e$ being the parameters of the extrapolated inner track and $\vec{X}_m$ those of the outer track in the muon system. Errors of track parameter measurements and their correlations are taken into account by means of covariance matrices V_e (inner track) and V_m (outer track). The track parameters $\vec{X}_e$ and $\vec{X}_m$ used depend on the region of the instrumented iron where the outer track is reconstructed. In the barrel the first measured hit belonging to the reconstructed outer track and the direction of the muon within the iron[6] are used, in the endcaps the spatial coordinates and the azimuthal angle are taken.

The probability $P(\chi^2)$ for a pair of inner and outer tracks to stem from the same muon can be obtained by integrating the density function $\mathcal{F}(\chi^2, N)$ of the χ^2 distribution [67]:

$$P(\chi^2) = \int_{\chi^2}^{\infty} \mathcal{F}(Z, N)\, dZ,$$

with N being the number of degrees of freedom. Track pairs with $P(\chi^2) > 0.0001$ are considered as muon candidates for the analysis. In the case of several link hypotheses the one with the highest χ^2 probability is chosen.

3.4.3 Muon Selection

Depending on the measurement different sets of cuts for the muon identification are applied. Two categories of cuts, A and B, can be defined, for which the specific muon identification criteria are given in table 3.6.

In the case of the J/ψ cross section measurement as a function of $W_{\gamma p}$ and the measurement of the Regge trajectory for elastic J/ψ mesons, the relatively weak cuts as in category A are

[6] The direction is calculated from the slope measured in the wire layers: $\tan\alpha_{yz} = \tan\vartheta \sin\varphi$.

used. This is because the number of signal events is determined by fitting the mass spectra. However, for the measurement of the slope parameter (category B), where the $|t|$ distribution is directly corrected for background contributions, all background has to be described by the LPAIR Monte Carlo generator. Therefore all non-resonant but "non-LPAIR" background such as misidentified hadrons has to be rejected. This is achieved by applying harder cuts on the muon identification using the cuts of category B (see figure 4.7).

In the case of the Υ analysis the same cuts (category B) are required due to the bad signal-to-background ratio. The weak lepton identification criteria as applied in the pre-selection (line four in table 4.2) and used for systematic studies are given in addition (category C).

A	B	C
$\geq 1\mu$ in the iron or in the LAr (quality=3) or $= 2\mu$ in the LAr (quality≥ 2)	$= 2\mu$ in the iron or in the LAr (quality=3)	$\geq 1\mu$ in the iron or in the LAr (quality≥ 2)

Table 3.6: Different sets of muon identification criteria as applied for the different measurements in this analysis (categories A and B). Category C is used in the pre-selection (weak muon identification cuts, see line four in table 4.2).

For muons identified in the barrel of the instrumented iron at least three hits have to be associated with the reconstructed muon track. In the case of backward going muons ($\vartheta \geq 135^\circ$) six hits are required in order to suppress misidentified hadrons. These are particularly numerous in the backward part of the detector because there is only little material in front of the instrumented iron. This additional cut is only applied for the categories A and B.

For J/ψ events only triggered by `s34` at least one muon has to be identified in the barrel of the instrumented iron, since already on L1 a muon signal in the barrel is required (see section 3.3.1).

Chapter 4

Selection of Diffractive J/ψ Mesons

In this chapter the data selection and the technical aspects of the J/ψ analysis are presented. In the first section the selection chain and the resulting data set are described. Afterwards the method of correcting the data for acceptance and efficiency losses is given. Examples from the extensive comparison between the Monte Carlo simulation and the data are shown. Finally, studies of systematic effects are discussed. The results derived from this analysis will be given in chapter 5.

4.1 Selection of Diffractive J/ψ Events

In this section the selection chain of diffractively produced J/ψ mesons is discussed. It starts from data that have passed the complete trigger scheme (L1-L5). Emphasis is placed on the separation of elastic ($\gamma p \to J/\psi p$) and proton dissociative ($\gamma p \to J/\psi Y$) production mechanisms by means of characteristic event signatures. Afterwards the run selection, the luminosity used and the accessible kinematic region are described. Finally the dominant background and its suppression is discussed and the resulting data set is summarized.

4.1.1 Selection of Diffractive Events

Diffractive production of vector mesons comprises elastic events with only the vector meson and the scattered beam particles in the final state and dissociative events with the vector meson, the scattered positron and the dissociated proton in the final state. In contrast to non–diffractive events the region between the proton direction of flight and the hadronic final state (the vector meson) is empty (rapidity gap) due to a lack of colour flow in between. Thus one characteristic of diffractive events is an empty detector with at most the scattered positron, the scattered proton or the dissociated proton remnant and the hadronic final state detected. Since in this analysis J/ψ mesons are reconstructed via their muonic decay and only photoproduction is considered, diffractive events are selected by requiring nothing but the two oppositely charged

decay muons of the J/ψ meson allowing at most for the scattered proton[1] or the indirect signals from its dissociated remnant as described below. An example of an elastically produced J/ψ candidate decaying into two muons is shown in figure 4.1, a proton dissociative J/ψ candidate in figure 4.2. In order to achieve reasonable muon identification and measurement of angles and momenta only the central part of the tracking detector is used ($20^\circ \leq \vartheta_\mu \leq 160^\circ$), where the track measurement is well understood.

In order to measure the elastic part of diffractively produced vector mesons one has to distinguish between events with a scattered proton and those where the proton has dissociated. For the majority of dissociative events part of the proton can be detected via secondary interactions in the material surrounding the beam by means of several detectors in the forward direction. Information from the forward part of the LAr calorimeter ($\vartheta \leq 10^\circ$), the pre-toroid hit pairs in the FMD and hits in the counters of the PRT are used for this purpose. PRT counters one, two, three and seven are used for 1996 data and one, two and three for 1997 data.

An event is classified as *forward untagged* when the energy deposition in the LAr calorimeter in the forward direction ($\vartheta \leq 10^\circ$) is below 0.75 GeV, if not more than one hit pair in the pre-toroidal FMD is found and if none of the chosen PRT counters is set. The event is classified as *forward tagged* when one of these conditions is not fulfilled. All three detectors are sensitive to different regions of the mass M_Y of the dissociated system as shown in figure 4.3.

4.1.2 Run Selection

In order to have reliable and reproducible conditions, a run[2] selection has to be applied. It is required that all major detector components which are used for this analysis were fully operational for the time data were taken, that is their high voltage must have been switched on and they must have been in the readout. In addition only runs in later periods of a luminosity run (phase 2 - phase 4) are analysed, where photoproduction triggers with a high rate have reasonably low prescale factors.

In a final run selection, about 6 % of 1996 luminosity has to be excluded from the analysis due to a malfunctional muon trigger (runs 168200-169814). Due to inadequate performance of the Forward Muon Detector the run range 177920-184256 in the beginning of 1997 corresponding to 6.7% of 1997 luminosity is excluded from the analysis. In addition no runs with special trigger settings (e.g. minimum bias runs) or a systematically shifted z-vertex position are used (final run selection).

4.1.3 Luminosity

The integrated luminosity finally analysed is $20.9 \pm 0.3\,\mathrm{pb}^{-1}$ for the data taking periods 1996 and 1997. To obtain this number one has to correct the total luminosity collected by H1 for several losses. A detailed listing of these corrections is given in table 4.1, separately for 1996

[1] The scattering angle of the proton is very small and the proton is not measured in the main H1 detector.

[2] The term *run* is used for a unit of data taking in which all detector, trigger and background conditions are roughly constant; the typical duration of a *run* is about 20 minutes.

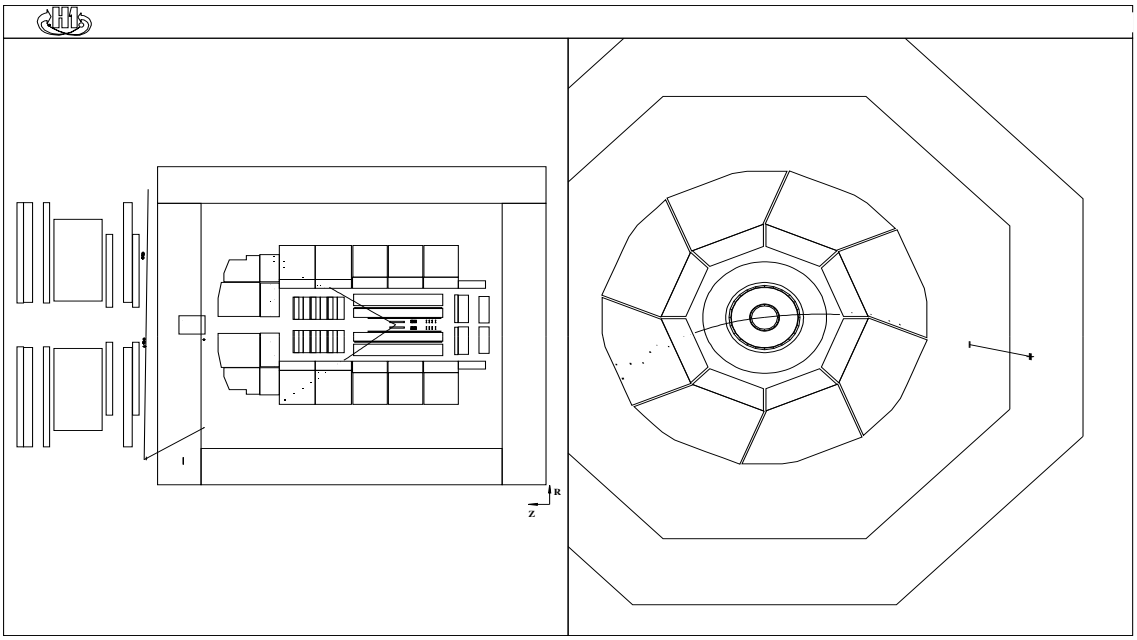

Figure 4.1: Schematic view of a typical event candidate for the process $\gamma \to J/\psi p, J/\psi \to \mu\mu$; on the left hand side the side view of the H1 detector is shown and on the right hand side the radial view. Except for the two decay muons (one detected in the LAr calorimeter and in the instrumented iron, the other one only in the LAr calorimeter) the detector is empty; the invariant mass of the two muon system is 3.17 GeV.

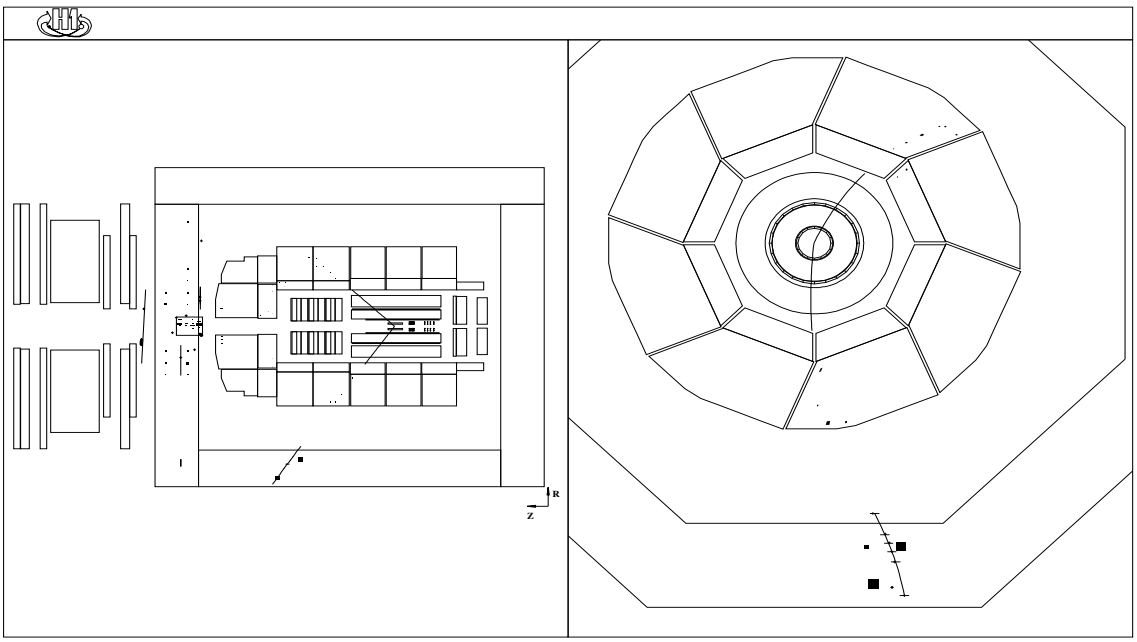

Figure 4.2: Schematic view of a typical event candidate for the process $\gamma p \to J/\psi Y, J/\psi \to \mu\mu$; on the left hand side the side view of the H1 detector is shown and on the right hand side the radial view. Besides the two decay muons (one detected in the LAr calorimeter and in the instrumented iron, the other one only in the LAr calorimeter), signals in the forward direction due to the proton remnant can be seen. The invariant mass of the two muon system is 3.11 GeV.

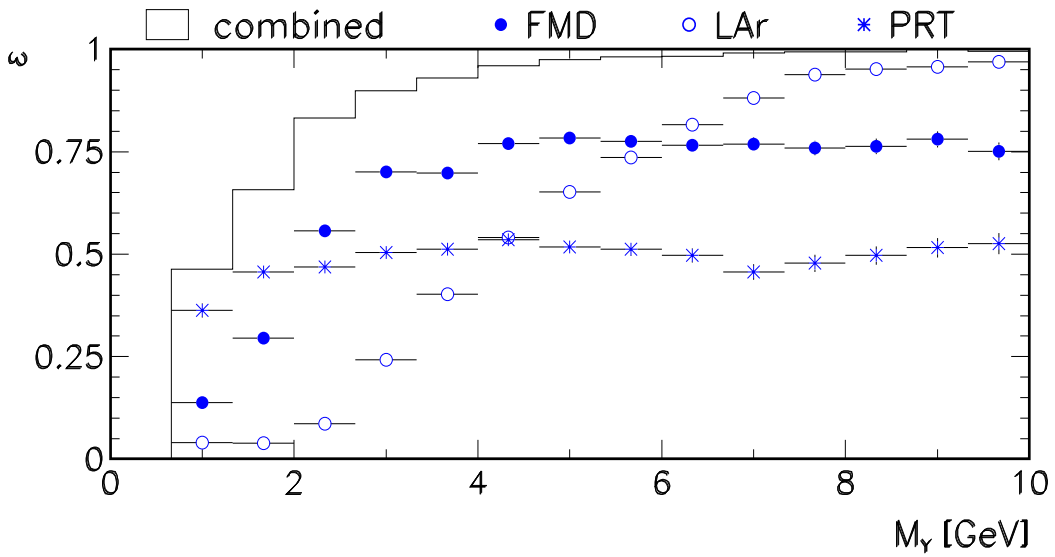

Figure 4.3: Efficiency of tagging the proton remnant as a function of the mass M_Y of the dissociated system, determined from simulated J/ψ events. Shown are the acceptances of the Forward Muon Detector, the LAr calorimeter below $\vartheta = 10^\circ$ and the Proton Remnant Tagger; "combined" refers to the logical "OR" of all three forward detectors.

and 1997 data taking periods. First of all those runs are selected in which the main detector components were operational and certain phases and high voltage conditions are required as described in section 4.1.2, which reduces the accumulated luminosity by about 20 %. In addition a correction has to be applied for a cut on the reconstructed vertex position (in the z-direction) with respect to the nominal interaction point ($|z_{vertex} - z_{nominal}| \leq 40\,\text{cm}$), which rejects events originating from satellite bunch collisions (i.e. late or early bunches) taking place outside the nominal interaction region. These events are taken into account for the online luminosity determination, which therefore has to be corrected according to the number of events rejected by this cut. Finally, the final run selection (section 4.1.2) is applied. The error on the luminosity measurement is estimated to be 1.77% (in 1996) and 1.5% (in 1997) respectively [68] and it is dominated by the knowledge of the satellite bunch corrections.

4.1.4 Kinematic Region

Events without a cluster in the SpaCal with an energy of more than 8 GeV they are considered to be photoproduction events. Due to this cut the accepted Q^2 range is restricted to below $1\,\text{GeV}^2$; this is illustrated in figure 4.4 a. In figure 4.4 b the remaining contamination of $Q^2 > 1\,\text{GeV}^2$ events can be seen ($O(0.1\,\%)$).

The restriction of the polar angle of the tracks associated with the decay muons to the central region of the detector leads to a limited acceptance in $W_{\gamma p}$. Requiring an acceptance of at least 20 %, the covered $W_{\gamma p}$ region is

$$40 \leq W_{\gamma p} \leq 150\,\text{GeV}\,, \tag{4.1}$$

		1996	1997	Σ
$\int \mathcal{L}dt$ delivered by HERA	$[\text{nb}^{-1}]$	14460	33360	47820
$\int \mathcal{L}dt$ H1 on tape	$[\text{nb}^{-1}]$	9887	28220	38107
$\int \mathcal{L}dt$ for good and medium runs	$[\text{nb}^{-1}]$	9605	24530	34135
$\int \mathcal{L}dt$ after HV and phase selection	$[\text{nb}^{-1}]$	8008	20081	28089
Satellite correction	$[\%]$	7.2 ± 1.2	6.5 ± 0.9	—
Total error on $\int \mathcal{L}dt$	$[\%]$	1.77	1.5	—
$\int \mathcal{L}dt$ for analysis	$[\text{nb}^{-1}]$	7468 ± 132	18856 ± 283	26324 ± 415
$\int \mathcal{L}dt$ after final run selection	$[\text{nb}^{-1}]$	7015 ± 124	13842 ± 208	20857 ± 332

Table 4.1: Integrated luminosity as delivered by HERA to H1 and written on tape. Rejection of poor runs (main detector components not operational) and demanding high voltage (HV) for major subdetectors reduce the luminosity further. Average satellite bunch corrections (see text) and errors on the luminosity measurement [68] are given in addition. Applying the final run selection as described in section 4.1.2 one obtains an integrated luminosity of about 21 pb^{-1}.

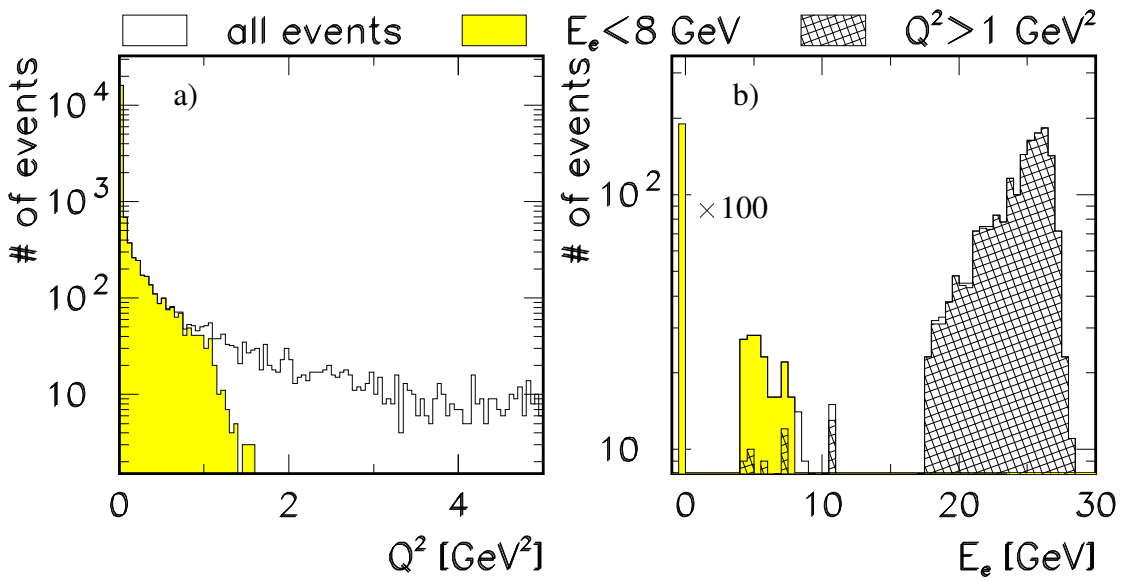

Figure 4.4: Shown is the separation between photoproduction and deep inelastic scattering (DIS) using simulated J/ψ events: a) the effect in Q^2 due to the energy cut on clusters found in SpaCal, b) the energy distribution for SpaCal clusters in DIS ($Q^2 > 1\,\text{GeV}^2$; hatched histogram) and photoproduction ($E_e < 8\,\text{GeV}$, $Q^2 \lesssim 1\,\text{GeV}^2$; shaded histogram). All events without a reconstructed cluster in SpaCal ($E_e = 0\,\text{GeV}$) are scaled down by a factor of 0.01 in b).

which is indicated in figure 4.5.

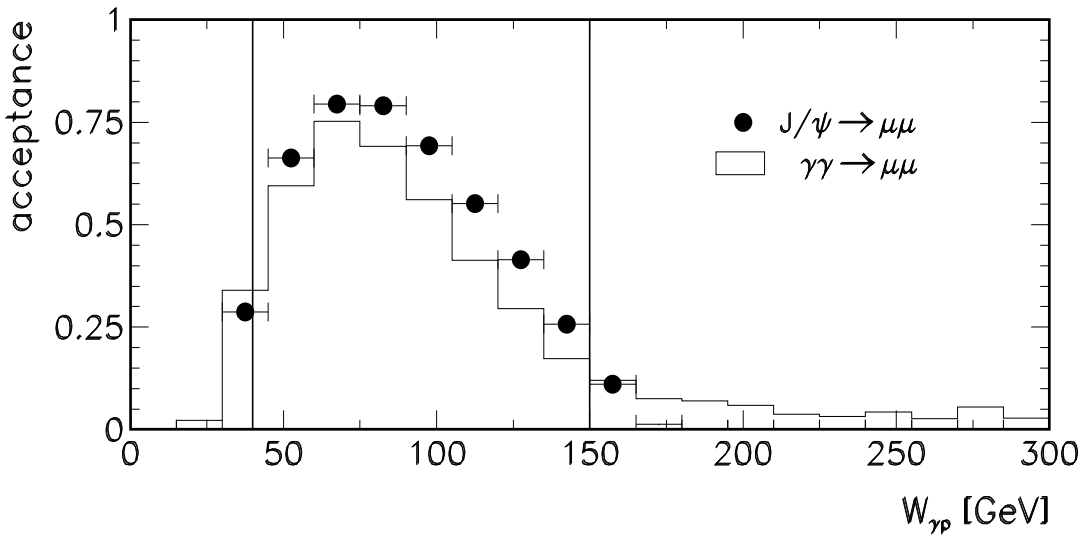

Figure 4.5: Acceptance in $W_{\gamma p}$ for a polar angular cut of $20^\circ \leq \vartheta_\mu \leq 160^\circ$. Shown are the distributions from a J/ψ Monte Carlo (full circles) and from simulated QED two–photon processes with $M_{\mu\mu} > 2\,\mathrm{GeV}$ (histogram). In addition the $W_{\gamma p}$ region used in this analysis ($40 \leq W_{\gamma p} \leq 150\,\mathrm{GeV}$) is indicated.

Concerning the range in $|t|$ a compromise has to be found between a desired long lever arm for fitting the $|t|$ distribution and limited statistics at high $|t|$. Therefore the cut

$$0 \leq |t| \leq 1.5\,\mathrm{GeV}^2 \tag{4.2}$$

has been chosen for the trajectory determination, whereas the total cross section as a function of $W_{\gamma p}$ is extracted for all $|t|$ and the corrected $|t|$ distributions cover the range in $|t|$ up to $|t| = 0.8\,\mathrm{GeV}^2$ in case of elastic J/ψ and up to $|t| = 2.5\,\mathrm{GeV}^2$ for proton dissociative J/ψ production.

The data are corrected for acceptance losses only in these regions in $W_{\gamma p}$, $|t|$ and Q^2 and are not extrapolated to the whole kinematical domain. The geometrical acceptance is shown as a function of $W_{\gamma p}$ in different bins of $|t|$ in figure 4.14 together with the other contributions to the overall data correction.

4.1.5 Background

After all trigger levels and after applying basic selection steps as described in this chapter the remaining background to the leptonic decay of heavy vector mesons stems from cosmic ray shower muons (*cosmics*), and at low invariant masses from misidentified hadrons.

Rejection of Cosmic Rays

One distinctive signature of events from ep interactions compared to cosmics is the timing (T_0) of the track measurement in the inner drift chambers with respect to the nominal bunch collisions defined by the HERA clock. While real ep events coincide with the HERA clock, cosmics pass through the detector independently of any collision frequency and are therefore uniformly distributed in time. A slight deviation from this behaviour is only due to trigger effects.

In figure 4.6 a the measured CJC T_0 is shown for ep interaction events (J/ψ candidates) overlaid with muons from cosmic showers. A cut already applied on L5 can clearly be seen[3].

A further discriminating feature of cosmic muons is their back-to-back topology[4] (see figure 4.6 b) which can be used to discriminate between diffractive heavy vector mesons and cosmics. But since vector mesons dominantly decay at rest and therefore the decay leptons fly in opposite directions in the $r\varphi$-plane[5], the separation of decay muons and cosmics has to be done with care. This is in particular true due to finite drift chamber resolution. In the J/ψ analysis a region is cut out according to $R_{\Delta\vartheta\Delta\varphi} = \sqrt{((180^\circ - \Delta\vartheta)/8^\circ)^2 + ((180^\circ - \Delta\varphi)/4^\circ)^2} < 1$ as drawn in figure 4.6 b.

figure 4.6 c shows the polar angular difference between the two decay muons and in figure 4.6 d the kinematic region populated by cosmics is illustrated. Shown is the $M_{\mu\mu} - W_{\gamma p}$ plane, in which a *cosmic band* can clearly be seen at medium $W_{\gamma p}$, in addition to the J/ψ signal that is present over the whole $W_{\gamma p}$ range in the form of a narrow band. One additional cut against cosmics is applied, a cut on the quality of the track fit ($\chi^2_{track\,fit} \leq 5$) for both vertex fitted tracks.

Misidentification of Hadrons

An additional type of background in the J/ψ analysis is due to the misidentification of hadrons as muons at low energies; one source of these events is non-resonant pion pair production. The misidentification probability decreases for higher momenta of the particles and therefore for higher invariant masses. This effect can be seen in figure 4.7. The measured invariant mass distribution is not so well described by non-resonant $\gamma\gamma \to \mu\mu$ simulated by the LPAIR generator at low masses when applying only *normal* lepton identification cuts (figure 4.7 a, category A in table 3.6), whereas the description is rather good when applying *harder* cuts (figure 4.7 b, category B in table 3.6), which reduce "non-LPAIR" background.

4.2 Selected Data Set

The final selection for diffractively produced J/ψ mesons together with the resulting event reduction is listed in table 4.2. The related sections in which the analysis steps are discussed are

[3] For 1997 data only events fulfilling $|T_0| < 50$ were classified on L5.

[4] A muon from cosmic rays which traverses the detector from top to bottom is reconstructed under the assumption of originating from the nominal interaction point thus yielding two reconstructed muons at the vertex.

[5] This is not that pronounced for ϑ due to the boost in the proton direction (figure 4.6 c).

given in addition. Following the preselection of the event classification on L5 and the selection of low multiplicity events (at most four *good* tracks[6]), requiring then one or two identified muons in the LAr calorimeter or in the instrumented iron with the algorithms presented in section 3.4, and finally calculating the invariant mass of the identified muons (in the case where both are identified) or of one identified muon and another good track and requiring this invariant mass to be larger than 2 GeV, one ends up with about 76 000 events from 1996 and 1997 together (line 5 in table 4.2).

Rejecting events with an invariant mass of more than 4 GeV and applying the diffractive event selection – no further good track with a curvature corresponding to a momentum $p > 0.8$ GeV and $p_t > 0.6$ GeV beside the decay muons – and requiring the final cuts on the decay muons, reduces the event sample to about 24 000 events (line 8 in table 4.2).

Cuts against non–ep background ($|z_{vertex}| \leq 40$ cm) and against cosmics lead to a further reduction to about 5 500 events. The run selection, trigger requirements and the kinematic cuts for photoproduction together with the separation between elastically scattered and proton dissociative J/ψ mesons result in about 1 300 forward untagged muon pairs in photoproduction in the

[6]The definition of good tracks is given in appendix A.1.

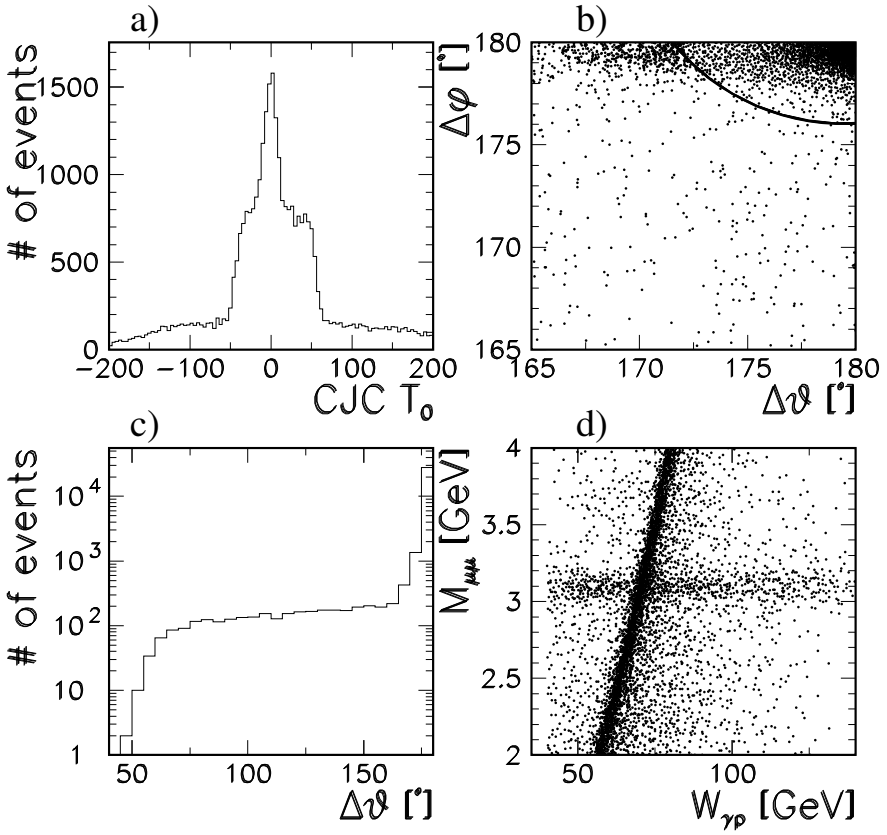

Figure 4.6: Illustration of distinctive signatures between diffractive heavy vector mesons and cosmic muons after a loose preselection (up to cut five in table 4.2): a) timing T_0 as measured in the inner drift chambers CJC, b) correlation between angular differences in ϑ and φ of the two muons, the rejected region is marked with a line, c) polar angular difference $\Delta\vartheta$ between the two muons, d) correlation between invariant mass $M_{\mu\mu}$ and hadronic centre of mass energy $W_{\gamma p}$.

	Selection Step	Section	1996	1997	$\sum$
1	All H1 events		26 360 289	30 982 674	57 342 963
2	L5 classes 17$\vee$18$\vee$24	3.3.4	3 893 595	5 719 620	9 613 215
3	Low multiplicity (≤ 4 *good* tracks)		572 963	547 920	1 120 883
4	One or two identified muons	tab. 3.6	70 044	76 381	146 425
5	$M_{ll} > 2\,\text{GeV}$		39 904	36 538	76 442
6	$M_{ll} < 4\,\text{GeV}$		15 919	18 160	34 079
7	Final muon identification (cat. A)	tab. 3.6	13 408	14 283	28 690
8	Exactly two *good* central tracks	4.1.1	11 981	11 576	23 557
9	$\lvert z_{vertex}\rvert \leq 40\,\text{cm}$	4.1.3	11 841	11 279	23 120
10	Cosmic muon rejection	4.1.5	2 038	3 465	5 503
11	Run selection	4.1.2	1 784	2 861	4 645
12	Trigger	3.3	1 014	1 392	2 406
13	Photoproduction	4.1.4	975	1 299	2 274
14	No *forward tag*	4.1.1	535	789	1 324
15	$40 \leq W_{\gamma p} \leq 150\,\text{GeV}$	4.1.4	520	764	1 284
16	$\lvert t\rvert \leq 1.5\,\text{GeV}^2$		519	741	1 260
17	$2.9 \leq M_{\mu\mu} \leq 3.3\,\text{GeV}$		346	507	853

Table 4.2: Reduction of the data volume during the J/ψ selection. Selection steps number three and number eight involve the definition of good tracks (appendix A.1), which have to be associated with oppositely charged particles with $20^\circ \leq \vartheta \leq 160^\circ$, $p > 0.8\,\text{GeV}$ and $p_t > 0.6\,\text{GeV}$. In selection step number ten the following two criteria are required: $R_{\Delta\vartheta\Delta\varphi} > 1$ and ${\chi^2}_{trackfit} \leq 5$ for both muons.

mass range of $2 \leq M_{\mu\mu} \leq 4\,\text{GeV}$, corrected for non–$ep$ background (line 14 in table 4.2).

The restriction on the kinematic range of $40 \leq W_{\gamma p} \leq 150\,\text{GeV}$ as well as $\lvert t\rvert < 1.5\,\text{GeV}^2$ together with a narrow mass window around the J/ψ resonance lead to 853 candidates.

In order to extract the cross section, the event sample is divided into several bins of $W_{\gamma p}$ or $\lvert t\rvert$ such that in each bin almost the same number of J/ψ candidates is measured. The specific number of bins which is chosen for a particular analysis depends on the balance between the statistical precision and the lever arm of the distribution for the result in question. There will be the following different sets of bin grids:

- eight bins in $W_{\gamma p}$, all $\lvert t\rvert$ for the cross section dependence on $W_{\gamma p}$
- five bins in $W_{\gamma p}$ for the corrected $\lvert t\rvert$ distributions
- six bins in $W_{\gamma p}$ each comprising five bins in $\lvert t\rvert$ in case of the measurement of the Regge trajectory.

For the resulting mass spectra and the exact bin grids see the respective result sections in chapter 5.

After applying all selection cuts, 853 events remain in the mass window ($2.9 \leq M_{\mu\mu} \leq 3.3\,\mathrm{GeV}$) around the J/ψ. This data set contains – according to simulated events – predominantly elastically scattered J/ψ mesons ($\sim 77\,\%$) and about 23 % background contributions. The background is dominated by J/ψ production with proton dissociation ($\sim 48\,\%$), indirect J/ψ production from $\psi(2S)$ decays ($\sim 9\,\%$) – i.e. events from the decay $\psi(2S) \to J/\psi + X$, muons from cosmic showers, non-resonant muon pair production and misidentified hadrons ($\sim 43\,\%$). The corresponding mass distribution containing all events from line 16 of table 4.2 is shown in figure 4.7.

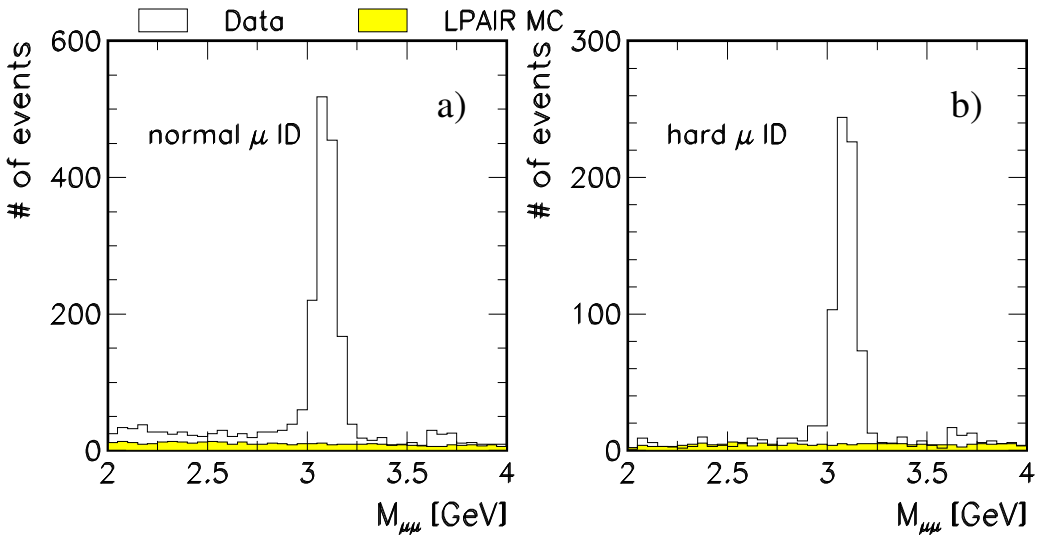

Figure 4.7: Invariant mass distribution for events passing the diffractive photoproduction selection. The open histogram represents the data while non-resonant muon pair background as simulated with the LPAIR Monte Carlo program is given in the shaded histogram: a) for normal muon identification criteria (category A in table 3.6), b) for the harder muon selection (category B).

4.3 Acceptance and Efficiencies

In order to derive cross sections, the data have to be corrected for geometrical acceptances and inefficiencies introduced by the selection cuts. Since the behaviour of the cross section as a function of $W_{\gamma p}$ and $|t|$ will be investigated, a region in these variables is chosen where relatively high acceptance is guaranteed, in order to minimize the dependence on the specific Monte Carlo model used for the correction of the data. Most of the efficiencies of the selection chain due to imperfections of the detector, such as trigger efficiency, track and vertex finding, and lepton identification efficiency, are determined from the data. If needed, the Monte Carlo simulation is corrected accordingly in order to describe the data.

The data are then corrected using the adjusted DIFFVM Monte Carlo. In figure 4.8 it is checked whether this simulation is able to describe the data. Data (full dots) and a mixture of elastic J/ψ DIFFVM plus elastic LPAIR Monte Carlo (hatched histogram), within a mass window of 200 MeV around the nominal J/ψ mass, are compared for the most important variables for this analysis: the polar angle ϑ of the decay muons (a), their azimuth φ (b), the transverse momentum p_t of the muons (c) and their angular relation in the $\vartheta\varphi$-plane ($R_{\Delta\vartheta\Delta\varphi} = \sqrt{((180^\circ - \Delta\varphi)/4^\circ)^2 + ((180^\circ - \Delta\vartheta)/8^\circ)^2}$) (d). In figure 4.8 e the distribution of the photon–proton centre of mass energy $W_{\gamma p}$ is given and finally in (f) the momentum transfer at the proton vertex $|t|$.

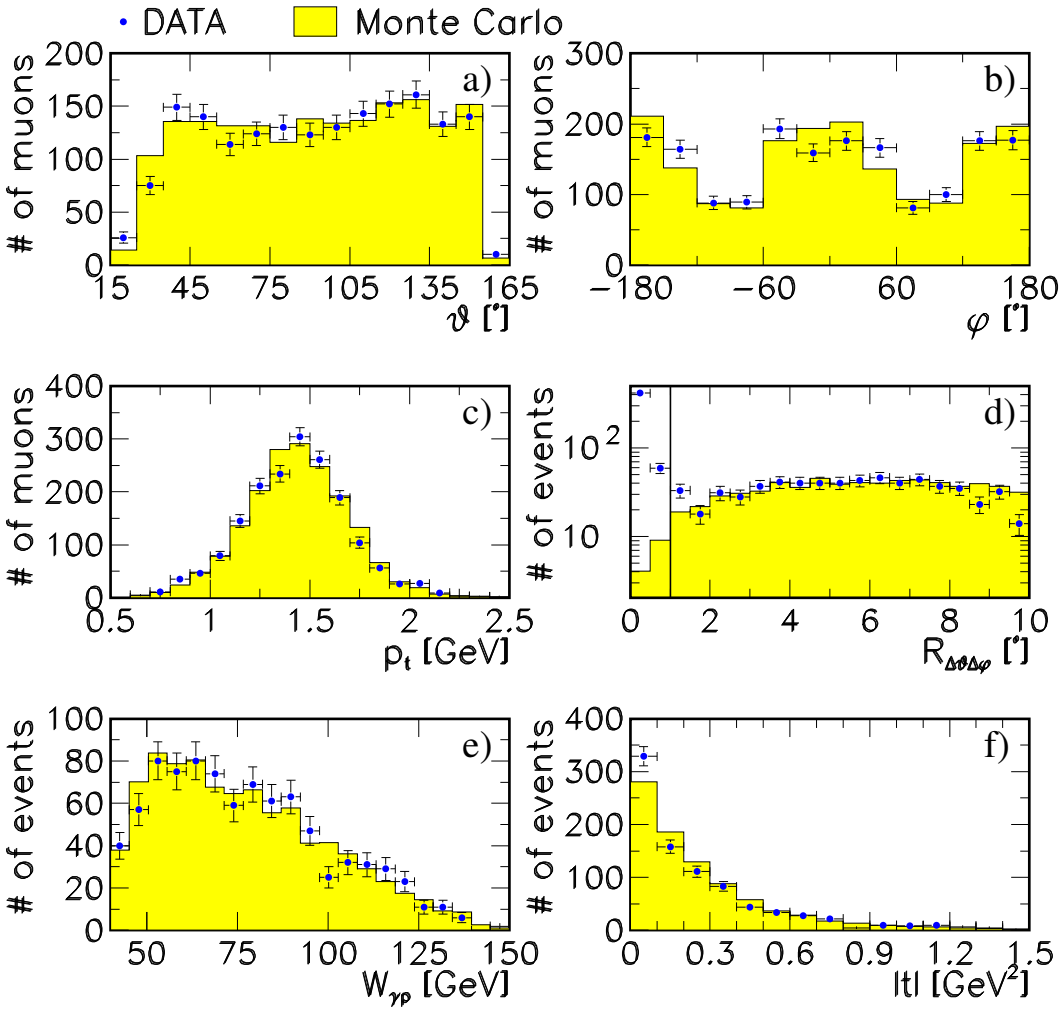

Figure 4.8: Comparison between data and Monte Carlo distributions for some important variables. a) Polar angle ϑ and b) azimuthal angle φ of the decay muons of the J/ψ and c) their transverse momentum p_t. In d) the angular relation of the two decay muons in the $\Delta\vartheta\Delta\varphi$-plane is shown: $R_{\Delta\vartheta\Delta\varphi} = \sqrt{((180^\circ - \Delta\varphi)/4^\circ)^2 + ((180^\circ - \Delta\vartheta)/8^\circ)^2}$, with $\Delta\vartheta$, $\Delta\varphi$ being the angular differences between the two muons. The line indicates the cut which is, however, not applied for this particular plot. In e) the γp centre of mass energy $W_{\gamma p}$ and in f) the momentum transfer at the proton vertex $|t|$ are displayed.

A sufficiently good description of the data by the simulation is seen in all these variables. The two minima in the φ distribution (figure b) are due to an inefficient region of the CJC in 1997. In figure d the cut applied on the angular relation between the two muons against cosmic background is indicated by a vertical line at $R_{\Delta\vartheta\Delta\varphi} = 1$. This cut rejects almost all cosmic muons in the data sample and only a small fraction of J/ψ events. The slight deviation of data and simulation at low momentum transfer $|t|$ as seen in figure 4.8 f can be explained by a slightly wrong $|t|$ dependence implemented in the Monte Carlo simulation (all events used for data correction were generated with a $|t|$-slope of $b = 4\,\mathrm{GeV}^{-2}$). Since the measured $|t|$-slope in this analysis results in higher values of b, the $|t|$-dependence in the simulation was alternatively set to $b = 5\,\mathrm{GeV}^{-2}$ (in contrast to figure f) and the resulting difference in the final cross section will later be taken into account in the systematic error.

4.3.1 Trigger Efficiency

A further important point which has to be checked before correcting the data with the help of the Monte Carlo simulation is whether the efficiencies of the trigger elements used are simulated correctly. From the description in section 3.3.1 of the trigger mix which is used for the J/ψ selection, it can be seen that the most important contributions to the overall trigger efficiency are given by the condition on the barrel part of the muon detector, the topological back-to-back condition, the efficiency of the track trigger to trigger on high p_t particles and the performance of the proportional chambers reconstructing a vertex position in low multiplicity events.

The efficiencies are determined using a sample of events which pass the preselection up to step 11 in table 4.2. These events must pass the four H1 trigger levels due to L1 triggers and L2 to L5 conditions which are independent of the investigated trigger element or the subdetector in question. In most cases SpaCal triggers are used as independent L1 triggers. In addition the efficiency for the `Topo_BR` trigger element is cross checked with events triggered by the muon system (not shown). The results of both methods are found to agree within the statistics.

In figure 4.9 data and simulation are compared with respect to the most important trigger elements for this analysis both as a function of ϑ and p_t of the muons. In the first row the efficiency for the `Topo_BR` trigger element, which requires a back-to-back topology, is presented. The second row shows the `Mu_Bar` trigger element, which triggers on the presence of two hits in one module of the barrel of the instrumented iron. The efficiency of the `DCRPh_THig` trigger element, which is sensitive to particles crossing the CJC with a momentum above 0.6 GeV, is given in the third row. And in the last row the comparison for the `zVtx_Cls` trigger element is shown, which triggers on a central primary vertex in events with few tracks.

For all these trigger elements a good overall agreement can be seen. The differences for the `Mu_Bar` trigger element are most pronounced at small p_t, while the majority of J/ψ decay muons have a transverse momentum of about 1.7 GeV. To estimate the influence of the differences in the trigger efficiencies, the simulation was corrected according to what was found in the data and the differences in the final results are found to be covered by the systematic error quoted later on.

All triggers used demand in addition veto conditions against non-ep interactions. These are chosen such that they are more than 99 % efficient for genuine ep collision events. Since the

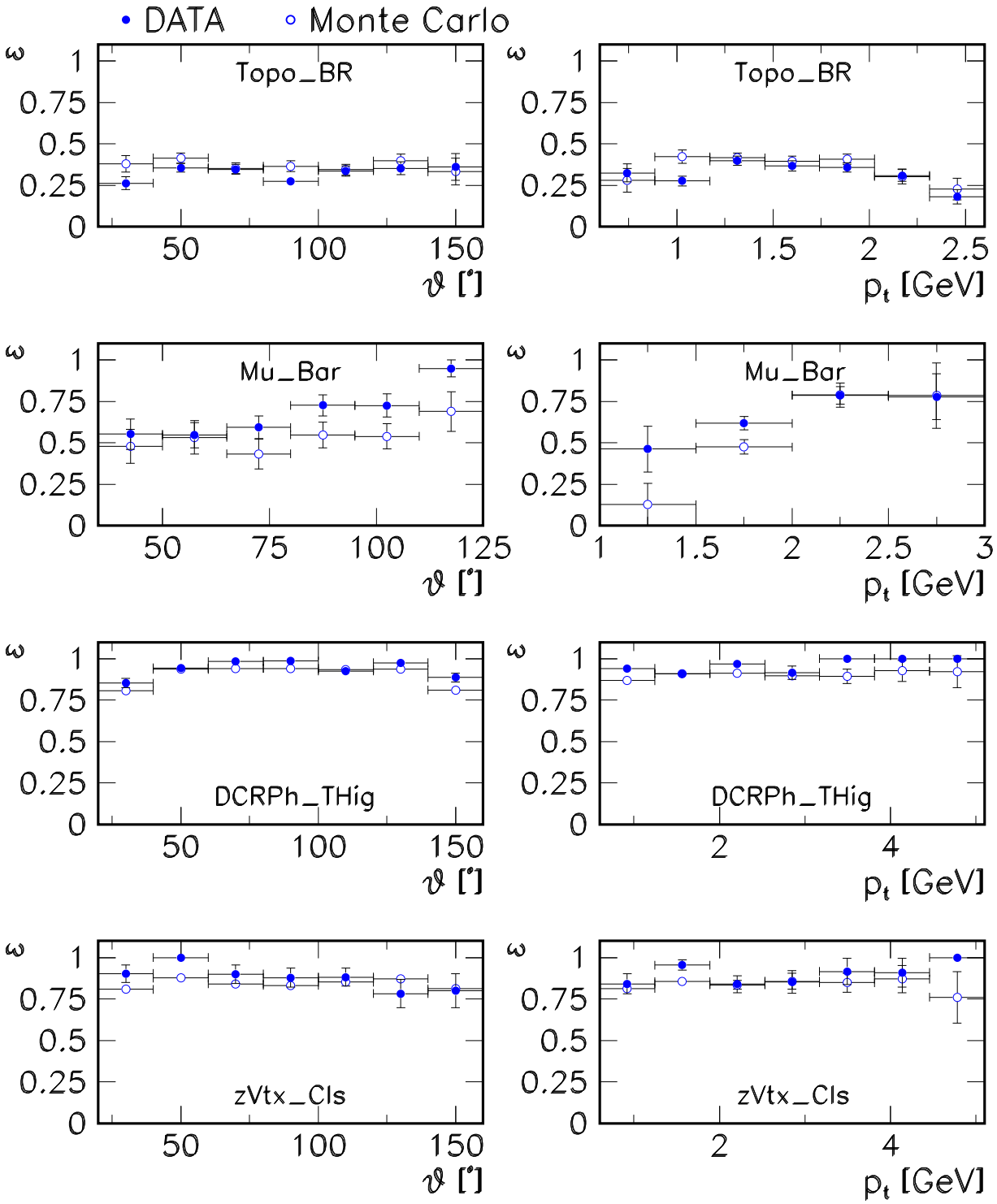

Figure 4.9: Comparison between the efficiencies of the most important trigger elements in data and in the Monte Carlo simulation.

other trigger elements described above have much lower efficiencies, the veto conditions are assumed to be 100 % efficient. The error made by this assumption is well covered in the final systematic error on the cross section.

Events triggered by the L1 trigger `s54` have to be verified by two neural net triggers on L2 (section 3.3.2). The decision of these nets is simulated in the generated events and their combined efficiency is determined to be $\sim 98\,\%$, in agreement with the value found in the data. The total trigger efficiency is shown as a function of $W_{\gamma p}$ in different bins of $|t|$ in figure 4.14 together with the other contributions to the overall data correction.

4.3.2 Vertex Finding and Track Reconstruction

The efficiencies related to the track measurement, e.g. those from hit finding, track reconstruction and vertex fit, are taken from the Monte Carlo simulation. The efficiency of the link between a reconstructed track and the vertex has been independently cross checked from the data for the 1997 data taking period [62]. From a J/ψ sample selected independently of the vertex fit, the decay leptons are used to determine the vertex link efficiency for these events. It is found to be above 99 %. The track reconstruction efficiency convoluted with the hit finding efficiency has also been determined from 1997 data. In [63], the reconstructed tracks from cosmic ray muons are used to look for correlated reconstructed tracks in the drift chambers. This method determines the efficiency for reconstructing a track in low multiplicity events to be above 99 %. This number is confirmed by using data from ep collisions instead of cosmic muons. Requiring track quality criteria close to those listed in appendix A.1 reduces this efficiency to about 97 % [63].

4.3.3 Muon Identification

The efficiency for identification of the decay muons of elastically scattered J/ψ mesons is determined in data as well as in Monte Carlo. In order to derive the efficiency for identifying a J/ψ decay muon in the LAr calorimeter those J/ψ events are selected which contain at least one well identified muon in the instrumented iron lying within the acceptance region of the calorimeter. The efficiency is then given by the fraction of the muons also identified in the LAr calorimeter (figure 4.10). From this method it is found that a ϑ dependent correction factor $(0.29 - 0.0054 \cdot \vartheta + 0.00004 \cdot \vartheta^2)$ has to be applied in the Monte Carlo simulation in order to describe the data. This is shown in figure 4.10. The efficiency found in the data is about 75% except for $\vartheta > 120^\circ$ due to the lower acceptance of the calorimeter in backward direction. The correction is of the order of 10% (up to 20% at lowest ϑ and low p_t). This is compatible with corrections applied in previous analyses such as [3] and [64].

The efficiency for muons to be identified by means of the instrumented iron (CMD) is determined with the help of events containing at least one well identified muon, the second particle having a certain minimal momentum in order to be able to reach the CMD, in addition the two particle invariant mass has to lie within the J/ψ mass window. The efficiency is then derived from the number of events where the second particle is identified in the CMD. Data and simulation agree well within the errors except in the forward direction at low polar angles ($\vartheta < 35^\circ$).

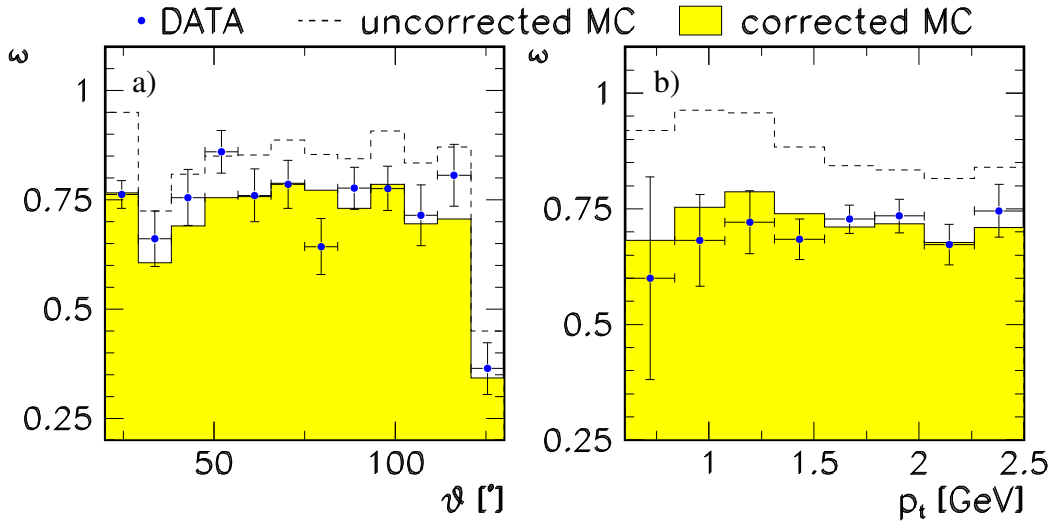

Figure 4.10: Comparison between the muon identification efficiency in the LAr calorimeter as found in data and Monte Carlo simulation for events in the J/ψ mass window selected with loose cuts. In a) the efficiency is shown as a function of the polar angle ϑ of the muons and in b) as a function of p_t. The dashed and the shaded histograms show the efficiency from the simulation before and after a ϑ-dependent correction.

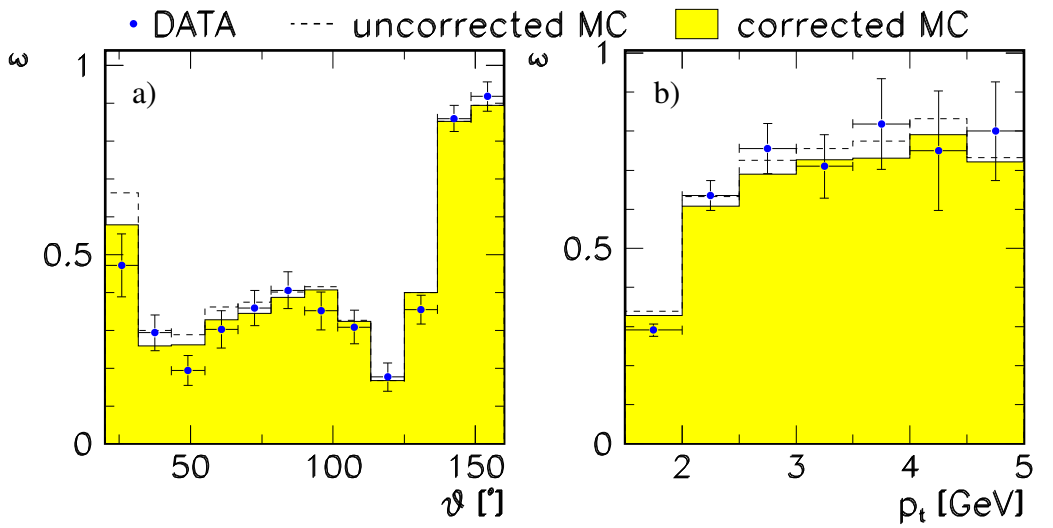

Figure 4.11: Comparison between the muon identification efficiency in the instrumented iron as found in data and Monte Carlo simulation for events in the J/ψ mass window selected with loose cuts. In a) the efficiency is shown as a function of the polar angle ϑ of the muons and in b) as a function of p_t. The dashed and the shaded histograms show the efficiency from the simulation before and after a ϑ-dependent correction.

The simulation is corrected according to this discrepancy as shown in figure 4.11 a where the simulated efficiency (dashed open histogram), the corrected Monte Carlo response (shaded histogram) and the efficiency as determined from the data can be seen (full dots). In figure 4.11 b the effect of this correction is shown as a function of p_t of the decay muons.

4.3.4 Forward Tagging

The use of the forward detectors for the separation of elastically scattered J/ψ mesons and events with proton dissociation is described in section 4.1.1. In the forward untagged J/ψ-sample, that is after requiring no activity in the forward detectors (section 4.1.1), an amount of proton dissociative background is still present ($\sim 14\%$).

Therefore not only elastic DIFFVM Monte Carlo events are used to correct the data but also a small percentage of proton dissociative events is needed. In order to correct the data for acceptance losses and detector and selection inefficiencies a mix of elastic and dissociative DIFFVM and LPAIR Monte Carlo events is used. While both LPAIR contributions, elastic and proton dissociation, are normalized to the luminosity used for the analysis, the amount as well as the mixture of elastic and proton dissociative DIFFVM Monte Carlo events has to be determined from data. The fraction of proton dissociation needed to describe the data is chosen such that the ratio of events with and without a tag in the forward detectors is similar in data and Monte Carlo (see figure 4.12 d). As illustrated in figure 4.12 a-c, the data are also described by this Monte Carlo mixture in the single distributions for the three forward detectors separately. This Monte Carlo mixture is used for all comparison plots between data and Monte Carlo in this chapter.

In figure 4.12 a the total energy measured in the LAr calorimeter below $\vartheta = 10^\circ$ is compared between this Monte Carlo mix and the data. Good agreement is found. To achieve the same for the pre-toroid hit pairs in the FMD one hit pair has to be added in the Monte Carlo due to the absence of noise hits in the simulation[7] (figure 4.12 b).

In the case of the PRT the Monte Carlo simulation has to be corrected for each scintillator which is used. These factors are calculated from the ratio between data and Monte Carlo of the number of hits in each specific counter. This is done only for those counters which are used for the analysis (1, 2, 3 and 7 in 1996 and 1, 2, 3 in 1997). In figure 4.12 c the hit distribution is shown; the entries at zero indicate that there was no hit in any of the used counters. Note that the disagreement in the seventh counter is due to the fact that it is only used and corrected for 1996 data and not for 1997. For 1996 alone the agreement is good.

The agreement between data and simulated efficiency is cross checked additionally with the following method. Signals are required in two of the three detectors and the response of the third one is compared between data and simulation. Good agreement is found for all three forward detectors.

[7] Note that this addition of one hit pair is only a correction of the distribution and has almost no influence on the number of events tagged or not tagged with the FMD, in contrast to the 3 % correction of the cross section as applied in section 5.1.1.

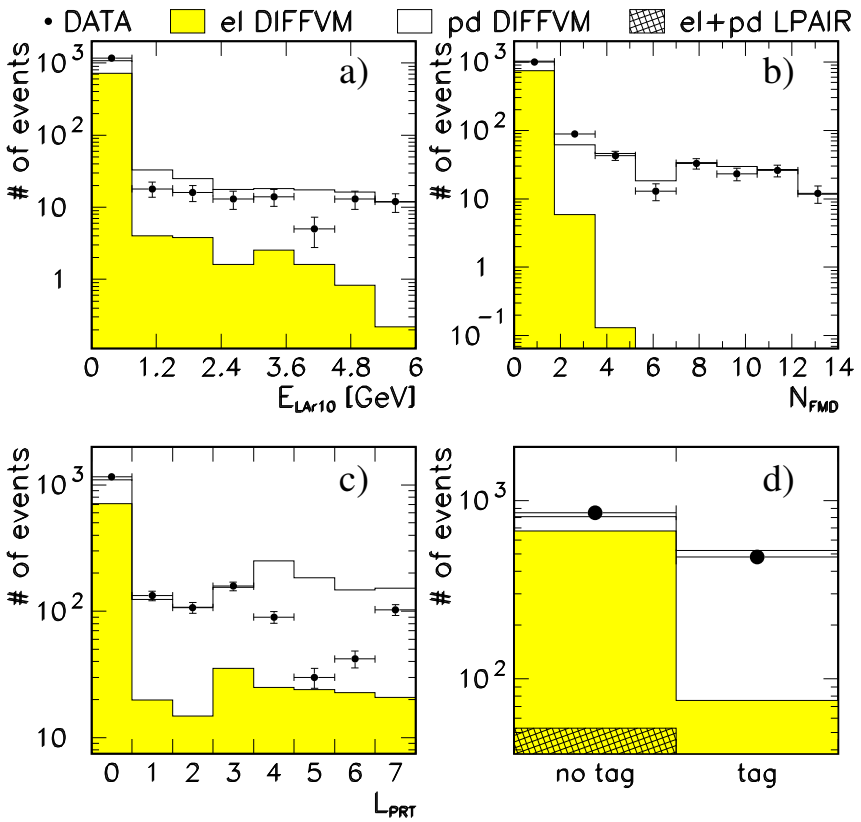

Figure 4.12: Comparison of the response of detector components used for the separation of elastic and proton dissociative data between real and simulated J/ψ events. a) Energy in the LAr calorimeter below $\vartheta = 10^{\circ}$, b) number of hit pairs in the pre-toroid layers of the Forward Muon Detector, c) hits in the Proton Remnant Tagger where "0" means "no hit" and the other numbers refer to the different scintillators of the tagger (1-7), d) decomposition of events with and without a tag using all three detectors. The content of the Monte Carlo simulation is explained in the text. The upper full histogram corresponds to the sum of all MC contributions.

In certain run ranges (190423-192499,192620-193143,193145-196582) it is not possible to use the PRT information due to timing and other problems during those periods. These run ranges correspond to 30.7% of the 1997 luminosity, so that in almost one third of 1997 luminosity the PRT is not used (in data and Monte Carlo as well) for the forward tagging of the events. This leads to a larger background contamination from proton dissociative events in the elastic event sample and to a lower efficiency in the case of the proton dissociative selection during this period.

Figure 4.13 shows the efficiency for tagging an event with at least one of the forward detectors for simulated elastic and proton dissociative J/ψ events as a function of $W_{\gamma p}$ (a) and $|t|$ (b). The probability of tagging an elastic event rises at low $W_{\gamma p}$. It also rises at higher $|t|$ due to signals in the PRT only, which is most sensitive to low proton remnant masses M_Y.

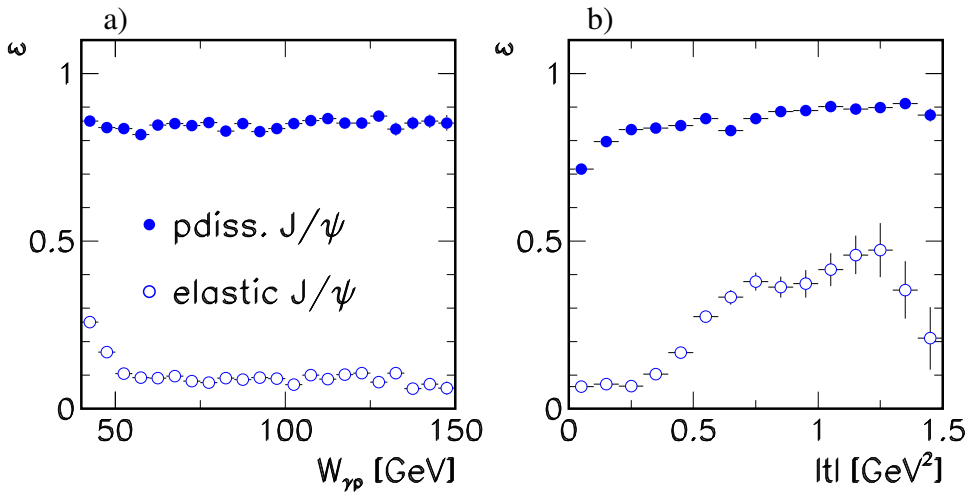

Figure 4.13: Efficiency of the forward tag in any of the detectors used (PRT, LAr, FMD) comparing simulated elastic and proton dissociative J/ψ events. Shown is the dependence on the kinematic variables $W_{\gamma p}$ (a) and $|t|$ (b).

4.3.5 Summary of Efficiencies

After comparing all essential variables and efficiencies between data and Monte Carlo and correcting for differences between them, all acceptances and efficiencies are calculated from the DIFFVM Monte Carlo. figure 4.14 shows the total efficiency together with its decomposition into geometrical acceptance, trigger efficiency and analysis efficiency, where the latter comprises all losses due to the applied selection chain (see chapter 4.1 and table 4.2). The efficiencies are taken from the elastic DIFFVM simulation; they are given as a function of $W_{\gamma p}$ in five bins of $|t|$. This two dimensional binning corresponds to the bin grid used for the measurement of the Regge trajectory in section 5.3 and is given in table 5.4.

The geometrical acceptance is due to the fact that only J/ψ events are analysed for which the decay muons are reconstructed in the central part of the detector ($20^\circ \leq \vartheta_\mu \leq 160^\circ$). It is largest for medium $W_{\gamma p}$ and almost independent of $|t|$. The trigger efficiency rises for high $W_{\gamma p}$ and drops slightly with increasing $|t|$. It is rather low since prescale factors are already taken into account. The analysis efficiency drops with $W_{\gamma p}$, it is to a good approximation flat in $|t|$. Finally, the total efficiency is of the order of 5-15% and independent of $|t|$ but slightly higher at lower $W_{\gamma p}$.

4.4 Systematic Uncertainties

In table 4.3 all different sources of systematic uncertainties are given which are introduced during the cross section extraction procedure. Several errors are due to the inaccuracy either of the efficiency determination (errors one to three, seven and eight in table 4.3) or of the knowledge of the background contribution (errors four and five). The luminosity and the branching ratio are only known to a certain accuracy (errors nine and ten). The effect of the assumed $W_{\gamma p}$ dependence in the Monte Carlo generator on the finally measured cross section behaviour is expressed

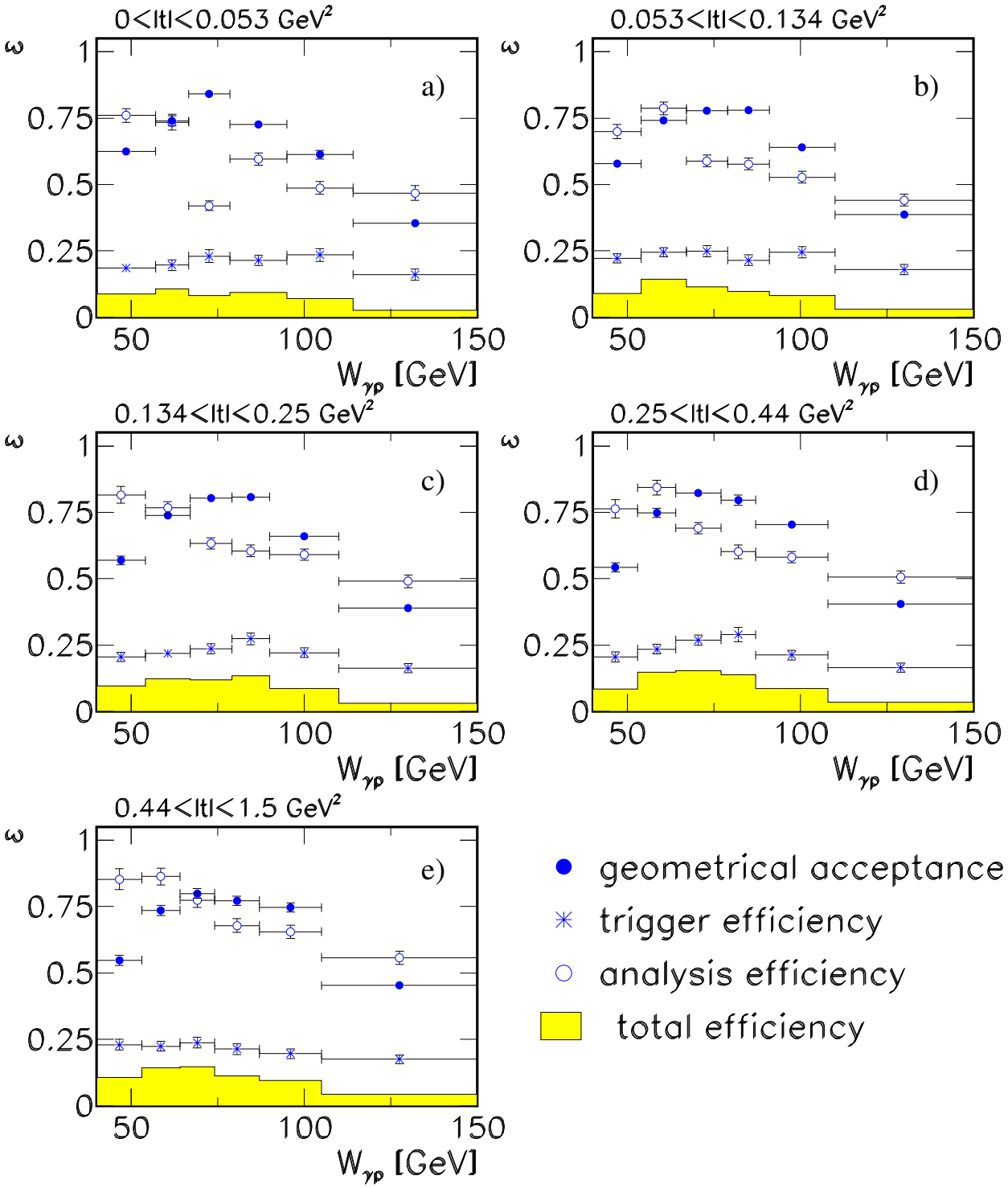

Figure 4.14: The decomposition of the total efficiency in bins of $|t|$ and $W_{\gamma p}$ into geometrical acceptance, trigger efficiency and analysis efficiency from elastic DIFFVM J/ψ Monte Carlo events.

in error number eight. The methods with which the systematic uncertainties are estimated are briefly explained in the following paragraphs.

The total systematic error of 11.8 % (on average) is dominated by the uncertainty on the lepton identification efficiency (6.5 %) and the forward tagging efficiency (5.6 % on average). Part of this error is correlated and just affects the normalization; this is estimated to be 5.2 % on average.

	Source	Amount [%]	Correlated [%]
1	Track and vertex efficiency	4	-
2	z_{vertex} distribution	1	-
3	Trigger efficiency	4	-
4	Number of signal events	2	-
5	$\psi(2S)$ background	1.2	-
6	Bin centre determination	3.3	-
7	Muon identification	6.5	3
8	Forward tagging (*)	5 / 10	2/4
9	Luminosity	1.6	1.6
10	J/ψ branching ratio	3.2	3.2
	Total systematic error (*)	11.4 / 14.3	5.1/6.1

Table 4.3: Systematic uncertainties taken into account for the cross section measurement. Items one to six are assumed to be uncorrelated between different $W_{\gamma p}$ bins, whereas the error on the luminosity determination and on the branching ratio are fully correlated in $W_{\gamma p}$. Errors seven and eight are assumed to be half uncorrelated, half correlated. For the determination of the slope of the $W_{\gamma p}$ dependence only the uncorrelated errors are taken into account. The errors marked by (*) are $W_{\gamma p}$ dependent.

Track and Vertex Efficiency The combined efficiency for hit finding in the drift chamber, track reconstruction and vertex fit amounts to 97 % according to Monte Carlo simulation. This value is verified by different analyses performed with data from 1997 (see section 4.3.2). A conservative systematic error on the track efficiency of 2 % per track is assumed (4 % error on the cross section).

z-Vertex Distribution The cut on the z-position of the event vertex (less than 40 cm from the nominal interaction point) might introduce an uncertainty due to slight differences between the data and the simulated distribution. This error is estimated by varying the z-position in the Monte Carlo by ± 1 cm. The effect on the final cross section is less than 1 %.

Trigger Efficiency The efficiencies for the different trigger elements are determined from data as described in section 4.3.1. Small differences between the data and the simulation can be seen. Correcting for these differences results in a slightly different value of the measured cross section. Since the deviation between data and Monte Carlo simulation lies within the statistical uncertainty of the efficiency determined from the data, the systematic error on the cross section is estimated from the precision with which this efficiency and therefore the deviations are known. This means the statistical error of the trigger efficiency determination is taken as the systematic error on the cross section; it amounts to up to 4 %.

Number of Signal Events The error on the number of J/ψ events (see section 5.1.1) is estimated by varying the assumed functional form for the background in the fit to the mass spectra from a polynomial to an exponential. The difference in the resulting number of J/ψ events is interpreted as a systematic error on this number (about 2 %). This error is verified by alternatively subtracting the non-resonant background with the help of simulated LPAIR Monte Carlo events and by applying a harder cut against cosmic background. Just counting the remaining events (no fit is applied) does not give a larger deviation from the number of J/ψ events extracted with the fit method than the systematic error.

$\psi(2S)$ Background The contribution from $\psi(2S)$ decay into J/ψ as well as its uncertainty is taken from the corresponding H1 measurement [69] in photoproduction convoluted with the latest branching ratios from [67].

Bin Centre Determination In order to measure the $W_{\gamma p}$ dependence of the cross section one has to determine the centres of the $W_{\gamma p}$ bins over which the cross section is integrated (see section 5.1.2). This is done with the help of the Monte Carlo simulation with which the mean of the generated events in a certain bin is evaluated. The dependence of this method on the $W_{\gamma p}$ dependence as implemented in the Monte Carlo leads to a systematic error on the bin centre determination and therefore on the slope of the $W_{\gamma p}$ dependence of the cross section. This error is estimated by varying the $W_{\gamma p}$ dependence ($\sigma \propto {W_{\gamma p}}^{\delta}$) in the Monte Carlo generator within the range $\delta = 0.9 \pm 0.4$. It is found to be 3.3 % and almost independent of $W_{\gamma p}$.

Muon Identification For the estimation of the error on the muon identification efficiency, which is one of the dominating errors for this analysis, the cross section is calculated using different cuts to constrain the events to be $J/\psi \to \mu\mu$ candidates. As described in section 3.4, besides the normal muon identification cuts as used for the analysis (category A), also very hard cuts on both decay muons on one hand (category B) and very weak cuts (category C) on the other hand, where only one muon has to be identified, are also applied. The resulting differences in the cross section are then expressed in a systematic error of 6.5 %. There is no significant dependence of this error on $W_{\gamma p}$ or $|t|$. Applying the correction to the muon identification in the simulation as described in section 4.3.3 gives a remaining difference between data and Monte Carlo. The resulting difference in the cross section lies within the quoted 6.5 %.

This total error due to the uncertainty in the muon identification is estimated to be partly correlated (3 %) and uncorrelated (3.5 %) in $W_{\gamma p}$.

Forward Tagging The error induced by the separation of the elastic and the proton dissociative data sample by means of the forward detectors as described in sections 3.2.5, 4.1.1 and 4.3.4 is estimated by the following procedure. For the separation of both samples only two out of three forward detectors are used (all three possible combinations) and the differences in the final cross section are then expressed in the systematic error. This effect is seen to be $W_{\gamma p}$ dependent; the specific values are 5 % for bins one to seven and 10 % in the eighth bin in $W_{\gamma p}$. A variation of the M_Y dependence of the proton dissociative cross section from $\sigma \propto 1/{M_Y}^{2 \cdot 1.0808}$ to $\sigma \propto 1/{M_Y}^{1 \cdot 1.0808}$ and $\sigma \propto 1/{M_Y}^{3 \cdot 1.0808}$ changes the measured elastic cross section by 2.8 %. The systematic error is assumed to be partly correlated (2 %/4 %) and uncorrelated (3 %/6 %) in $W_{\gamma p}$. The first value is valid for bins one to seven, while the second value is for the highest $W_{\gamma p}$ bin (bin eight).

Luminosity For a summary of the luminosity used and its error see table 4.1. All information is from [68].

J/ψ Branching Ratio The branching ratio and the error on it are taken from the particle data group [67]: $BR(J/\psi \to \mu\mu) = (6.01 \pm 0.19)\,\%$.

Chapter 5

Results for Diffractive J/ψ Production

After the discussion of the selection chain, Monte Carlo simulation, and experimental systematic effects in the previous chapter, this chapter will concentrate on the measurement of the production cross sections $\sigma(\gamma p \to J/\psi p)$ – "elastic" – and $\sigma(\gamma p \to J/\psi Y)$ – "p diffractive dissociation". The data, corrected for acceptance and efficiency losses, are used to study the energy dependence of the photoproduction cross section, the t dependence, the energy dependence of the t slope parameter, and finally to determine the exchanged trajectory in terms of Regge theory. The results are discussed in the light of several phenomenological models.

5.1 Cross Section Results on Elastic J/ψ Production

In this section the procedure is described by which the numbers of elastically scattered J/ψ mesons is extracted from the measured mass spectra (figure 5.1) and how non-resonant background as well as background from the decay $\psi(2S) \to J/\psi + X$ is calculated and subtracted. Then the extraction of the measured bin-integrated electron–proton cross section σ_{ep} in eight bins of $W_{\gamma p}$ is explained and afterwards the conversion into the total photon–proton cross section $\sigma_{\gamma p}$ is performed, which can be compared to different models and predictions both in magnitude and with respect to the $W_{\gamma p}$ dependence. All relevant numbers which are needed to extract the cross sections are summarized in table 5.1.

5.1.1 Correction of the Data

In the first step the number of signal events within the J/ψ mass peak has to be evaluated from the forward untagged (elastic J/ψ enriched) data sample (figure 5.1). This is done by fitting the mass spectra from $2-4\,\mathrm{GeV}$ with the sum of a Gaussian for the J/ψ resonance and a polynomial for the non-resonant background (QED two–photon processes, cosmic muons, misidentified hadrons) in each of the eight $W_{\gamma p}$ bins separately. From this fit one gets the number of diffractive J/ψ events without a tag in the forward detectors ($N_{diff}^{notag} = N_{el}^{notag} + N_{pd}^{notag}$), which comprises an elastic part (about 85 %) as well as a proton dissociative one (about 15 %) (see

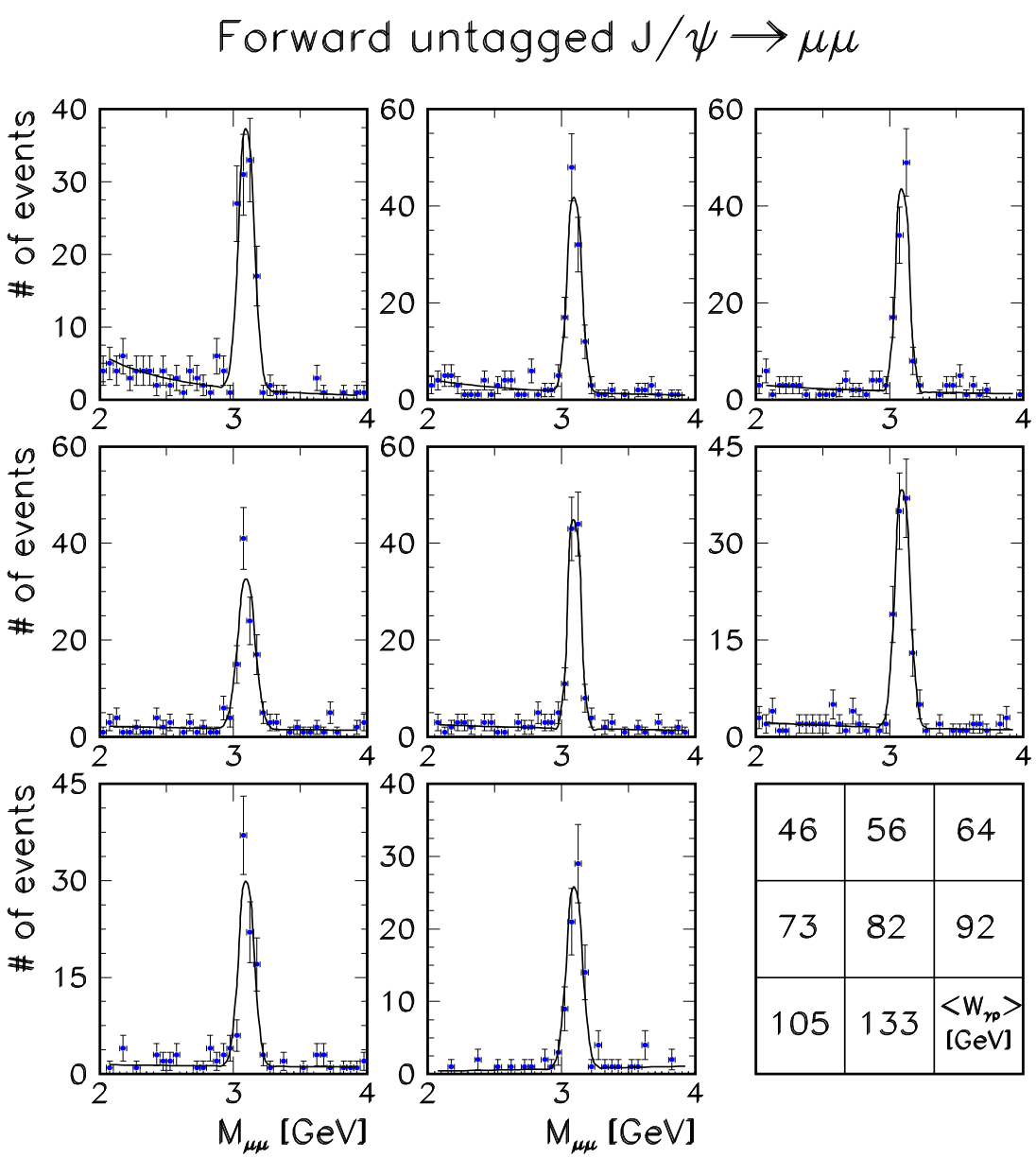

Figure 5.1: Shown are the mass spectra in eight $W_{\gamma p}$ bins for forward untagged data. In the bottom right corner the average values $\langle W_{\gamma p} \rangle$ in each bin are given.

table 5.1). The systematic error induced by this method is estimated by varying the functional form of the non-resonant background shape in the fit (see section 4.4).

As described in section 4.3.4 the elastic and the proton dissociative Monte Carlo files are mixed in such a way that the ratio of tagged and untagged events agrees well between data and simulation for all diffractive events ($N_{diff}^{notag} + N_{diff}^{tag}$) (figure 4.12). This mixture corresponds to a ratio of dissociative (N_{pd}) to elastic (N_{el}) J/ψ Monte Carlo events of $\frac{N_{pd}}{N_{el}} \approx 0.7$ (on generator level, before all cuts).

From this ratio the fraction of proton dissociative J/ψ production (f_{pd}) still present in the forward untagged sample is derived with the help of the elastic and the dissociative efficiencies

for events without a tag in the forward detectors (${\varepsilon_{el}}^{notag}$, ${\varepsilon_{pd}}^{notag}$) taken from the Monte Carlo simulation (applying all corrections as described in section 4.3):

$$f_{pd} = \frac{N_{pd}}{N_{el}} \cdot \frac{\varepsilon_{pd}^{notag}}{\varepsilon_{el}^{notag}}. \tag{5.1}$$

The resolution in $W_{\gamma p}$ is more than one order of magnitude better than the chosen bin size; therefore a bin-by-bin acceptance correction is adequate. The following definition for the efficiency in a bin of $W_{\gamma p}$ ($W_1 < W_{\gamma p} < W_2$) and for $Q^2 \leq 1\,\mathrm{GeV}^2$ is used:

$$\varepsilon_{el,pd}^{notag} = \frac{N_{el,pd}^{rec}(W_1 < W_{\gamma p}^{rec} < W_2, Q^{2,rec} \leq 1\,\mathrm{GeV}^2)}{N_{el,pd}^{gen}(W_1 < W_{\gamma p}^{gen} < W_2, Q^{2,gen} \leq 1\,\mathrm{GeV}^2)}, \tag{5.2}$$

with the labels *rec* and *gen* denoting the reconstructed and the generated variables respectively. This total efficiency contains the geometrical acceptance as well as losses due to the selection cuts and the trigger requirements.

Using equation 5.1 the corrected number $N_{J/\psi}$ of elastically scattered J/ψ mesons is given by:

$$N_{J/\psi} = N_{diff}^{notag} \cdot (1 - f_{pd}) \cdot (1 - f_{\psi(2S)}) \cdot (1 + f_{noise}^{FMD}), \tag{5.3}$$

where f_{noise}^{FMD} is a correction which takes into account the number of noise hits in the Forward Muon Detector. These noise hits are not simulated in the Monte Carlo and therefore more elastically scattered J/ψ events are rejected due to a forward tag in the data than in the simulation. This overestimation of the efficiency is determined to be about 3 % (compare e.g. [70], [71]). $f_{\psi(2S)}$ is the fraction of J/ψ events not directly produced but coming from the decay of $\psi(2S)$ mesons. The $\psi(2S)$ mesons decay predominantly via channels which include a J/ψ meson: $BR(\psi(2S) \to J/\psi + X) = (54.2 \pm 3)\,\%$ [67]. The ratio of cross sections for $\psi(2S)$ and J/ψ mesons in photoproduction has been measured by H1 [69] in a very similar $W_{\gamma p}$ regime to be $(16.0 \pm 3.8)\,\%$ [1]. Neglecting all decay channels which would not enter the J/ψ sample due to their event topology (extra charged particles beside the J/ψ), only three channels contribute significantly:

$$BR(\psi(2S) \to J/\psi\pi^0\pi^0) = (17.9 \pm 1.8)\,\%, \tag{5.4}$$
$$BR(\psi(2S) \to J/\psi\eta) = (2.7 \pm 0.4)\,\%, \tag{5.5}$$
$$BR(\psi(2S) \to J/\psi\pi^0) = (0.097 \pm 0.021)\,\%. \tag{5.6}$$

Taking into account only the neutral decays of the η meson ($BR(\eta \to \text{neutrals}) = (71.5 \pm 0.6)\,\%$) yields a total branching fraction $BR(\psi(2S) \to J/\psi + \text{neutrals}) = (19.9 \pm 2.2)\,\%$ [67]. Combining this branching ratio with the cross section ratio the result for the fraction of $\psi(2S)$ background in the J/ψ sample is $f_{\psi(2S)} = (3.2 \pm 1.2)\,\%$[2].

[1] Note that for the cross section ratio extracted in [69] the old values for the branching ratios [48] are taken. Correcting for the new values [67] changes the cross section ratio from (15.0 ± 3.5) % to the number quoted here.

[2] The decays $\psi(2S) \to \chi\gamma \to \gamma J/\psi\gamma$ are neglected. However, taking them into account would change $f_{\psi(2S)}$ to 3.8 %.

5.1.2 Extraction of the Elastic J/ψ Cross Section

In order to calculate the photoproduction cross sections $\sigma_{\gamma p}$ in bins of $W_{\gamma p}$, first of all the bin-integrated electron–proton cross sections σ_{ep} are derived, which are then converted into $\sigma_{\gamma p}$ at a certain $\langle W_{\gamma p} \rangle$ via the Weizsäcker-Williams-Approximation [7]-[10].

Calculation of the ep Cross Section

With the corrected number $N_{J/\psi}$ of elastically scattered J/ψ mesons as described in the previous section (5.1.1) the bin-integrated cross sections ($\sigma_{ep} = \int dQ^2 \int dW_{\gamma p} \frac{d^2\sigma_{ep}}{dQ^2 dW_{\gamma p}}$) in eight bins of $W_{\gamma p}$ are calculated using:

$$\sigma_{ep} = \frac{N_{J/\psi}}{\varepsilon_{el}^{notag} \cdot BR \cdot \int \mathcal{L} dt}, \tag{5.7}$$

where BR is the branching ratio for the decay $J/\psi \to \mu\mu$ [67] and $\int \mathcal{L} dt$ the integrated luminosity used for this analysis (see section 4.1.3):

$$\int \mathcal{L} dt = 20.9 \pm 0.3\,\text{pb}^{-1}, \tag{5.8}$$

$$BR(J/\psi \to \mu\mu) = (6.01 \pm 0.19)\,\%. \tag{5.9}$$

Note that corrections to the measured electron–proton cross section due to radiative effects such as initial or final state radiation are not applied since the measurement is performed in the photoproduction regime ($Q^2 \leq 1\,\text{GeV}^2$), where these radiative effects are small [72].

Calculation of the γp Cross Section

The conversion of the electron–proton cross section into the photon–proton cross section is done within the framework of the Weizsäcker-Williams-Approximation [7]-[10], where the double differential ep cross section $\frac{d^2\sigma_{ep}}{dydQ^2}$ is related to the total photoproduction cross section by

$$\frac{d^2\sigma_{ep}}{dydQ^2} = \Gamma_L \cdot \sigma_{\gamma p}^L + \Gamma_T \cdot \sigma_{\gamma p}^T \tag{5.10}$$

$$= \Gamma_T \cdot \sigma_{\gamma p}^T \cdot (1 + \varepsilon R) \tag{5.11}$$

$$= \Gamma_T \cdot \sigma_{\gamma p} \cdot \frac{1 + \varepsilon R}{1 + R} \tag{5.12}$$

$$\simeq \Gamma_T \cdot \sigma_{\gamma p}, \tag{5.13}$$

where $\sigma_{\gamma p}^L$ and $\sigma_{\gamma p}^T$ are the longitudinal and the transverse photon–proton cross sections with $R := \sigma_{\gamma p}^L / \sigma_{\gamma p}^T$. Γ_L and Γ_T are the fluxes of longitudinally and transversely polarized photons

with $\varepsilon := \Gamma_L/\Gamma_T$ being the polarization parameter, which is about 1 in the kinematic regime of this analysis. Γ_T is given by

$$\Gamma_T = \frac{\alpha_{em}}{2\pi y Q^2} \cdot (1 + (1-y)^2 - 2m_e^2 \frac{y^2}{Q^2}), \tag{5.14}$$

where α_{em} is the electro-magnetic coupling constant and m_e the electron mass. Integrating over y and Q^2 one obtains

$$\sigma_{ep} = \int_{y_{min}}^{y_{max}} dy \int_{Q^2_{min}}^{Q^2_{max}} dQ^2 \cdot \Gamma_T(y, Q^2) \cdot \sigma_{\gamma p}(y, Q^2) \qquad \text{with} \tag{5.15}$$

$$Q^2_{min} = m_e^2 \cdot \frac{y^2}{1-y}. \tag{5.16}$$

Defining the integrated flux of transversely polarized photons off the electron as

$$\mathcal{F} = \int_{y_{min}}^{y_{max}} dy \int_{Q^2_{min}}^{Q^2_{max}} dQ^2 \cdot \Gamma_T(y, Q^2), \tag{5.17}$$

a point $(\langle y \rangle, \langle Q^2 \rangle)$ – or $(\langle W_{\gamma p} \rangle, \langle Q^2 \rangle)$ – can be found for which

$$\sigma_{ep} = \mathcal{F} \cdot \sigma_{\gamma p}(\langle W_{\gamma p} \rangle, \langle Q^2 \rangle) \tag{5.18}$$

is valid.

With the help of equation 5.18 the bin-integrated electron–proton cross section is converted into a photon–proton cross section at the bin centre $(\langle W_{\gamma p} \rangle, \langle Q^2 \rangle)$. The photoproduction data of this analysis have an average $\langle Q^2 \rangle$ of $0.05\,\text{GeV}^2$. A good approximation of the bin centres $\langle W_{\gamma p} \rangle$ is obtained by taking the mean values of all generated events within the specific $W_{\gamma p}$ bins from the DIFFVM Monte Carlo simulation. The systematic error of the measurement of the $W_{\gamma p}$ dependence introduced by this method is estimated by varying the generated $W_{\gamma p}$ dependence as described in section 4.4. The resulting values of the bin centres and the γp cross sections are listed in table 5.1.

5.1.3 Elastic J/ψ Cross Section as a Function of $W_{\gamma p}$

The measured elastic photoproduction cross section for the process $\gamma p \to J/\psi p$ is shown in figure 5.2 as a function of $W_{\gamma p}$. The eight data points from this analysis are shown, together with a fit of the form $\sigma_{\gamma p} \propto W_{\gamma p}^{\delta}$ yielding a value

$$\delta = 0.96 \pm 0.16. \tag{5.19}$$

Note that only the statistical and those systematic errors which are not correlated between the $W_{\gamma p}$ bins enter the fit, because only these influence the slope of the distribution. The value obtained for δ agrees well with previous measurements in photoproduction ($\delta = 0.80 \pm 0.10$

	$40 < W_{\gamma p} < 52\,\text{GeV}$	$52 < W_{\gamma p} < 60\,\text{GeV}$	$60 < W_{\gamma p} < 67.8\,\text{GeV}$
N_{diff}^{notag}	103.7 ± 10.5	107.1 ± 10.8	102.4 ± 10.6
f_{pd} [%]	14.5 ± 1.4	13.9 ± 1.5	12.0 ± 1.4
ε_{el}^{notag} [%]	9.1 ± 0.3	9.8 ± 0.5	10.1 ± 0.6
$N_{J/\psi}$	88.4 ± 10.5	91.9 ± 10.8	89.8 ± 10.6
$\mathcal{F}$	0.025846	0.013410	0.011038
$\langle W_{\gamma p} \rangle$ [GeV]	45.92	55.94	63.85
$\sigma_{\gamma p}$ [nb]	$29.8 \pm 3.7 \pm 3.4$	$41.7 \pm 5.2 \pm 4.8$	$49.5 \pm 6.6 \pm 5.6$
	$67.8 < W_{\gamma p} < 77\,\text{GeV}$	$77 < W_{\gamma p} < 86\,\text{GeV}$	$86 < W_{\gamma p} < 97\,\text{GeV}$
N_{diff}^{notag}	99.5 ± 10.9	101.6 ± 10.8	101.6 ± 10.6
f_{pd} [%]	11.6 ± 1.3	16.2 ± 1.8	13.9 ± 1.5
ε_{el}^{notag} [%]	8.7 ± 0.5	9.0 ± 0.5	7.9 ± 0.4
$N_{J/\psi}$	87.7 ± 10.8	84.9 ± 10.8	87.2 ± 10.6
$\mathcal{F}$	0.011057	0.009223	0.009606
$\langle W_{\gamma p} \rangle$ [GeV]	72.35	81.41	91.48
$\sigma_{\gamma p}$ [nb]	$51.8 \pm 6.9 \pm 5.9$	$62.4 \pm 8.5 \pm 7.1$	$67.6 \pm 8.8 \pm 7.7$
	$97 < W_{\gamma p} < 113\,\text{GeV}$	$113 < W_{\gamma p} < 150\,\text{GeV}$	$40 < W_{\gamma p} < 150\,\text{GeV}$
N_{diff}^{notag}	82.0 ± 8.9	72.9 ± 8.9	768 ± 28
f_{pd} [%]	14.1 ± 1.6	15.8 ± 1.9	13.2 ± 0.5
ε_{el}^{notag} [%]	4.6 ± 0.3	2.0 ± 0.1	5.4 ± 0.1
$N_{J/\psi}$	70.2 ± 9.8	61.2 ± 8.5	665 ± 28
$\mathcal{F}$	0.011474	0.018892	0.110487
$\langle W_{\gamma p} \rangle$ [GeV]	104.9	130.8	89.4
$\sigma_{\gamma p}$ [nb]	$64.6 \pm 9.6 \pm 7.4$	$89.0 \pm 13.2 \pm 12.7$	$55.9 \pm 2.5 \pm 6.7$

Table 5.1: Summary of the elastic J/ψ cross section in eight bins of $W_{\gamma p}$. The errors on f_{pd} and ε_{el}^{notag} represent the statistical error of the Monte Carlo simulation, whereas the error on N_{diff}^{notag} is the statistical error from the fit to the data. The error on $N_{J/\psi}$ comprises both these statistical uncertainties. The first error on the cross section is the statistical and the second is the systematic uncertainty. The last column shows the photoproduction cross section for the entire $W_{\gamma p}$ range from 40 to 150 GeV.

from ZEUS [73] and preliminary H1 data [74]) as well as at higher Q^2 ($\delta = 0.84 \pm 0.20$ at $Q^2 = 3.5\,\mathrm{GeV}^2$ and $\delta = 1.3 \pm 0.4$ at $Q^2 = 10.1\,\mathrm{GeV}^2$ [71]).

The cross sections extracted in this analysis are compared with previous HERA data in the same $W_{\gamma p}$ regime [15, 73] as well as at higher $W_{\gamma p}$ [75] and with results from fixed target experiments [76, 77] at much lower $W_{\gamma p}$ values (figure 5.3). A fit to all available HERA data in the range $30 \leq W_{\gamma p} \leq 285\,\mathrm{GeV}$ yields $\delta = 0.81 \pm 0.08$ (see figure 5.3).

Low energy results are only shown for those experiments which use free proton targets and distinguish between elastically scattered J/ψ mesons and those with proton dissociation (compare also the discussion in [78]). A fit of the form $\sigma_{\gamma p} \propto W_{\gamma p}^{\delta}$ to all these data yields

$$\delta = 0.83 \pm 0.05\,, \tag{5.20}$$

which is in good agreement with the result for this analysis alone (equation 5.19).

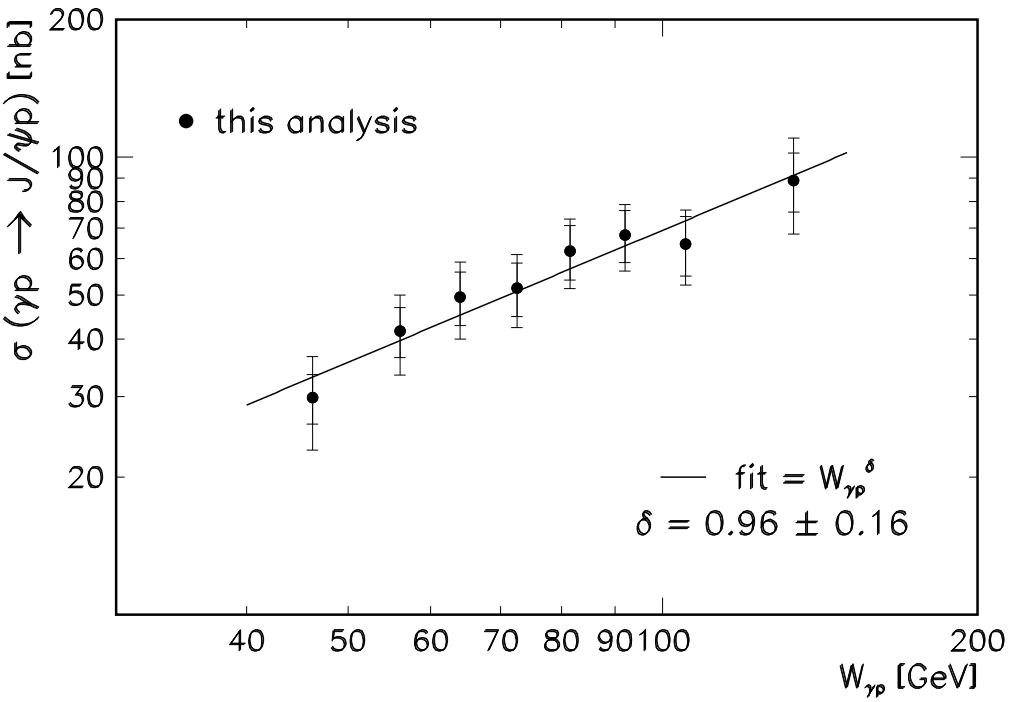

Figure 5.2: The total photoproduction cross section $\sigma(\gamma p \to J/\psi p)$ versus $W_{\gamma p}$ resulting from the analysis presented here. A fit $\propto W_{\gamma p}^{\delta}$ to the data is performed yielding $\delta = 0.96 \pm 0.16$. The inner error bars show the statistical uncertainty, whereas the outer bars give the systematic and the statistical errors added in quadrature.

Discussion of $\sigma_{\gamma p}$ in the Light of the Two-Pomeron Model

As stated previously, the measured slope of the $W_{\gamma p}$ dependence of $\sigma_{\gamma p}$ rules out the weak rise with $W_{\gamma p}$ predicted by *soft* pomeron models ($\sigma_{\gamma p} \propto W_{\gamma p}^{0.22-0.32}$; see section 2.2.1). In a new model by Donnachie and Landshoff – the so-called two-pomeron model [19] – a second (*hard*)

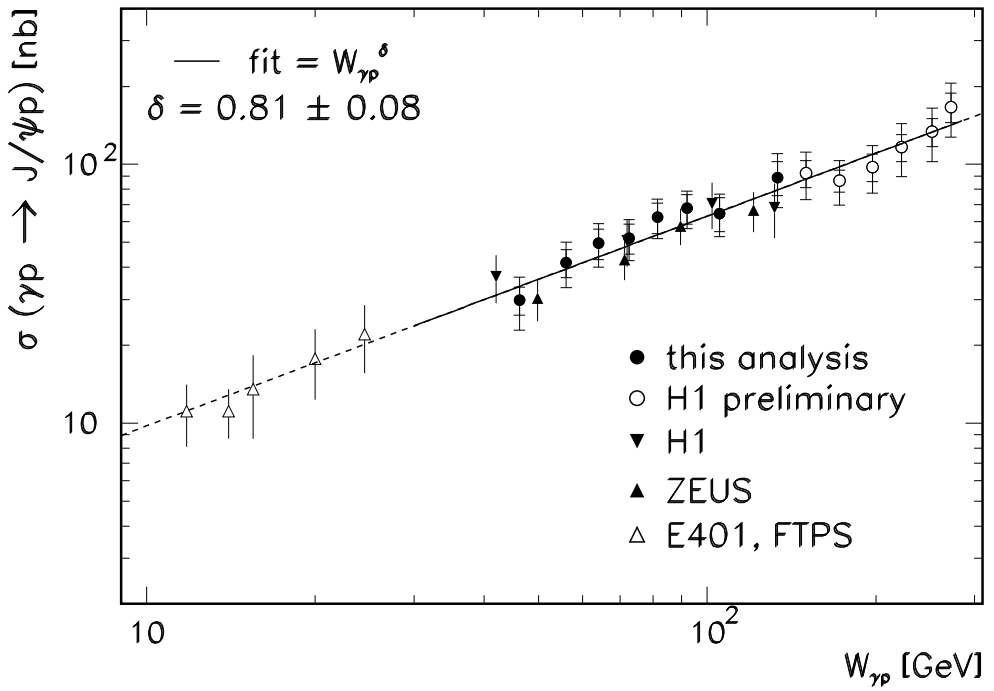

Figure 5.3: The total photoproduction cross section $\sigma(\gamma p \rightarrow J/\psi p)$ versus $W_{\gamma p}$ for this analysis, previous HERA results and low energy measurements. A fit $\propto W_{\gamma p}^{\delta}$ to the HERA data is performed yielding $\delta = 0.81 \pm 0.08$. The inner error bars show the statistical uncertainty, whereas the outer bars give the systematic and the statistical errors added in quadrature.

pomeron with an intercept of about 1.4 is derived from the analysis of F_2 data at low x. A fit to all HERA J/ψ photoproduction data according to this model is shown in figure 5.4. The relative contributions of both pomerons are used as free parameters, while the intercepts and slopes of the trajectories and therefore the shape of the cross sections remain unchanged.

The dashed lines show the contributions by the soft and the hard pomeron and their mixing. The fit to the HERA data alone reproduces the shape of the $W_{\gamma p}$ dependence rather nicely, but deviates significantly from the fixed target points both in shape and in magnitude. In figure 5.5 the fit range is extended to the low energy data. The same two-pomeron fit performed over the whole accessible $W_{\gamma p}$ domain (10-300 GeV) is everywhere in reasonable agreement with the data but especially for the HERA data systematic deviations in magnitude from the model can be seen.

Discussion of $\sigma_{\gamma p}$ in the Light of Perturbative QCD

In contrast to Regge-inspired models such as the soft pomeron model by Donnachie and Landshoff or their two-pomeron model, which do not predict the absolute value of the cross section but only its dependence on $W_{\gamma p}$, calculations in perturbative QCD predict in addition to a steep rise with energy also the absolute value of the cross section for J/ψ production. This absolute

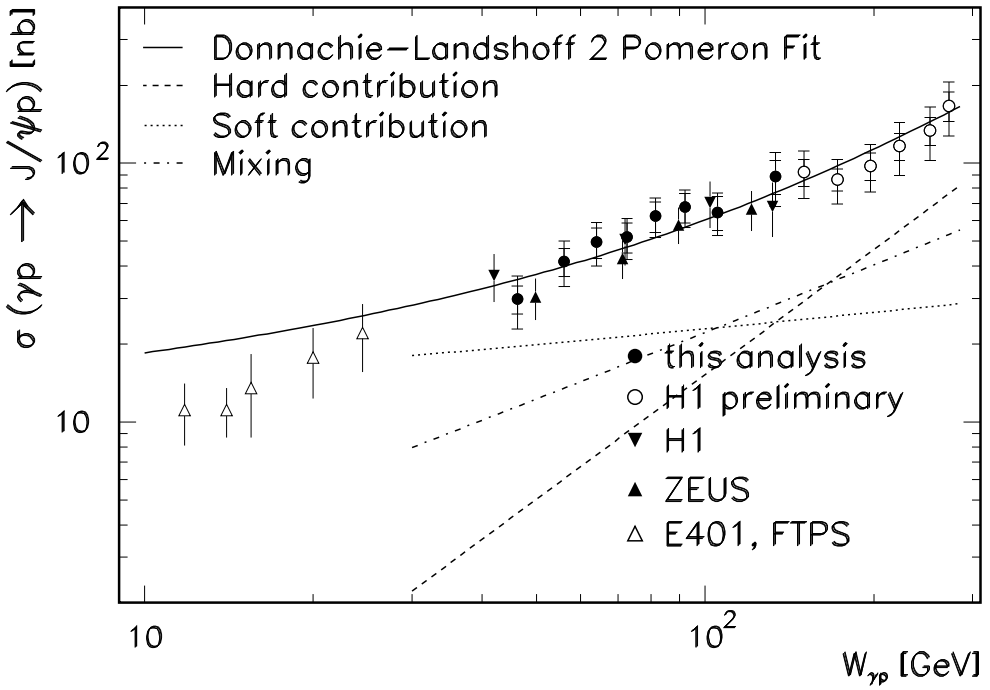

Figure 5.4: The total photon–proton cross section $\sigma(\gamma p \to J/\psi p)$ versus $W_{\gamma p}$ for this analysis, previous HERA results and low energy measurements. A fit according to the two-pomeron model by Donnachie and Landshoff [19] is performed to the HERA data only (full line). The dashed curves represent the *soft* and the *hard* pomeron contribution as well as their mixing.

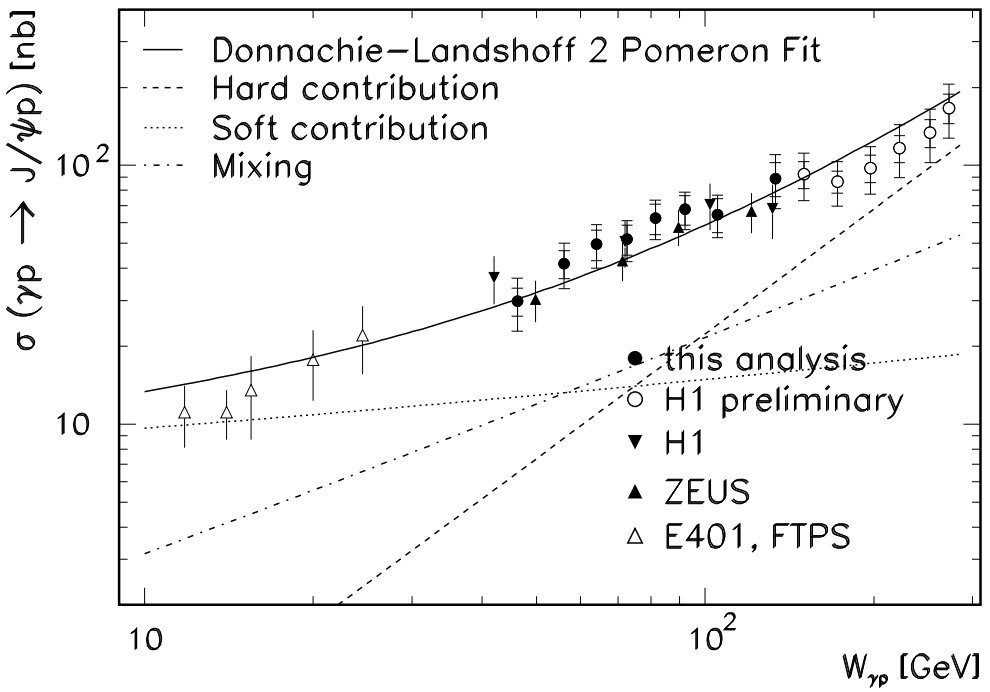

Figure 5.5: The same as figure 5.4 but the fit performed to all HERA and low energy data.

value is strongly dependent on the choice of the charm quark mass m_c and the gluon density in the proton. The latter also has a strong influence on the shape of the prediction. In this section the HERA data are compared to calculations by Frankfurt, Koepf and Strikman (FKS) (see [37]–[39] and section 2.3).

The predictions shown in figure 5.6 are calculated for three different gluon densities of the proton (GRV [79], MRSR2 [80], CTEQ4M [81]). Since the absolute normalization is strongly dependent on the chosen charm quark mass (section 2.3), each curve is adjusted with a different value for the charm quark mass: $m_c = 1.5\,\text{GeV}$ (GRV), $m_c = 1.38\,\text{GeV}$ (MRSR2), $m_c = 1.43\,\text{GeV}$ (CTEQ4M). Changing m_c from 1.5 GeV to 1.4 GeV reduces the cross section at $W_{\gamma p} = 200\,\text{GeV}$ by about 40 %.

While it is not possible to discriminate between the MRSR2 and the CTEQ4M gluon densities with help of the data at the moment, it can clearly be seen that – even with the current precision – the GRV proton parameterisation does not fit the shape of the data. Note that the calculation is not expected to work at low values of $W_{\gamma p}$, i.e. in the fixed target regime.

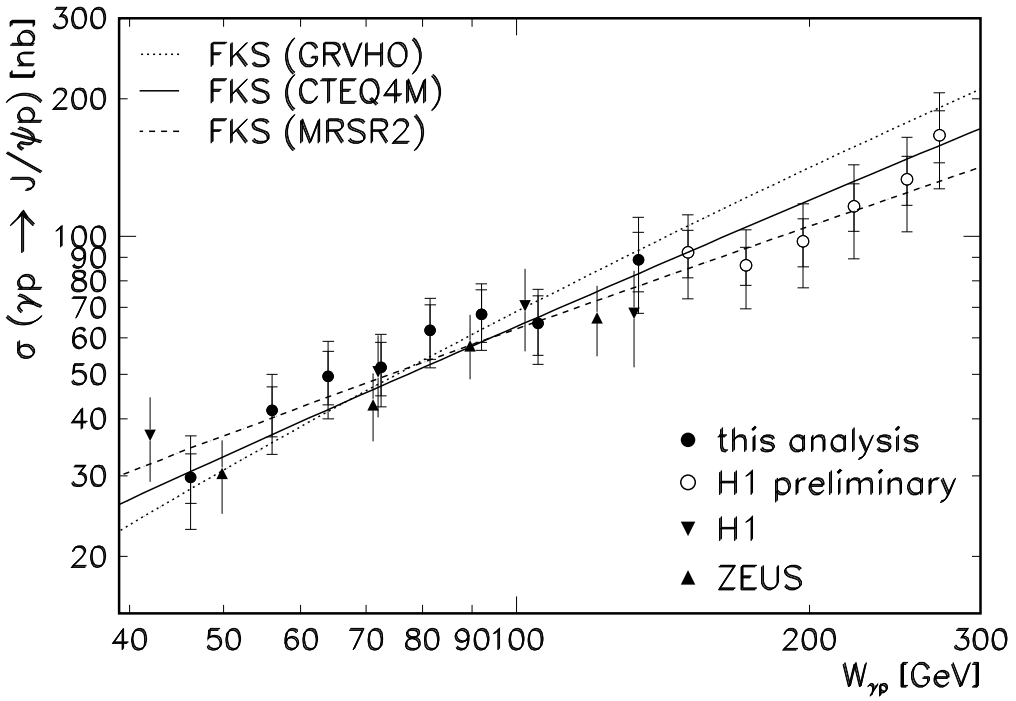

Figure 5.6: The total photon–proton cross section $\sigma(\gamma p \to J/\psi p)$ versus $W_{\gamma p}$ for this analysis and previous HERA results. The data are shown together with predictions by Frankfurt, Koepf and Strikman [39] for different proton parameterisations. Note that the absolute normalisation is adjusted by the choice of the charm quark mass.

5.2 The t Distribution

In order to study the dependence on t, the momentum transfer at the proton vertex, the forward untagged data sample containing predominantly elastically scattered J/ψ mesons is divided into five bins in $W_{\gamma p}$, and the t distributions are extracted in each bin. The correction for background and all t and $W_{\gamma p}$ dependent effects such as geometrical acceptance, trigger efficiency and analysis efficiency is performed as described in section 4.3. A fit is performed to the corrected t distributions with a function $e^{-b|t|}$ and the slope parameter b is measured in five bins of $W_{\gamma p}$ as well as for the entire $W_{\gamma p}$ range. For comparison the corrected t distribution for proton dissociative events is extracted for the entire $W_{\gamma p}$ range and the b parameter is determined as well.

5.2.1 Slope Parameter b for Elastic Scattering of J/ψ Mesons

The procedure used to extract the slope parameter from the measured t distributions will be discussed in this section. It is explained for the elastic analysis but holds also for the proton dissociative data. In the following, the slope parameter extracted from elastic J/ψ events is called *elastic slope parameter* and that extracted from proton dissociative events is called *proton dissociative slope parameter*.

Correction of the Data

In order to extract the slope parameter b a tighter selection (category B in table 3.6) with respect to the lepton identification is performed compared to the cross section analysis in section 5.1: both muons have to be identified and only CMD muons and *good* calorimeter muons are allowed. This is done because the slope of the steep t distribution is very sensitive to any background contamination. In contrast to the cross section measurement the number of J/ψ events in each t bin is not determined by a fit to the mass spectrum, but the measured t distribution is directly corrected for background by means of simulated LPAIR and DIFFVM events, assuming background only from $\gamma\gamma \to \mu\mu$ and proton diffractive dissociation. Due to the lack of knowledge about the t dependence of background from misidentified hadrons a tight lepton identification is required. In addition, a narrow mass window ($2.9 < M_{\mu\mu} < 3.3\,\text{GeV}$) around the J/ψ resonance is chosen in order to suppress non-resonant background as much as possible without losing too much of the signal.

All data are divided into five $W_{\gamma p}$ bins (see table 5.3). Elastic slope parameters are extracted in these five bins as well as for the entire $W_{\gamma p}$ range (given in the last column in table 5.3). The momentum transfer t at the proton vertex can be approximated by $p^2_{t,J/\psi}$:

$$|t| = -t_{min} + p^2_{t,J/\psi} + Q^2\,, \tag{5.21}$$

and for low Q^2:

$$|t| \simeq p^2_{t,J/\psi}\,. \tag{5.22}$$

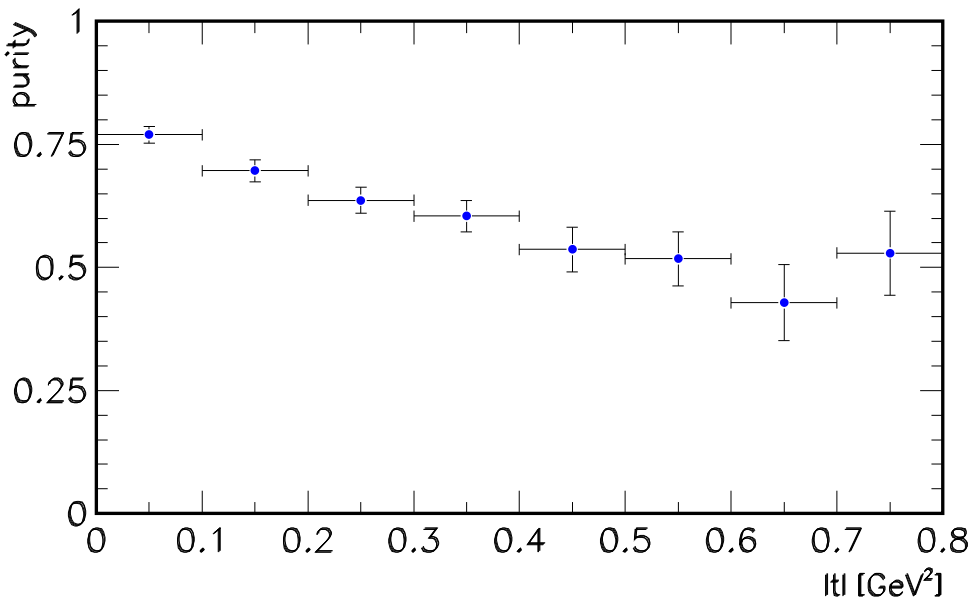

Figure 5.7: Shown is the purity of t bins within the kinematic region of the analysis. The purity is always better than 40 %.

Note that the minimum momentum transfer t_{min} needed for the reaction is very small for elastic scattering and can be neglected (see section 2.1). Due to the chosen kinematical region in this analysis the Q^2 of the events is restricted to values smaller than 1 GeV^2 with a mean value of $\langle Q^2 \rangle = 0.05\,\text{GeV}^2$. Nevertheless, the exact Q^2 is not known and therefore a small deviation between true and reconstructed t is introduced. The measurement is performed in eight equally sized bins. In figure 5.7 the purity ($N_{true,rec}/N_{rec}$) of the data in the chosen t bins is shown to be larger than 40 % everywhere. The resolution in t is found to be in the worst case, at low $|t|$, about 20 % ($\pm 0.02\,\text{GeV}^2$ at $|t| = 0.1\,\text{GeV}^2$), whereas the chosen bin width, $0.1\,\text{GeV}^2$, is much larger.

In figure 5.8 the raw t distribution resulting from the selection is shown together with the background subtracted one (non-resonant and proton dissociation background). Since the lepton identification criteria are hard the non-resonant background is assumed to stem only from QED two–photon processes (compare figure 4.7) and is subtracted in each t bin as estimated from the LPAIR simulation. The influence of muon events from cosmic background on the slope parameter is estimated to be small (about 1 %) by varying the cosmic cuts. The remaining background from proton dissociation after requiring no forward tag is determined and subtracted for each t bin separately from the simulation. The decomposition of the overall correction applied into geometrical acceptance, trigger and selection efficiency as a function of t and $W_{\gamma p}$ has already been shown and discussed in section 4.3.

Systematic Uncertainties on b

The systematic error on the b measurement is estimated for different possible sources summarized in table 5.2. The determination of the error is performed by fitting the corrected t

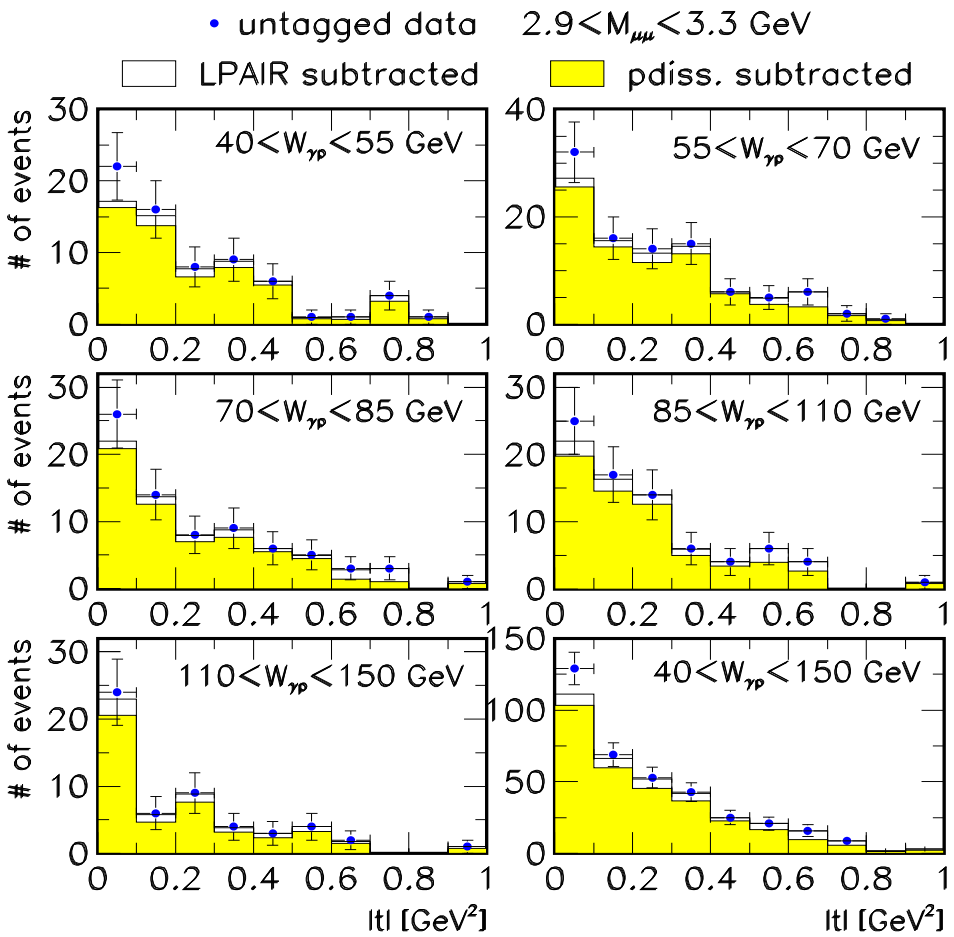

Figure 5.8: The uncorrected t distributions in bins of $W_{\gamma p}$ and in the bottom right corner for the entire $W_{\gamma p}$ range. The points represent the raw t distributions as measured with the forward untagged data sample within a narrow mass window around the J/ψ resonance ($2.9 < M_{\mu\mu} < 3.3\,\text{GeV}$). The histograms show the same data after a successive background subtraction (open histogram: LPAIR subtracted, shaded histogram: LPAIR and proton dissociation subtracted).

distribution for the entire $W_{\gamma p}$ range taking into account only the statistical uncertainty of the data points and then varying the variable in question. The deviation of the resulting b value from the original one is converted into a systematic error.

The first three errors listed in table 5.2 are due to uncertainties on the background contamination. As mentioned before, the lepton identification for this measurement is chosen to be rather strict in order to suppress as many of the misidentified hadrons as possible. Applying weaker cuts on the muons results in a larger background contribution from non-resonant pion pairs. This background contamination leads to deviations in b (about 8 %). The influence of the proton dissociative background on the elastic slope parameter extracted here is estimated by choosing different combinations of forward detectors as already described for the cross section calculation (section 4.4). It is found to give a systematic error of 4.7 %. The influence of a possible contamination of cosmic rays is small (~ 1 %), since a much stricter cut on the *back-*

Source	Amount [%]
lepton identification	8
forward tagging	4.7
cosmic rejection	1
modelled W dependence	4.5
modelled t dependence	8.7
modelled α'	3.7
Total systematic error	14

Table 5.2: Summary of systematic uncertainties on b. No significant $W_{\gamma p}$ dependence is found.

to-back topology of the events (varying the back-to-back cut from $R_{\Delta\vartheta\Delta\varphi} > 1$ to $R_{\Delta\vartheta\Delta\varphi} > 2.5$, compare figure 4.8) yields almost the same b.

The last three errors mentioned in table 5.2 concern the model dependence assumed in the Monte Carlo simulation for data correction. Varying the $W_{\gamma p}$ dependence between $W_{\gamma p}^{0.5}$ and $W_{\gamma p}^{1.3}$ changes the extracted value for b by 4.5 %. Changing the generated t dependence like $b = 4 \pm 0.5\,\mathrm{GeV}^{-2}$ results in the largest contribution to the total systematic uncertainty of 8.7 % due to differences in forward tagging efficiencies and therefore a different estimation of the background fraction from proton dissociation. Assuming the presence of shrinkage – this is a $W_{\gamma p}$ dependent slope parameter of the form $b = b_0 + 4\alpha' \ln(W_{\gamma p}/90\,\mathrm{GeV})$ – according to *soft* pomeron models (section 2.2.1) by inserting $\alpha' = 0.25\,\mathrm{GeV}^{-2}$ changes the measured b by about 3.7 %.

All these investigations were also performed in each of the five $W_{\gamma p}$ bins separately but no significant $W_{\gamma p}$ dependence could be found. The different sources of systematic errors add up to a total systematic uncertainty of 14 %, which is about twice as large as the statistical precision of the data. Thus the measurement of the elastic slope parameter b is – especially for the entire $W_{\gamma p}$ range – dominated by systematic uncertainties.

Results on the Elastic Slope Parameter

The background subtracted and thus pure elastic t distributions shown in figure 5.8 are corrected for all t and $W_{\gamma p}$ dependent effects[3] and normalized to the initial number of events: $dN/dt = dN'/dt \cdot N_0/N_0'$, where N_0 is the initial, measured number of events with $|t| < 0.8\,\mathrm{GeV}^2$ and N_0' is the corrected number of events in the same $|t|$ range. The resulting corrected numbers of events $dN/d|t|$ are displayed in figure 5.9 for the entire $W_{\gamma p}$ range and in figure 5.10 for the five $W_{\gamma p}$ bins separately. The entries in each bin are given at the bin centre, which is determined in a similar way as the bin centres in $W_{\gamma p}$, namely, the mean value of the generated events, simulated with the DIFFVM Monte Carlo, is chosen.

[3] Note that no correction is performed for $\psi(2S)$ background or noise in the FMD (as discussed on the cross section) since the t or $W_{\gamma p}$ dependences have not been measured up to now.

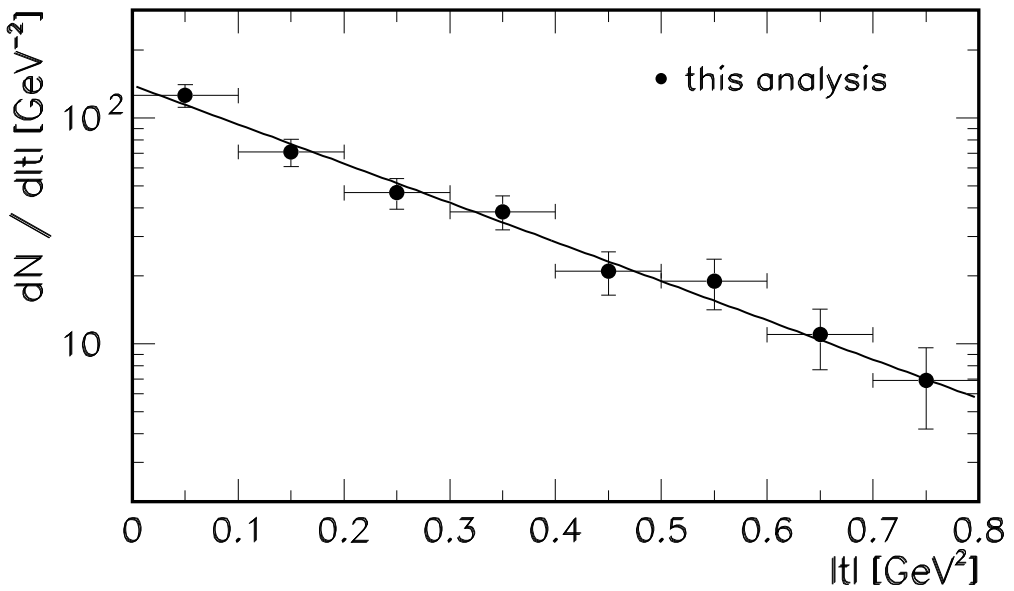

Figure 5.9: The corrected number of elastically scattered events $dN/d|t|$ as a function of $|t|$ for the energy region $40 < W_{\gamma p} < 150\,\text{GeV}$ together with a one parameter fit to the data of the form $dN/d|t| \propto b \cdot \exp(-b \cdot |t|)$ in the fit range $|t| \leq 0.8\,\text{GeV}^2$. The error bars show the statistical errors only.

The data are fitted up to $|t| = 0.8\,\text{GeV}^2$ with a two parameter exponential function of the form

$$\frac{dN}{d|t|} = \frac{1}{N_0} \cdot \exp(-b' \cdot |t|)\,. \tag{5.23}$$

The total number of events N corresponds to the integral of equation 5.23:

$$N = -\frac{1}{N_0} \cdot \frac{1}{b'} \cdot \exp(-b' \cdot |t|)\,. \tag{5.24}$$

The fitted absolute normalization $-\frac{1}{N_0} \cdot \frac{1}{b'}$ is then used as an input to perform a one parameter fit depending on the slope parameter b only:

$$\frac{dN}{d|t|} = -\frac{1}{N_0} \cdot \frac{b}{b'} \cdot \exp(-b \cdot |t|)\,. \tag{5.25}$$

The result for the elastic slope parameter b in the range $40 < W_{\gamma p} < 150\,\text{GeV}$ is thus (see table 5.3):

$$b = 4.2 \pm 0.2 \pm 0.6\,\text{GeV}^{-2} \qquad \text{at an average} \quad \langle W_{\gamma p} \rangle = 89.4\,\text{GeV}\,, \tag{5.26}$$

where the first error is statistical and the second gives the systematic uncertainty. A variation of the fit range has only a small influence on the resulting b value. The slightly different slope obtained when excluding the first bin from the fit or extending the fit up to $|t| = 1\,\text{GeV}^2$ is covered by the systematic uncertainty given in 5.26.

It has to be stressed that the b value obtained takes into account the smearing from $|t|$ to $p^2_{t,J/\psi}$. First of all the difference between those two variables in the chosen kinematic region is small compared to the bin width. Secondly, the data are corrected with respect to the generated t and are taken at the $|t|$ bin centres. And finally the model dependence on the assumed generated t behaviour is considered in the systematic error quoted.

The result for b is well compatible with previous H1 [64] ($b = 4.1 \pm 0.2 \pm 0.4\,\mathrm{GeV}^{-2}$)[4] and ZEUS [73] ($b = 4.6 \pm 0.6\,\mathrm{GeV}^{-2}$) photoproduction measurements at similar $\langle W_{\gamma p} \rangle$. It is also very similar to a recent measurement from H1 at higher Q^2 [71], which gives a slope parameter of $b = 4.1 \pm 0.3 \pm 0.4\,\mathrm{GeV}^2$ at a mean $\langle W_{\gamma p} \rangle = 96\,\mathrm{GeV}$ and at a mean $\langle Q^2 \rangle = 8\,\mathrm{GeV}^2$. It has to be stressed that no deviation from a single exponential can be found within the accessible range ($|t| < 1.5\,\mathrm{GeV}^2$).

The same procedure for fitting the slope parameter b is now adapted for the five bins in $W_{\gamma p}$ (see figure 5.10). The extracted values for b in the five $W_{\gamma p}$ bins are summarized in table 5.3 together with the global value from equation 5.26. They are also displayed in figure 5.11, where two different fits to these data are also shown. The dashed curve is a fit of a $W_{\gamma p}$ independent constant yielding a mean b of $4.5 \pm 0.3\,\mathrm{GeV}^{-2}$; the quality of the fit is quite good ($\chi^2/ndf = 0.82$). Assuming shrinkage of the diffractive peak (section 2.2.1) of the form

$$b = b_0 + 4 \cdot \alpha' \cdot \ln \frac{W_{\gamma p}}{90\,\mathrm{GeV}} \tag{5.27}$$

gives a slightly higher $\chi^2/ndf = 1.04$ with results $b_0 = 4.5 \pm 0.4\,\mathrm{GeV}^{-2}$ and $\alpha' = 0.1 \pm 0.2\,\mathrm{GeV}^{-2}$ (full curve in figure 5.11). The data from this analysis are compatible with both assumptions preferring slightly a flat behaviour of b with $W_{\gamma p}$. Note that the result for α' is compatible with zero as well as with the expected value from *soft* pomeron models of $\alpha' = 0.25\,\mathrm{GeV}^{-2}$.

	$40 < W_{\gamma p} < 55\,\mathrm{GeV}$	$55 < W_{\gamma p} < 70\,\mathrm{GeV}$	$70 < W_{\gamma p} < 85\,\mathrm{GeV}$
$< W_{\gamma p} >$ [GeV]	47.4	62.4	77.3
b [GeV^{-2}]	$4.08 \pm 0.34 \pm 0.57$	$4.55 \pm 0.29 \pm 0.64$	$5.30 \pm 0.38 \pm 0.74$
	$85 < W_{\gamma p} < 110\,\mathrm{GeV}$	$110 < W_{\gamma p} < 150\,\mathrm{GeV}$	$40 < W_{\gamma p} < 150\,\mathrm{GeV}$
$< W_{\gamma p} >$ [GeV]	97.2	129.1	89.4
b [GeV^{-2}]	$3.78 \pm 0.32 \pm 0.53$	$5.23 \pm 0.53 \pm 0.73$	$4.2 \pm 0.2 \pm 0.6$

Table 5.3: Summary of the elastic slope parameters b in bins of $W_{\gamma p}$. In the last bottom column the fit value for the entire $W_{\gamma p}$ range is given.

[4] Note that in this analysis a fit to dN/dp_t^2 instead of $dN/d|t|$ was performed. This is estimated to give a 10 % lower value for b, which is corrected here.

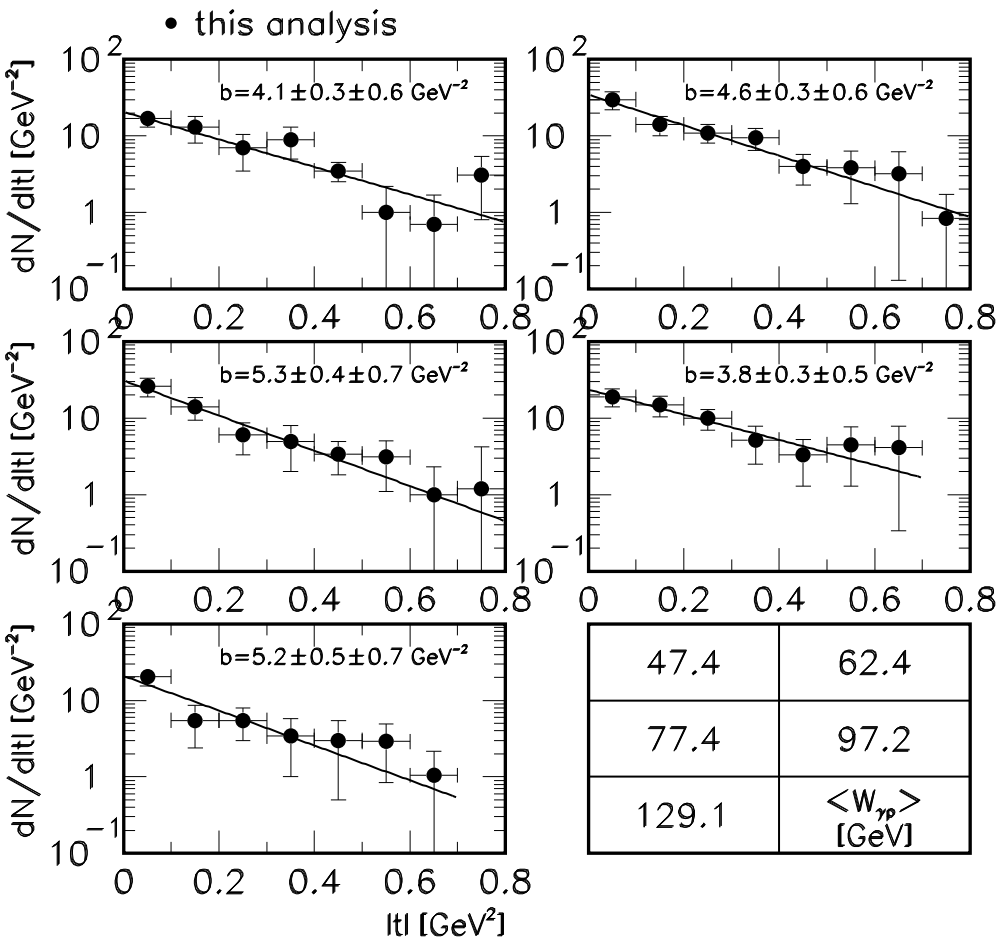

Figure 5.10: The corrected numbers of events $dN/d|t|$ as functions of $|t|$ for five bins in $W_{\gamma p}$ together with one parameter fits to the data of the form $dN/d|t| \propto b \cdot \exp(-b \cdot |t|)$ in the fit range $|t| \leq 0.8\,\mathrm{GeV}^2$. Only statistical errors are used. In the right bottom corner the mean $\langle W_{\gamma p} \rangle$ values for the chosen bins are given.

The combination of the results of this analysis with previous HERA measurements [78, 73] and low energy data of the E401 experiment [77] is shown in figure 5.12. Note that the E401 experiment is chosen following the discussion about compatibility between fixed target and HERA experiments in [78]. Since the E401 collaboration published a more complicated parameterisation of the $|t|$ dependence, a fit of the form $\propto \exp(-b|t|)$ was applied in [78] to the E401 data yielding $b = 3.2 \pm 0.5 \pm 0.5\,\mathrm{GeV}^{-2}$ at $W_{\gamma p} = 17\,\mathrm{GeV}$. This value (here called E401*) is then comparable with the HERA results. The results of the two types of fits to this enlarged data set are shown in figure 5.12. Similar to the data from this analysis alone (figure 5.11) the combination with E401* and previous HERA results is also compatible with both types of hypotheses, favouring slightly the assumption of shrinkage by a weak deviation (about two standard deviations) of α' from zero ($\alpha' = 0.18 \pm 0.09\,\mathrm{GeV}^{-2}$; $\chi^2/ndf = 1.80/3$), while the straight line fit yields a $\chi^2/ndf = 3.63/4$. The influence of the low energy point on the slope result due to the long lever arm is obvious. In order to be independent of normalization problems, differences in the targets and the separation of elastic and proton dissociative events, it would be desirable to extend the $W_{\gamma p}$ range within the HERA data itself.

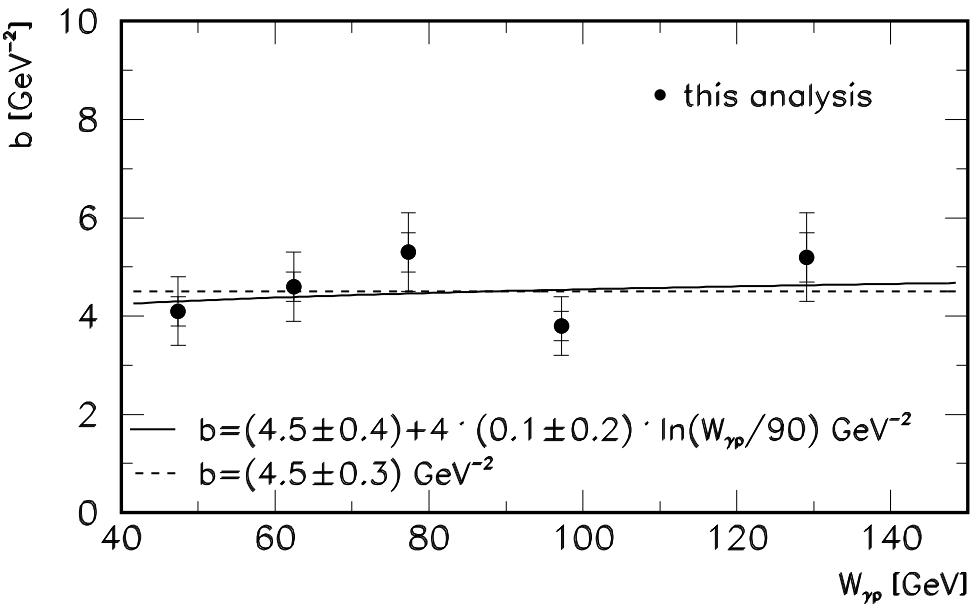

Figure 5.11: The results for b in the five $W_{\gamma p}$ bins from this analysis alone. The inner error bars are the statistical errors, while the outer bars are the statistical and the uncorrelated systematic errors added in quadrature. In addition two different fit results are shown, assuming the presence (full line) or the absence (dashed line) of shrinkage, respectively.

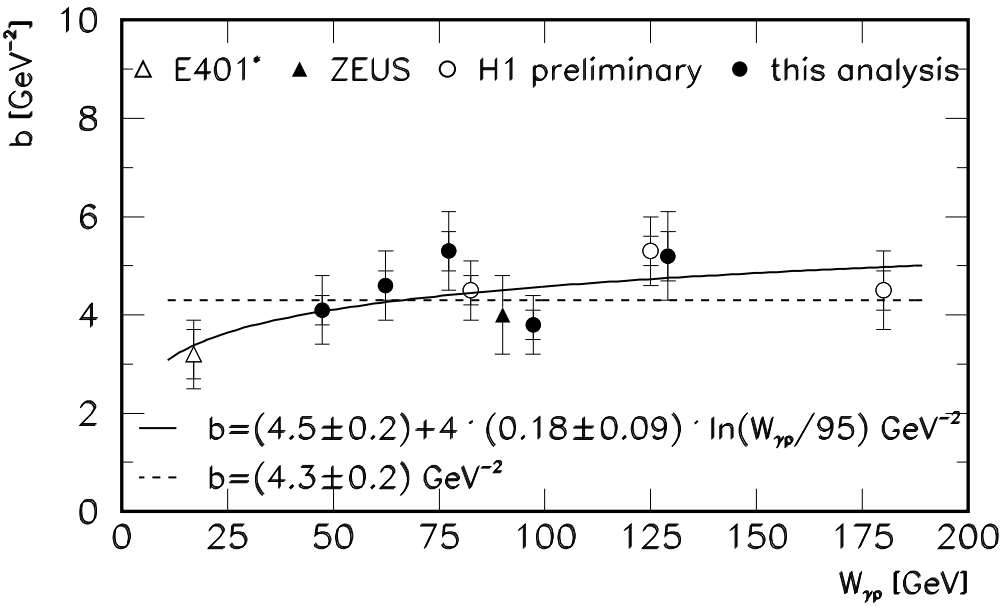

Figure 5.12: The b values in the five $W_{\gamma p}$ bins from this analysis together with previous independent H1 measurements, a published ZEUS result and a modified E401* value. The old H1 values are scaled up by 10% since they were not corrected for the difference between $|t|$ and p_t^2 (see [64]). The inner error bars are the statistical errors, while the outer bars are the statistical and the uncorrelated systematic errors added in quadrature. In addition two different fit results are shown, assuming the presence (full line) or the absence (dashed line) of shrinkage, respectively.

Results on the Slope Parameter in Proton Dissociation

For the extraction of the slope parameter for J/ψ events with proton dissociation the same procedure of background subtraction and efficiency correction is applied as for the elastically scattered J/ψ mesons but using the forward tagged events. The slope parameter is, however, only measured for the entire $W_{\gamma p}$ range ($40 < W_{\gamma p} < 150\,\mathrm{GeV}$). The corrected event distribution is shown in figure 5.13. Two major differences compared to the elastic case can be seen. First of all much higher $|t|$ values are reached and the distribution is harder than for elastically scattered J/ψ events, resulting in a smaller b value:

$$b_{pd} = 1.3 \pm 0.1 \pm 0.2\,\mathrm{GeV}^{-2} \qquad \text{for} \quad 0 \leq |t| \leq 2.5\,\mathrm{GeV}^2. \tag{5.28}$$

The systematic uncertainty on this result is assumed to be of the same order as for the elastic measurement (14 %). Nevertheless, a stronger model dependence is present, namely the dependence of the cross section on the mass of the dissociated system, M_Y, which is assumed within Regge theory to be $\sigma \propto 1/M_Y^{2.16}$. Deviations from this behaviour can change the cross section by up to a factor of two. This additional systematic error is not accounted for in the 14 % considered above.

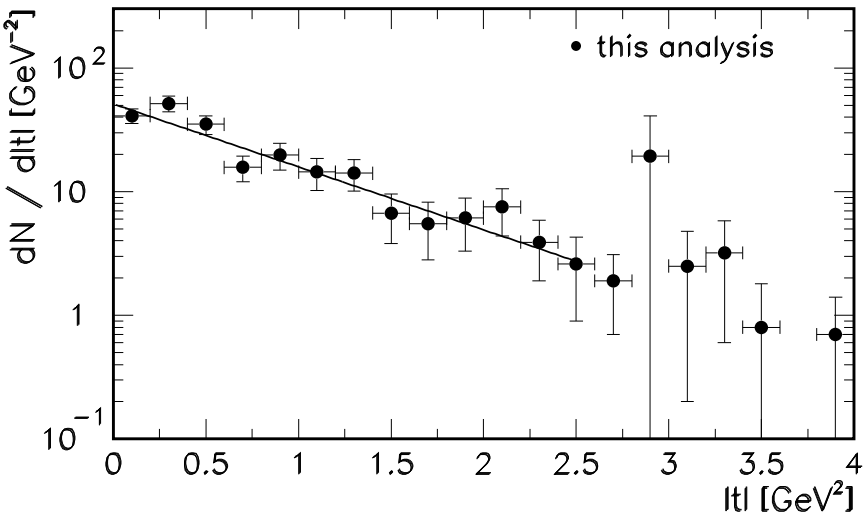

Figure 5.13: The corrected number of proton dissociative events $dN/d|t|$ as a function of $|t|$ for the entire energy range $40 < W_{\gamma p} < 150\,\mathrm{GeV}$ together with a fit to the data of the form $dN/d|t| \propto \exp(-b \cdot |t|)$ up to $|t| = 2.5\,\mathrm{GeV}^2$.

Furthermore, a suppression at the lowest $|t|$ values is visible. This effect can be attributed to a larger t_{min} for proton dissociative than for elastic J/ψ events due to $M_Y > m_p$ (see section 2.1). A change of the chosen fit range up to $|t| < 4\,\mathrm{GeV}^2$ has no significant effect on the resulting b value. Note that over the full accessible range in $|t|$ ($|t| \leq 4\,\mathrm{GeV}^2$) a good description ($\chi^2/ndf = 7.81/11$) of the data with only one exponential is achieved. Preliminary data [82] which use a different data selection and an extended t range ($|t| < 10\,\mathrm{GeV}^2$) found a change of slope at $|t| \simeq 1 - 2\,\mathrm{GeV}^2$. A comparison with these data in the overlap region has shown both data sets to be compatible within errors.

The result derived here is compatible with previous H1 measurements in photoproduction and in

DIS: $b = 1.7 \pm 0.3\,\mathrm{GeV}^{-2}$ [15] and $b = 1.9 \pm 0.4\,\mathrm{GeV}^{-2}$ ($\langle Q^2 \rangle = 8\,\mathrm{GeV}^2, \langle W_{\gamma p} \rangle = 96\,\mathrm{GeV}$; [3]), although it is slightly lower than these.

5.3 Regge Trajectory for Elastic J/ψ Production

A more instructive possibility besides the measurement of the $W_{\gamma p}$ dependence of the total elastic J/ψ cross section (section 5.1) or the slope parameter b (section 5.2.1) to shed light on the question whether the diffractive J/ψ photoproduction at HERA energies is a *soft* or a *hard* process, is to measure directly the Regge trajectory of the interaction. For a combination of HERA and fixed target J/ψ data this was done for the first time by A. Levy [83]. The same method is adapted here for H1 data only. While *soft* diffraction is characterized as a process in which one pomeron trajectory (*soft* pomeron) is exchanged, with the properties of having an intercept $\alpha_0 = 1.08$ and a slope $\alpha' = 0.25\,\mathrm{GeV}^{-2}$ (section 2.2.1), *hard* diffractive processes, seen e.g. in DIS reactions, seem to be described by a trajectory with a larger intercept and a smaller slope (*hard* pomeron; [19]).

Measuring the trajectory for elastically scattered J/ψ production is a more direct way to get information on its slope α' – and therefore on the presence or absence of shrinkage – than looking at the shrinkage of the diffractive peak with increasing energy (section 5.2.1), because no assumption has to be made about the t dependence of the cross section. The method consists in studying the $W_{\gamma p}$ dependence of $d\sigma/dt$ at fixed values of t:

$$\frac{d\sigma}{dt} = f(t) \cdot \left(\frac{W_{\gamma p}}{90\,\mathrm{GeV}} \right)^{4\alpha(t)-4}, \tag{5.29}$$

where $f(t)$ is a function of t only. Fitting the $W_{\gamma p}$ dependence of the differential γp cross section $d\sigma/dt$ with the functional form of equation 5.29 at different fixed t values allows one to determine $\alpha(t)$ at each t. Performing a linear fit to these values for $\alpha(t)$ of the form

$$\alpha(t) = \alpha_0 + \alpha' \cdot t \tag{5.30}$$

finally determines the trajectory $\alpha(t)$ with its slope α' and its intercept α_0.

5.3.1 Extraction of $d\sigma/dt$

Starting with the same forward untagged data set, which has already been described for the total γp cross section (section 4.2), the data are divided into five bins in $|t|$, each comprising six bins in $W_{\gamma p}$. The exact bin grid is listed in table 5.4 and is chosen such that the extracted number of J/ψ events (non-resonant background subtracted) is roughly the same in each of the 30 bins. In figure 5.14 the resulting 30 mass spectra between $2 < M_{\mu\mu} < 4\,\mathrm{GeV}$ are shown arranged in this bin grid: $W_{\gamma p}$ increases from the top row to the bottom, while $|t|$ increases from the left column to the right. The covered $W_{\gamma p}$ range is slightly different for each bin in $|t|$ (table 5.4).

In each mass plot the effective number of diffractive forward untagged J/ψ events is derived from a fit to the data of the same form as for the cross section determination in section 5.1.1, a

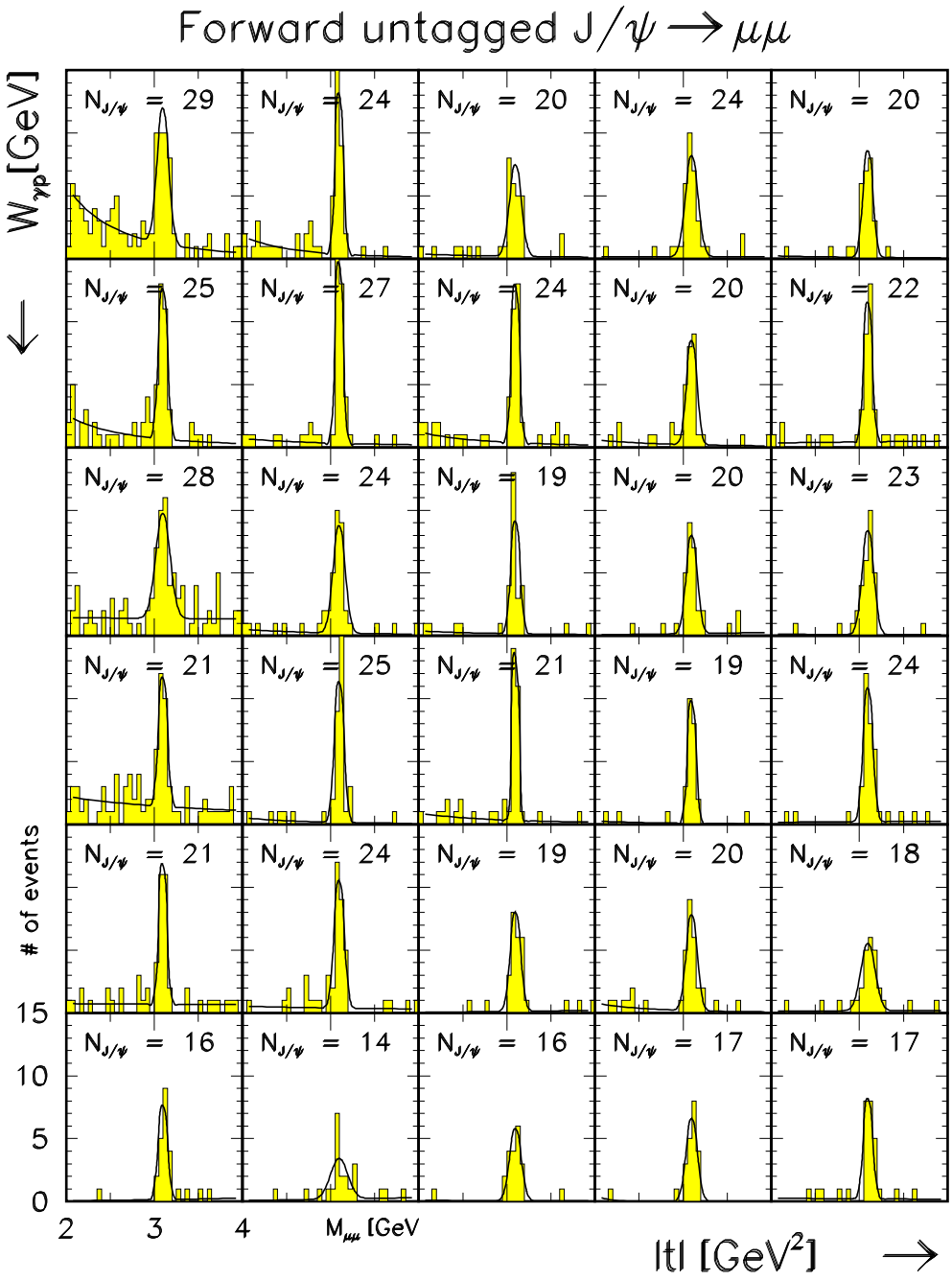

Figure 5.14: Forward untagged $J/\psi \to \mu\mu$ signals in the $W_{\gamma p} - |t|$-plane. Shown are the invariant mass distributions between $2 \leq M_{\mu\mu} \leq 4\,\text{GeV}$ in bins of $W_{\gamma p}$ and $|t|$, with $40 \leq W_{\gamma p} \leq 150\,\text{GeV}$ and $0 \leq |t| \leq 1.5\,\text{GeV}^2$; the size of each bin is given in table 5.4. The bins are chosen such that the number of signal events is approximately the same in each. The resulting number of J/ψ mesons is given in each bin; for details of the fit function see explanations in the text.

$\|t\|_{min}...\|t\|_{max}$ [GeV^{-2}]	1. $W_{\gamma p}$ bin [GeV]	2. $W_{\gamma p}$ bin [GeV]	3. $W_{\gamma p}$ bin [GeV]	4. $W_{\gamma p}$ bin [GeV]	5. $W_{\gamma p}$ bin [GeV]	6. $W_{\gamma p}$ bin [GeV]
0...0.053	40...57	57...66.5	66.5...78.5	78.5...95	95...114	114...150
0.053...0.134	40...54	54...67	67...79	79...91	91...110	110...150
0.134...0.25	40...54	54...67	67...79	79...90	90...110	110...150
0.25...0.44	40...53	53...64	64...77	77...87	87...108	108...150
0.44...1.5	40...53	53...64	64...74	74...87	87...105	105...150

Table 5.4: Choice of bin sizes in the $W_{\gamma p} - |t|$-plane. The bins are chosen such that the number of J/ψ mesons is roughly the same in each bin. The resulting mass spectra can be seen in figure 5.14.

sum of a Gaussian and a polynomial. Note that the non-resonant background is predominantly present in the lowest $|t|$ bin and decreasing with increasing $W_{\gamma p}$.

The numbers of forward untagged J/ψ events obtained by this fit are then corrected bin-by-bin for proton dissociative J/ψ background, acceptance and efficiency losses in the same way as described in 5.1.1. The decomposition of the total efficiency is given in figure 4.14. Indirect J/ψ events from $\psi(2S)$ decays are subtracted (independently of $|t|$ and $W_{\gamma p}$). The extraction of the total cross section $\sigma_{\gamma p}$ is then done exactly as described in section 5.1.1. The differential cross section $d\sigma/dt$ is obtained by dividing $\sigma_{\gamma p}$ in each $|t|$ bin by the specific width of that bin. The systematic error on each cross section point is taken from section 4.4. No additional systematic t dependence was found. In figure 5.15 the differential γp cross section $d\sigma/dt$, together with a fit of the form of equation 5.29, is shown in five bins of $|t|$.

The functional assumption of equation 5.29 fits the data very well in all five t bins. The t value at which this cross section and therefore the value $\alpha(t)$ is measured is determined by the mean of the generated t distribution within the $|t|$ bin. Varying the t dependence in the Monte Carlo gives a handle on the systematic error introduced by this. Also shown are the predictions from the soft and the hard Donnachie-Landshoff pomerons [19] as well as for the BFKL pomeron by Brodsky et al. [29].

5.3.2 Regge Trajectory

Finally, the resulting $\alpha(t)$ from the $d\sigma/dt$ fits (equation 5.29) at the mean t value at which they are derived are taken as an input for a linear fit of the form of equation 5.30. The Regge trajectory obtained is shown in figure 5.16 as a 1σ band taking into account correlations, yielding an intercept of $\alpha_0 = 1.26 \pm 0.05$ and a slope of $\alpha' = 0.05 \pm 0.15\,\text{GeV}^{-2}$.

In addition the expectations within the two-pomeron model by Donnachie and Landshoff [19] for the *soft* pomeron ($\alpha(t) = 1.08 + 0.25 \cdot t$) as well as for the *hard* pomeron trajectory ($\alpha(t) = 1.4 + 0.1 \cdot t$) and the BFKL pomeron of Brodsky et al. are displayed.

The error on the measurement, especially on the slope, is rather high. The intercept of the measured trajectory is found to be $\alpha_0 = 1.26 \pm 0.05$, thus lying in between the *soft* and the *hard*

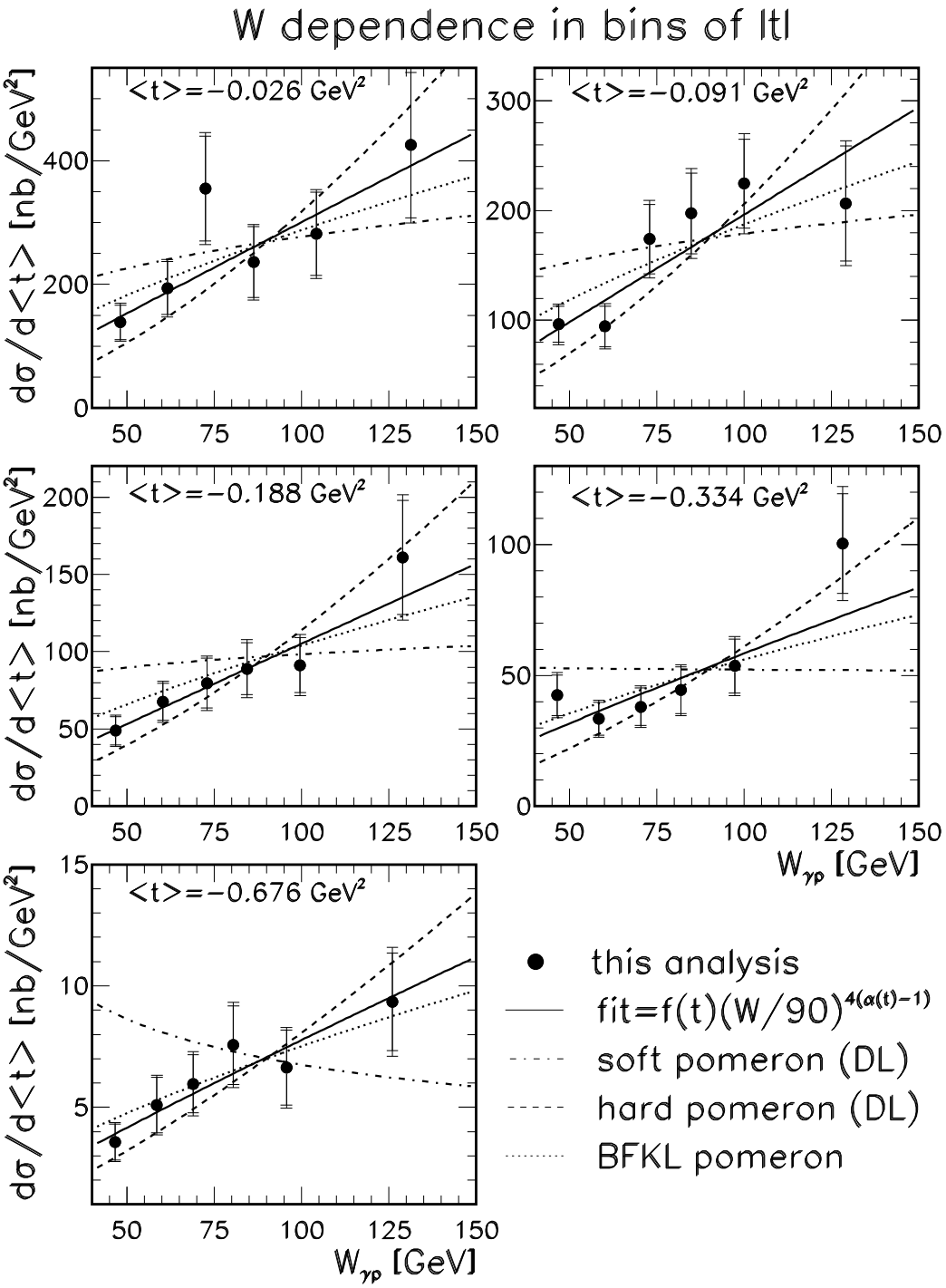

Figure 5.15: Shown is the differential γp cross section $d\sigma/dt$ in five bins of $|t|$ together with a fit of the form of equation 5.29. The mean t values at which the cross section is measured are given in each bin.

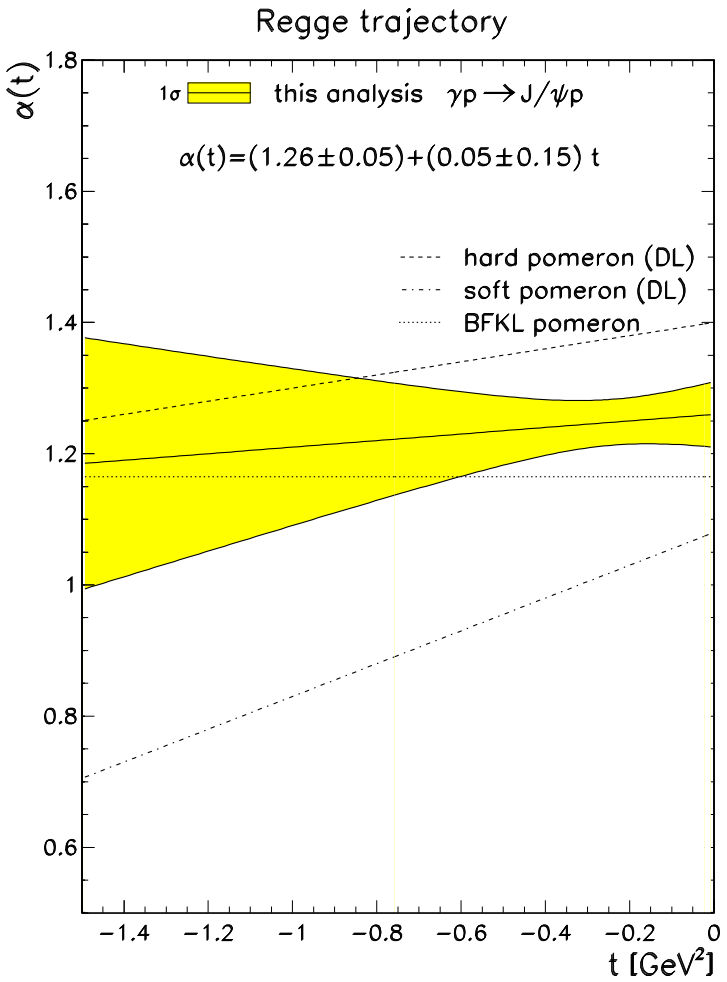

Figure 5.16: Displayed is the measured Regge trajectory for the process $\gamma p \to J/\psi p$ in photoproduction together with a fit to the data of the form of equation 5.30, giving results for $\alpha_0 = 1.24 \pm 0.06$ and $\alpha' = 0.007 \pm 0.220\,\mathrm{GeV}^{-2}$. Also shown are the *soft* and the *hard* pomeron trajectories.

pomeron's intercept, favouring the *hard* solutions. The measurement of the trajectory's slope ($\alpha' = 0.05 \pm 0.15\,\mathrm{GeV}^{-2}$) favours no shrinkage in J/ψ photoproduction in the HERA regime. The probability for α' to be zero is about 75 %, whereas the probability for α' to be 0.25 or larger is only 41 %.

5.4 Summary of J/ψ Results

In this chapter improved results on the energy dependence of the total photoproduction cross section, on the $|t|$ dependence, and on the energy dependence of the $|t|$ slope parameter were derived. A determination of the Regge trajectory for J/ψ production is carried out. These results shed further light on the mechanism of diffractive J/ψ photoproduction at HERA. While the production mechanism for the exclusive photoproduction of light vector mesons, such as φ

and ρ, at HERA energies is found to be dominated by *soft* pomeron exchange, J/ψ production seems to be driven by hard partonic processes.

- The measured $W_{\gamma p}$ dependence of the total γp cross section from this analysis alone ($40 \leq W_{\gamma p} \leq 150\,\text{GeV}$) yields:

$$\sigma_{\gamma p} \propto W_{\gamma p}^{0.96 \pm 0.16}\,. \tag{5.31}$$

  It is significantly steeper than predicted by *soft* pomeron exchange [18] ($\sigma_{\gamma p} \propto W_{\gamma p}^{0.22-0.32}$), but it is in fair agreement with an ad hoc approach in the context of Regge theory, the two–pomeron model [19] which assumes the exchange of two pomeron trajectories, a *soft* and a *hard* pomeron. A perturbative QCD calculation [39] in which the rise of the cross section reflects the increasing gluon density in the proton with decreasing momentum fraction x_g also gives a good description of the HERA data.

- The energy dependence derived from all available HERA data ($30 \leq W_{\gamma p} \leq 285\,\text{GeV}$) is:

$$\sigma_{\gamma p} \propto W_{\gamma p}^{0.81 \pm 0.08}\,, \tag{5.32}$$

  and from the entire accessible energy range ($15 \leq W_{\gamma p} \leq 285\,\text{GeV}$) including fixed target experiment data the result is:

$$\sigma_{\gamma p} \propto W_{\gamma p}^{0.83 \pm 0.05}\,. \tag{5.33}$$

- Results for the elastic slope parameter b are derived for the entire $W_{\gamma p}$ range:

$$b = 4.2 \pm 0.2 \pm 0.6\,\text{GeV}^{-2} \quad (\text{for} \;\; 40 \leq W_{\gamma p} \leq 150\,\text{GeV}, \langle W_{\gamma p} \rangle = 89.4\,\text{GeV})\,, \tag{5.34}$$

  as well as in five bins of $W_{\gamma p}$. No significant energy dependence can be seen from this measurement alone. This is also true for the combination with previous HERA data and a low energy measurement:

$$b = (4.5 \pm 0.2) + 4 \cdot (0.18 \pm 0.09) \cdot \ln \frac{W_{\gamma p}}{90\,\text{GeV}}\,\text{GeV}^{-2}\,. \tag{5.35}$$

  No deviation of the $|t|$ dependence of the elastic cross section from a single exponential can be seen in the accessible range ($|t| < 1.5$).

- The slope parameter in proton dissociative J/ψ production is measured to be:

$$b = 1.3 \pm 0.1 \pm 0.2\,\text{GeV}^{-2} \quad (\text{for} \;\; 40 \leq W_{\gamma p} \leq 150\,\text{GeV}, \langle W_{\gamma p} \rangle = 89.4\,\text{GeV})\,, \tag{5.36}$$

  which is much smaller than for the elastic process. A good description by one exponential is seen within the chosen fit range.

- The directly measured Regge trajectory exchanged in elastic J/ψ photoproduction at HERA favours the absence of shrinkage of the diffractive peak, but the data are not yet

precise enough to allow a final judgement on this question. The intercept and the slope of the measured trajectory are

$$\alpha(t) = (1.26 \pm 0.05) + (0.05 \pm 0.15)\,\mathrm{GeV}^{-2} \cdot t\,, \tag{5.37}$$

thus lying in between the two pomeron trajectories of [19] and being close to both the *hard* pomeron of Donnachie and Landshoff [19] and the BFKL *hard* pomeron by Brodsky et al. [29].

Finally, it can be summarized that the measurement of elastic J/ψ photoproduction at HERA shows good agreement with calculations in perturbative QCD as well as with results from Regge theory under the assumption of a second, *hard* pomeron. Based on the energy dependence of the cross section as well as on the favoured energy independence of the slope parameter, a pure *soft* production mechanism seems to be unlikely.

Chapter 6

Diffractive Υ Production

Since the cross section for the process $\gamma p \to \Upsilon p$ is predicted by perturbative QCD models [39, 84] to lie about two to three orders of magnitude below that for $\gamma p \to J/\psi p$, all available data have to be analysed in order to be able to see the Υ resonance in the H1 data at all. Therefore all $e^+ p$ data from 1994–1997 are analysed, corresponding to an integrated luminosity of $27.5\,\mathrm{pb}^{-1}$.

6.1 Selected Data Set

The selection of events with higher invariant masses ($5 \leq M_{\mu\mu} \leq 15\,\mathrm{GeV}$) is performed in a similar way to the J/ψ selection presented in chapter 4. A few changes are made, which take into account the signal-to-background ratio, which is considerably worse, and the different kinematics. In contrast to the J/ψ cross section measurement both decay muons have to be identified either in the LAr calorimeter or in the instrumented iron (corresponding to category B in table 3.6). For the cosmic muon rejection, in addition to the back-to-back requirement ($R_{\Delta\vartheta\Delta\varphi} > 1$) a cut on the CJC timing is also applied ($\Delta T_0 < 22$; compare section 4.1.5). The run selection for the 1996 and 1997 data taking periods corresponds to the one described in section 4.1.2. For 1994 and 1995 data those special runs in which the z_{vertex} is systematically shifted by $\pm 70\,\mathrm{cm}$, are excluded from the analysis. In addition the $e^- p$ data from 1994 are not taken into account.

Since the data from four different data taking periods are analysed and the trigger definitions, downscale factors and efficiencies changed during the four years, a more complex trigger mix than in the J/ψ analysis has to be chosen (see table 6.1). Three different types of triggers are used: triggers which are sensitive to a muon signature either in the barrel of the instrumented iron (`s19`, `s34` and `s15`) or in its endcaps (`s18`, `s22` and `s15`) as well as a trigger designed to recognize specifically events having a back-to-back topology (`s54`). The exact trigger requirements on all four trigger levels were already discussed in section 3.3.

The selection of photoproduction events[1] as well as the separation of elastic and proton dissociative Υ candidates is performed exactly as for the J/ψ selection (sections 4.1.4 and 4.1.1). The

[1] In 1994 instead of the backward calorimeter SpaCal a calorimeter called BEMC was installed. Using this device only those non-photoproduction events can be rejected which have a $Q^2 \geq 4\,\mathrm{GeV}^2$. From this results an average $\langle Q^2 \rangle = 0.11\,\mathrm{GeV}^2$ for all four years together.

1994	1995	1996	1997
s18	s19	s34	s15
s19	s54	s54	s34
s22			s54

Table 6.1: Overview of the triggers used in the Υ analysis.

acceptance range in $W_{\gamma p}$ is quite different for J/ψ ($40 \leq W_{\gamma p} \leq 150\,\text{GeV}$; compare figure 4.5) and Υ mesons ($70 \leq W_{\gamma p} \leq 250\,\text{GeV}$; compare figure 6.1).

The selection of Υ mesons starts from the preselection (up to line five in table 4.2); the cuts are summarized in table 6.2, where the reduction of event numbers is also listed.

The invariant mass spectrum is shown for the range $5 \leq M_{\mu\mu} \leq 15\,\text{GeV}$ in figure 6.2 at different stages of the analysis. In figure 6.2 a all events fulfilling the selection chain up to step seven in table 6.2 are shown. In figure b these events (open histogram) are compared to all those events fulfilling the trigger requirement in addition (shaded histogram; line eight in table 6.2). In figure c the difference between all triggered events (open histogram) and those which have a $Q^2 \leq 1\,\text{GeV}^2$ (or $Q^2 \leq 4\,\text{GeV}^2$ in 1994) (shaded histogram; line nine in table 6.2) and in figure 6.2 d the effect of the forward tagging can be seen (line ten in table 6.2).

The relative contributions from the states $\Upsilon(1S)$, $\Upsilon(2S)$ and $\Upsilon(3S)$ are roughly 10:2:3, estimated from $\text{BR} \times \Gamma_{ee}$ of each state (see table 6.3). Because of the mass resolution of the detector it is not possible to distinguish these states experimentally. The peak and width which are found in the data are compatible with the sum of the three Υ states estimated by Monte Carlo simulation,

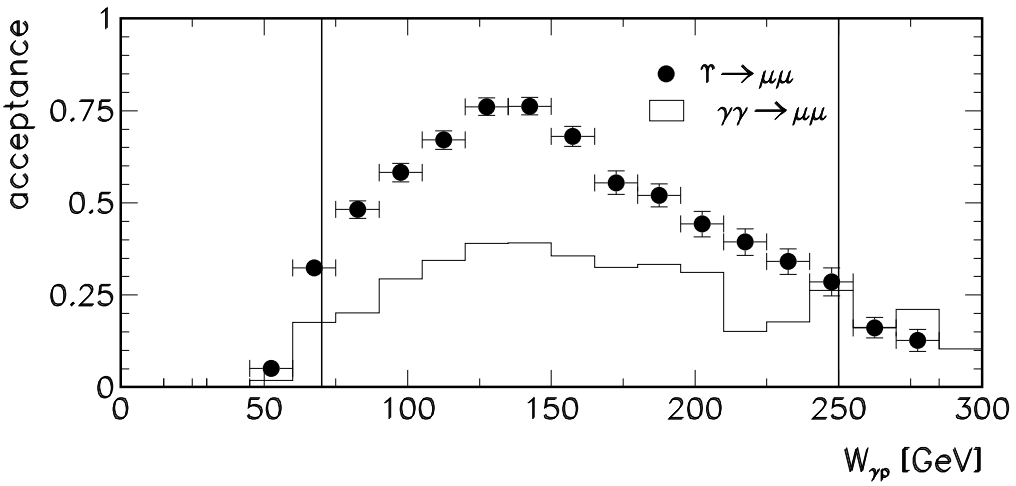

Figure 6.1: Acceptance in $W_{\gamma p}$ for a polar angular cut of $20^\circ \leq \vartheta_\mu \leq 165^\circ$. Shown are the distributions from an Υ Monte Carlo (points) and from simulated QED two–photon processes with $M_{\mu\mu} > 5\,\text{GeV}$ (histogram). In addition the $W_{\gamma p}$ region used in this analysis ($70 \leq W_{\gamma p} \leq 250\,\text{GeV}$) is indicated.

Selection Step		1994	1995	1996	1997	$\sum$
1	$5 \leq M_{\mu\mu} \leq 15\,\text{GeV}$	729	3768	9990	7945	22432
2	Final muon identification	523	2696	7038	5495	15752
3	Exactly two good central tracks	489	2676	6960	5351	15476
4	$\lvert z_{vertex}\rvert \leq 40\,\text{cm}$	449	2433	6857	5169	14908
5	Cosmic muon rejection	93	88	147	339	667
6	Run selection	86	81	124	280	571
7	$70 \leq W_{\gamma p} \leq 250\,\text{GeV}$	67	68	103	233	471
8	Trigger	60	48	68	164	340
9	Photoproduction	55	45	57	142	299
10	No forward tag	30	33	38	87	188

Table 6.2: Reduction of the data volume during the Υ selection.

although the peak in the data is narrower than in the simulation assuming the ratio 10:2:3 (see figure 6.6). This might be a hint for the higher $\Upsilon(1S)$ contribution of $\sim 85\,\%$ as calculated in [43] (see figure 6.7).

	$\Upsilon(1S)$	$\Upsilon(2S)$	$\Upsilon(3S)$
$M_\Upsilon\,[GeV]$	9.46	10.02	10.36
$\text{BR}(\Upsilon \to \mu\mu)\,[\%]$	2.48	1.31	1.81

Table 6.3: Properties of the Υ mesons taken from [67].

6.2 Efficiencies and Systematic Errors

The data are corrected for all acceptance and efficiency losses using simulated DIFFVM Υ events. The adequate description of the data by the detector simulation has already been proven for the J/ψ analysis; no differences are expected here. Nevertheless some checks are made for the entire mass range ($5 \leq M_{\mu\mu} \leq 15\,\text{GeV}$) as well as for a tight mass window around the Υ resonance ($9 \leq M_{\mu\mu} \leq 10\,\text{GeV}$). The data are compared to a mixture of LPAIR and DIFFVM[2] Monte Carlo events (figure 6.3). While the number of $\gamma\gamma \to \mu\mu$ events is normalized to the luminosity, the number of simulated Υ events is chosen in order to fit roughly the number of data events in the resonance peak. The ratio of elastic and proton dissociative simulated events is taken from the J/ψ analysis (section 4.3.4).

[2]The modelled $W_{\gamma p}$ dependence is chosen differently for the Υ simulation than for the J/ψ Monte Carlo, according to the latest findings in perturbative QCD calculations [43]: $\sigma_{\gamma p} \propto W_{\gamma p}^{1.7}$.

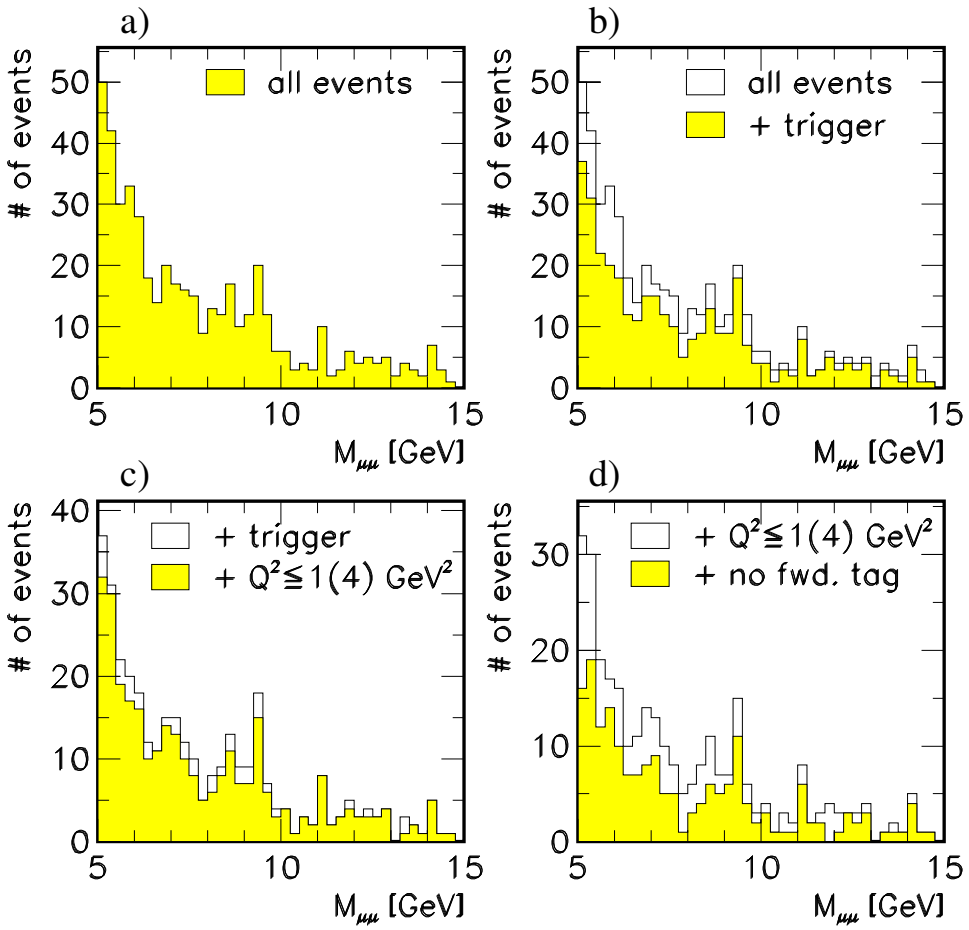

Figure 6.2: Invariant mass spectra at different stages of the ϒ selection: a) for all events fulfilling the selection chain up to step seven in table 6.2, b) all events as in a) compared to all events fulfilling the trigger requirement in addition (line eight in table 6.2), c) all events which fulfil the trigger conditions compared to those with a low Q^2 ($Q^2 \leq 1(4)\,\mathrm{GeV}^2$) (line nine in table 6.2) and d) the events from c) compared to all events which are forward untagged in addition (line ten in table 6.2).

Shown is the invariant mass distribution (figure 6.3 a), the difference of the azimuthal angle between the two decay muons (b and e), the polar angle of the muons (c and f) and their transverse momentum (d and g). On the left hand side (a-d) events for the entire mass range are shown, while on the right hand side (e-g) only events from the mass window are chosen, where roughly half of the events should stem from ϒ meson production. A sufficiently good description of the data is found in all the variables. The overall efficiency for elastic ϒ events to pass the entire selection chain is 24 %, determined by the simulation.

In order to estimate the total systematic error on the ϒ cross section measurement most of the errors evaluated for the J/ψ cross section (table 4.3) are adopted with the exception of the error on the number of measured ϒ events in the data, the knowledge of the trigger efficiency and the bin centre correction. The different sources of systematic errors on the ϒ cross section measurement are summarized in table 6.4.

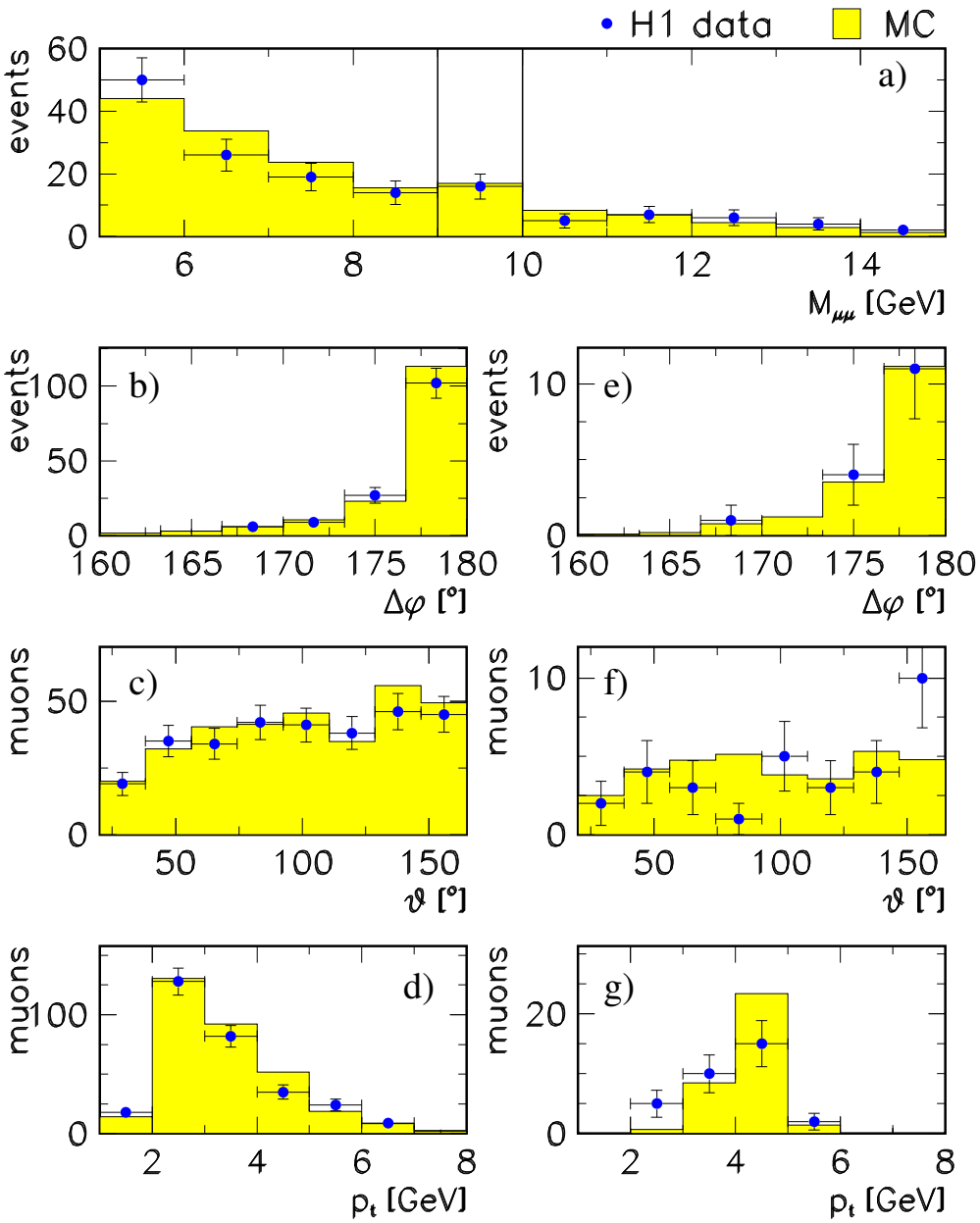

Figure 6.3: Comparison between data and Monte Carlo simulation for elastic two-muon events in photoproduction. a) Invariant mass of the muon pair between 5 and 15 GeV, b) and e) azimuthal opening angle of the muon pair $\Delta\varphi$, c) and f) polar angle of the muons ϑ_μ and d) and g) transverse momentum of the muons p_t. In figures a)-d) events with an invariant mass between 5 and 15 GeV are shown, for e)-g) only those between 9 and 10 GeV, where roughly half of the events should stem from Υ meson production. The full points are the data and the shaded histograms show the Monte Carlo simulation, which is a sum of LPAIR (normalized to the data luminosity) and DIFFVM (normalized to fit the mass peak in the data).

The fit used to extract the number of events is varied for the background component from a power law to an exponential. The binning and the fit range are varied in addition. The estimated error on the number of Υ events N_Υ is then 15 %. The error on the trigger efficiency is estimated by using two independent trigger sets to compute the cross section. These two cross section values are found to agree within statistical errors. The difference is used to estimate the systematic error on the trigger efficiency, yielding 16 %. Varying the $W_{\gamma p}$ dependence ($\sigma \propto W_{\gamma p}^{\delta}$) in the simulation as $\delta = 1.7 \pm 0.8$ results in a cross section error of 4 %.

The systematic errors on the track and vertex efficiency (4 %), on the z_{vertex} distribution (1 %), on the lepton identification (6.5 %) and on the forward tagging (7 %) are taken from the J/ψ analysis (table 4.3). The error on the luminosity measurement averaged over all four years is 1.55 %. For the branching ratio $\mathrm{BR}(\Upsilon(1S) \to \mu^+\mu^-)$ the error (2.8 %) is taken from [67].

The total systematic error on $\sigma \times \mathrm{BR}$ amounts to 24.7 % and for σ it is 24.9 %.

	Source	Amount [%]
1	Track and vertex efficiency	4
2	z_{vertex} distribution	1
3	Trigger efficiency	16
4	Number of signal events	15
5	Lepton identification	6.5
6	Forward tagging	7
7	Modelled $W_{\gamma p}$ dependence	4
8	Luminosity	1.55
	Total systematic error on $\sigma \times \mathrm{BR}$	24.7
9	$\Upsilon(1S)$ branching ratio	2.8
	Total systematic error on σ	24.9

Table 6.4: Systematic uncertainties taken into account for the Υ cross section measurement. Contributions one, two, five and six are taken from the J/ψ analysis.

6.3 Cross Section

The extraction of the Υ cross section follows a slightly different procedure than in the case of the J/ψ cross section described in section 5.1.2.

The events fulfilling all the cuts (figure 6.2 d, shaded histogram) are used. The number of Υ events is determined by fitting a Gaussian for the resonance plus a power law for the non-resonant background to the invariant mass distribution. The result of this fit is shown in figure 6.4. For comparison the signal is shown for all selected events neglecting the cuts on photo-

production and on the forward tag in figure 6.5. In addition the expectation for the non-resonant $\gamma\gamma \to \mu\mu$ background as simulated with the LPAIR generator is given as the shaded histogram.

The number of forward untagged Υ events in the data ($N_\Upsilon^{notag} = 11.6 \pm 4.8$) is then translated into the number of elastic Υ mesons using the following relation:

$$N_\Upsilon = N_\Upsilon^{notag} \cdot (1 - f_{pd}) \cdot (1 + f_{noise}^{FMD}), \tag{6.1}$$

with f_{pd} being the remaining background from proton dissociation ($f_{pd} = 16\,\%$), estimated using the simulation, and f_{noise}^{FMD} being a correction factor for noise hits in the Forward Muon Detector, which are not simulated ($f_{noise}^{FMD} = 3\,\%$). Using this number of elastic Υ mesons ($N_\Upsilon = 10.0 \pm 4.1$), the total efficiency ($\varepsilon = 24\,\%$), the integrated luminosity from all four years ($\int \mathcal{L} dt = 27.5\,\text{pb}^{-1}$) and the integrated photon flux ($\mathcal{F} = 0.0827$; see equation 5.17) for the $W_{\gamma p}$ range analysed here ($70 \leq W_{\gamma p} \leq 250\,\text{GeV}$), one calculates the photon–proton cross section times branching ratio at the bin centres $\langle W \rangle = 143\,\text{GeV}$ and $\langle Q^2 \rangle = 0.11\,\text{GeV}^2$ for the sum of all three Υ states $\Upsilon(1S)$, $\Upsilon(2S)$ and $\Upsilon(3S)$:

$$\sigma_{\gamma p \to \Upsilon p} \times \text{BR} = \frac{N_\Upsilon}{\varepsilon \cdot \int \mathcal{L} dt \cdot \mathcal{F}}. \tag{6.2}$$

The resulting value is

$$\sigma_{\gamma p \to \Upsilon p} \times \text{BR} = 18.3 \pm 7.6 \pm 4.5\,\text{pb},$$

where Υ stands for the sum over the states $\Upsilon(1S)$, $\Upsilon(2S)$ and $\Upsilon(3S)$. The first error is the statistical error and the second the systematic uncertainty.[3] All relevant numbers are listed in table 6.5. The preliminary H1 measurement [40] is: $\sigma_{\gamma p \to \Upsilon p} \times \text{BR} = 16.0 \pm 7.5 \pm 4.0\,\text{pb}$ at $\langle W_{\gamma p} \rangle = 160\,\text{GeV}$ and the corresponding published ZEUS result [41] is $\sigma_{\gamma p \to \Upsilon p} \times \text{BR} = 13.3 \pm 6.0^{+2.7}_{-2.3}\,\text{pb}$ at an average $\langle W_{\gamma p} \rangle = 120\,\text{GeV}$.

The value for $\sigma \times \text{BR}$ for the sum of all three Υ states can be translated into the photoproduction cross section for the $\Upsilon(1S)$ alone taking into account the relative contributions of the three states, which are, however, not well known. In figure 6.6 a the relative contributions from $\Upsilon(1S)$, $\Upsilon(2S)$ and $\Upsilon(3S)$ are shown assuming the ratio 10:2:3 as naively expected from the branching ratios and the electronic decay widths of each state. These contributions are given in figure 6.6 b summed up on top of the non-resonant background as simulated by the LPAIR generator. In figure 6.7 the mass spectra are displayed assuming the ratios 10:1.1:0.6 as predicted in [43]. The shape of the mass spectrum as measured in the data (figure 6.5) is more similar to that in figure 6.7 b than that in figure 6.6 b.

Using the branching ratios into muons and the electronic widths of the different Υ resonances, the ratio of $\Upsilon(1S) : \Upsilon(2S) : \Upsilon(3S)$ is then roughly $10 : 2 : 3$ corresponding to $10/15 \simeq 66\,\% \Upsilon(1S)$ contribution. The relative contribution of the $\Upsilon(1S)$ is measured by the CDF Collaboration [85] to be about 70 %. However, it has to be stressed that the predominant production process for Υ mesons at Fermilab is the gluon-gluon-fusion process and not a diffractive mechanism.

[3] The result presented here differs slightly from the H1 result on Υ photoproduction as presented in Vancouver [40] due to additional knowledge gained from the J/ψ analysis (chapter 4), but they are well compatible within the errors.

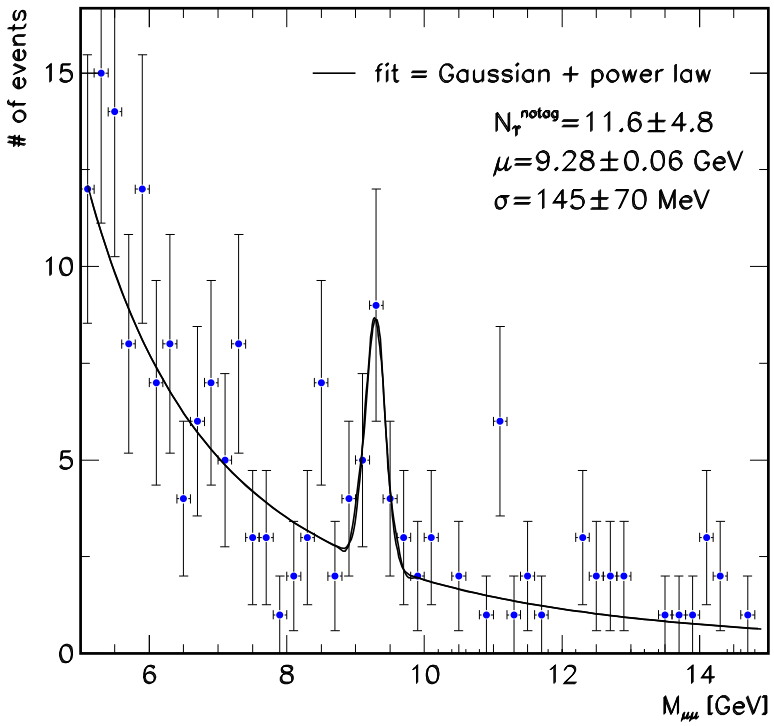

Figure 6.4: Invariant mass spectrum for the elastic Υ selection (line 10 in table 6.2) together with a fit of a Gaussian for the resonance plus a power law for the non-resonant background. In addition the fit results for the number of Υ events N_Υ, the peak position μ and the width of the peak σ are quoted.

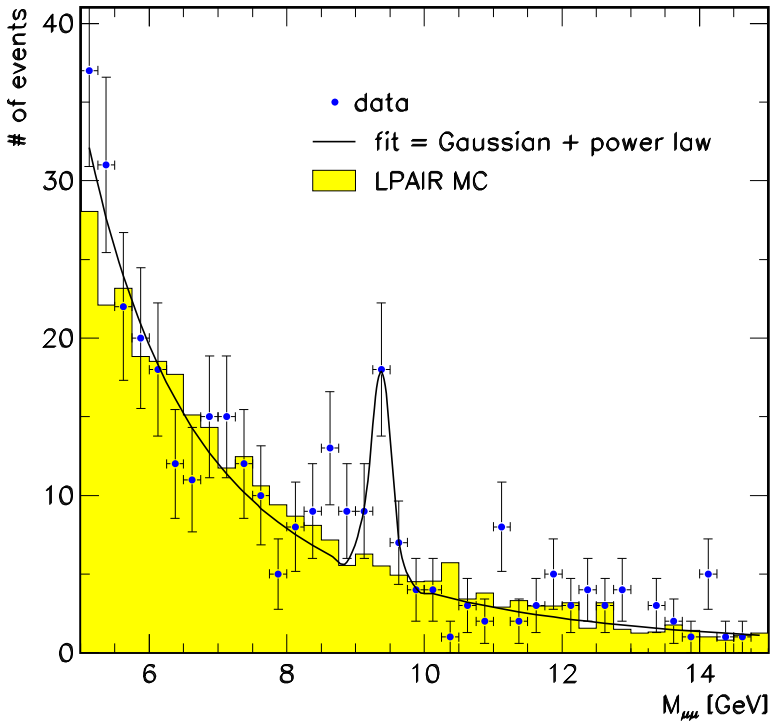

Figure 6.5: Invariant mass spectrum for the diffractive Υ selection neglecting the cut on photoproduction (line 8 in table 6.2) together with a fit of a Gaussian for the resonance plus a power law for the non-resonant background. The shaded histogram gives the expectation for the non-resonant $\gamma\gamma \to \mu\mu$ background as simulated with the LPAIR generator.

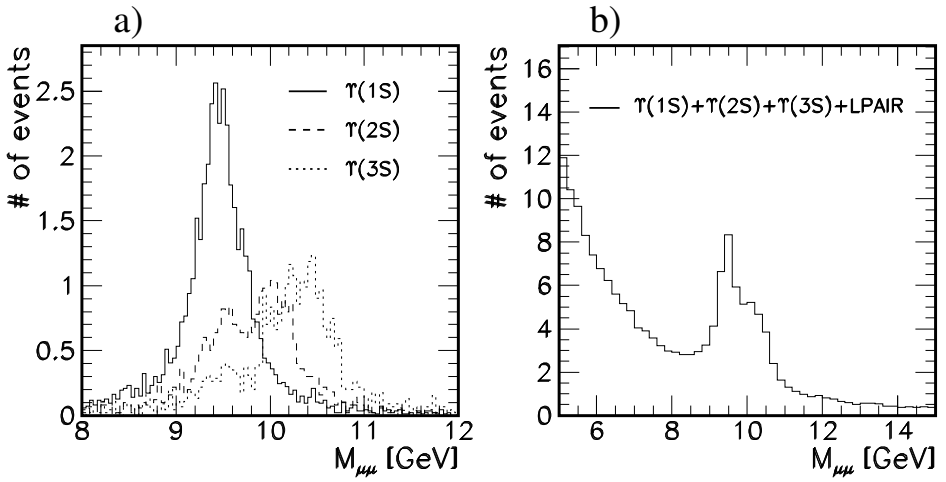

Figure 6.6: Invariant mass spectra as expected from Υ and LPAIR Monte Carlo mixture: a) the single contributions from the three Υ states with the relative weights of 10:2:3, b) all three Υ states summed up on top of the non-resonant background.

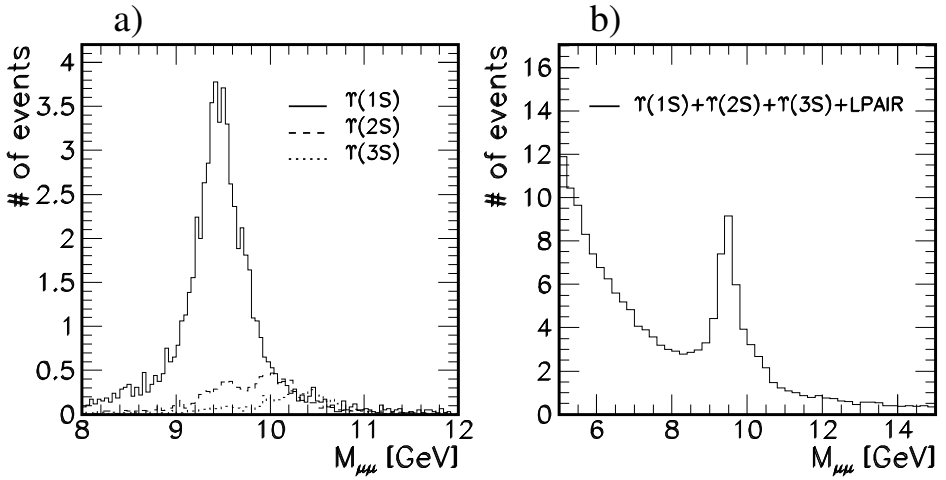

Figure 6.7: Invariant mass spectra as expected from Υ and LPAIR Monte Carlo mixture: a) the single contributions from the three Υ states with the relative weights of 10:1.1:0.6 [43], b) all three Υ states summed up on top of the non-resonant background.

The latest pQCD calculations [43] assign about 85 % (10:1.1:0.6) of the total cross section to the $\Upsilon(1S)$ state. Assuming 70 % contribution from $\Upsilon(1S)$ and the branching ratio from [67] $\mathrm{BR}(\Upsilon(1S) \to \mu^+\mu^-) = (2.48 \pm 0.07)\,\%$ the result for the elastic $\Upsilon(1S)$ photoproduction cross section is:

$$\sigma(\gamma p \to \Upsilon(1S)p) = 520 \pm 210 \pm 130\,\mathrm{pb},$$

where the first error is the statistical error and the second the systematic uncertainty. Assuming 85 % $\Upsilon(1S)$ contribution instead of 70 %, the corresponding result would be $\sigma(\gamma p \to \Upsilon(1S)p) = 630 \pm 260 \pm 160\,\mathrm{pb}$.

In figure 6.8 the measured cross section $\sigma_{\gamma p \to \Upsilon(1S)p}$ is compared to the latest ZEUS measurement [86], which includes in addition to the published result also a contribution from $\Upsilon \to ee$,

$70 \leq W_{\gamma p} \leq 250\,\text{GeV}$, $Q^2 \leq 1(4)\,\text{GeV}^2$				
N_Υ^{notag}	$f_{pd}\,[\%]$	$\varepsilon\,[\%]$	N_Υ	$\int \mathcal{L} dt\,[\text{pb}^{-1}]$
11.6 ± 4.8	16	24	10.0 ± 4.1	27.5
$\mathcal{F}$	$\langle W_{\gamma p} \rangle\,[GeV]$	$\sigma_{\gamma p \to \Upsilon p} \times \text{BR}\,[\text{pb}]$	$\sigma_{\gamma p}\,[\text{pb}]$	
0.0827	143	$18.3 \pm 7.6 \pm 4.5$	$520 \pm 210 \pm 130$	

Table 6.5: Summary of the elastic Υ cross section. The errors on N_Υ^{notag} and N_Υ are the statistical error from the fit to the data. The first error on the cross section is the statistical one and the second is the systematic uncertainty.

and to different pQCD calculations [39, 43, 44]. It can be seen that the recent calculations, namely the two different methods by Martin, Ryskin, Teubner (MRT) [44] and the updated calculations by Frankfurt, Strikman, McDermott (FSM) [43], are well compatible with the data points. The older calculation [39] by Frankfurt, Koepf, Strikman (FKS) based on the model used for J/ψ production, was the only one available at the time when the first HERA measurements were shown. It is about five times below the data, which however is only two standard

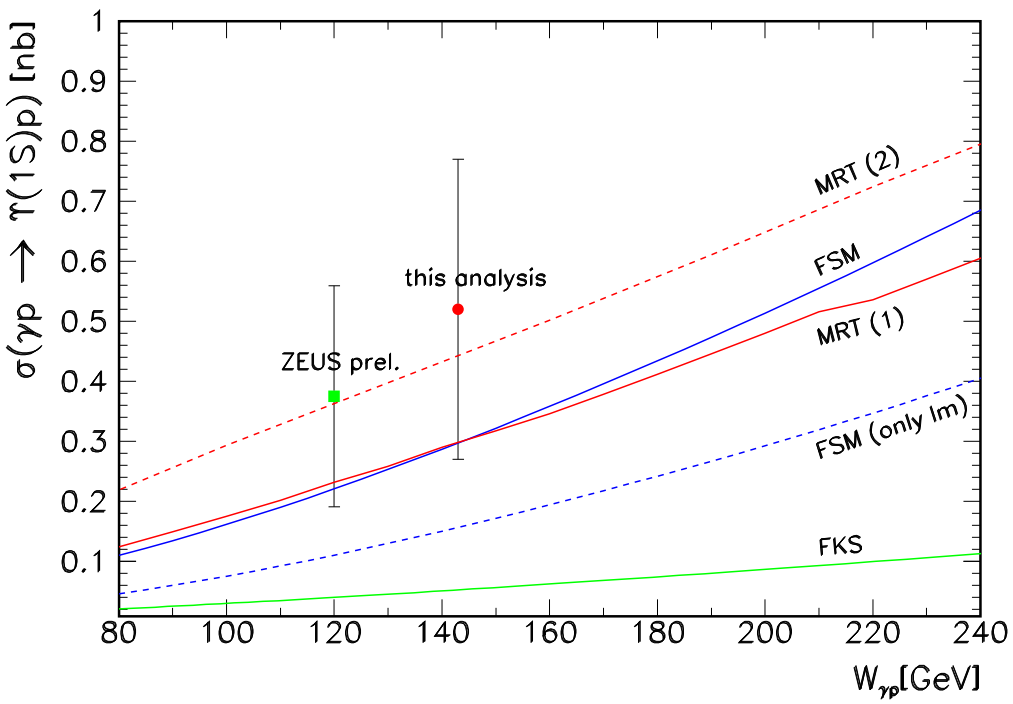

Figure 6.8: The Υ photoproduction cross section from this analysis together with the latest ZEUS result [86] compared to different pQCD calculations. The error bars show the statistical and the systematic error added in quadrature.

deviations (curve labeled 'FKS' in figure 6.8).

The main difference between the old and new calculations by Frankfurt et al. is based on two effects, which turned out to be much more important for Υ than for J/ψ production: the off-diagonal (or skewed) kinematics and the large magnitude of the real part of the amplitude (section 2.3.1). The effect of the skewedness (sketched in figure 2.7), which arises from the need to convert a space-like $-Q^2$ into a time-like M_V^2, and is given by the difference in momentum fractions carried by the outgoing and the returning gluons, can be seen from the difference of the curves labeled 'FKS' and 'FSM (only Im)' in figure 6.8.

The gluon emitted by the proton carries the proton momentum fraction x' from the proton, while it has only the momentum fraction x with $x \ll x'$ when coupling to the quark. The returning gluon carries $x - \xi$ at the quark-gluon vertex and $x' - \xi$ at the proton-gluon vertex. Because the momentum fraction x and the difference in momenta of outgoing and returning gluon are of the same order of magnitude ($x \approx \xi$), skewed parton density functions are probed at the vector meson level.

The contribution from the real part of the amplitude is expressed in the difference between the 'FSM' and the 'FSM (only Im)' curves. Both effects – the contribution of the real part of the amplitude and the skewed kinematics – are roughly of the same order of magnitude: each about a factor of two in the cross section.

In their first method Martin et al. use the same leading order QCD calculation as Frankfurt et al. considering relativistic corrections, the real part of the amplitude, off-diagonal partons and NLO corrections. The result of this calculation is shown with the curve labeled 'MRT (1)' in figure 6.8 and agrees well with [43]. They use a second method based on parton-hadron duality. The procedure is to calculate the amplitude for open $b\bar{b}$ production, then to project the amplitude onto the $J^P = 1^-$ state and finally to integrate the cross section over an appropriate interval ΔM of the mass of the $b\bar{b}$ pair which includes the resonance peak. The result of this calculation is shown as the curve labeled 'MRT (2)'.

6.4 Summary of Υ Results

The here presented measurement of the $\Upsilon(1S)$ photoproduction cross section in the energy range $70 < W_{\gamma p} < 250\,\text{GeV}$ at an average $\langle W_{\gamma p} \rangle = 143\,\text{GeV}$ yields:

$$\sigma_{\gamma p \to \Upsilon p} = 520 \pm 210 \pm 130\,\text{pb}. \tag{6.3}$$

Taking the different average $\langle W_{\gamma p} \rangle$ into account, this result is in good agreement with the measurement by the ZEUS collaboration [41]: $\sigma_{\gamma p \to \Upsilon p} = 375 \pm 170^{+75}_{-64}\,\text{pb}$ at $\langle W_{\gamma p} \rangle = 120\,\text{GeV}$. The analysis presented here is based on the same data as the preliminary H1 measurement from [40] using some additional knowledge gained from the J/ψ analysis as performed in chapter 4 and is in good agreement with the previous result.

Comparing the measurements with pQCD calculations [39, 43, 44] it is noticeable that the same calculations which are able to describe the measured J/ψ photo- and electroproduction cross

sections in size and $W_{\gamma p}$ and Q^2 dependence [39] were lower in the case of the Υ photoproduction cross section [39]. This discrepancy triggered a recalculation [43, 44] considering two main effects, namely the skewed parton densities and the real part of the amplitude, which play a more important role than in case of the J/ψ. All three new calculations, obtained with different methods, are in agreement with each other and with the available data points. A strong correlation between the mass of the diffractively produced state and the energy dependence of the cross section is found. In particular, a considerably stronger rise in energy is predicted ($\sigma \propto W_{\gamma p}^{\sim 1.7}$) than that found in J/ψ photoproduction ($\sigma \propto W_{\gamma p}^{\sim 0.8}$).

Chapter 7

Summary and Conclusions

Measurements are presented to shed further light on the mechanism of diffractive heavy vector meson production at HERA. While the production mechanism for the exclusive photoproduction of light vector mesons, such as ρ and ϕ, at HERA energies were found to be dominated by *soft* pomeron exchange, the data presented here on J/ψ and Υ production show that they are driven by hard processes.

- The total elastic J/ψ photoproduction cross section over the entire accessible energy range ($15 \leq W_{\gamma p} \leq 285\,\mathrm{GeV}$) including previous HERA and fixed target experiment data gives the most precise measurement of the $W_{\gamma p}$ dependence:

$$\sigma_{\gamma p \to J/\psi p} \propto W_{\gamma p}^{0.83 \pm 0.05} \,. \tag{7.1}$$

  It is significantly steeper than predicted by *soft* pomeron exchange [18] ($\sigma_{\gamma p} \propto W_{\gamma p}^{0.22-0.32}$), but it is in fair agreement with an ad hoc approach in the context of Regge theory, the two–pomeron model [19] which assumes the exchange of two pomeron trajectories, a *soft* and a *hard* pomeron. A perturbative QCD calculation [39] in which the rise of the cross section reflects the increasing gluon density in the proton with decreasing momentum fraction x also gives a good description of the HERA data.

- Results for the elastic slope parameter b in J/ψ photoproduction are derived for the entire $W_{\gamma p}$ range:

$$b = 4.2 \pm 0.2 \pm 0.6\,\mathrm{GeV}^{-2} \quad (\text{for } \; 40 \leq W_{\gamma p} \leq 150\,\mathrm{GeV}, \langle W_{\gamma p} \rangle = 89.4\,\mathrm{GeV}\,) \,, \tag{7.2}$$

  as well as in five bins of $W_{\gamma p}$. No deviation of the $|t|$ dependence of the elastic cross section from a single exponential can be seen in the accessible range ($|t| < 1.5$). No significant energy dependence can be seen from this measurement alone. This is also true for the combination with previous HERA data and a low energy measurement:

$$b = (4.5 \pm 0.2) + 4 \cdot (0.18 \pm 0.09) \cdot \ln \frac{W_{\gamma p}}{90\,\mathrm{GeV}}\,\mathrm{GeV}^{-2} \,. \tag{7.3}$$

- The slope parameter in proton dissociative J/ψ photoproduction is measured to be:

$$b = 1.3 \pm 0.1 \pm 0.2\,\mathrm{GeV}^{-2} \quad (\text{for } \; 40 \leq W_{\gamma p} \leq 150\,\mathrm{GeV}, \langle W_{\gamma p} \rangle = 89.4\,\mathrm{GeV}\,), \quad (7.4)$$

  which is much smaller than for the elastic process. A good description by one exponential is seen within the chosen fit range ($|t| < 2.5\,\mathrm{GeV}^2$).

- The directly measured Regge trajectory exchanged in elastic J/ψ photoproduction at HERA favours the absence of shrinkage of the diffractive peak, but the data are not yet precise enough to allow a final judgement on this question. The intercept and the slope of the measured trajectory are

$$\alpha(t) = (1.26 \pm 0.05) + (0.05 \pm 0.15)\,\mathrm{GeV}^{-2} \cdot t\,, \quad (7.5)$$

  lying in between the two pomeron trajectories of [19]. The measurement prefers slightly the *hard* pomeron solution of Donnachie and Landshoff [19] and the BFKL *hard* pomeron by Brodsky et al. [29] in contrast to the *soft* Donnachie-Landshoff pomeron.

- The elastic $\Upsilon(1S)$ photoproduction cross section is measured averaged over the region $70 \leq W_{\gamma p} \leq 250\,\mathrm{GeV}$ at a mean $\langle W_{\gamma p} \rangle = 143\,\mathrm{GeV}$ to be:

$$\sigma_{\gamma p \to \Upsilon p} = 520 \pm 210 \pm 130\,\mathrm{pb}\,. \quad (7.6)$$

  This measurement is based on the same data as the H1 preliminary measurement from [40], using some additional knowledge gained from the J/ψ analysis as presented here, and is in good agreement with the previous result.

- Comparing the Υ photoproduction cross section measurements with pQCD calculations [39, 43, 44] it is noticeable that the original calculations, which are able to describe the measured J/ψ photo- and electroproduction cross sections in size and $W_{\gamma p}$ and Q^2 dependence [39], fail by about two standard deviations in the case of the Υ photoproduction cross section [39]. This discrepancy triggered a recalculation [43, 44] considering two main effects, namely the skewed parton densities and the real part of the amplitude, which play a more important role than in case of the J/ψ. All three new calculations, obtained with different methods, are in agreement with each other and with the available data points.

Finally, it can be summarized that the measurement of various aspects of elastic J/ψ photoproduction at HERA shows good agreement with calculations in perturbative QCD as well as with results from Regge based models under the ad hoc assumption of a second, a *hard*, pomeron. Based on the energy dependence of the cross section as well as on the favoured energy independence of the slope parameter, a pure *soft* production mechanism for J/ψ mesons at HERA energies can be ruled out.

In figure 7.1 the total photoproduction cross section, σ_{tot}, is shown together with the cross sections of the vector mesons ($\rho, \omega, \phi, J/\psi$ and Υ) in elastic photoproduction, $\sigma(\gamma p \to V p)$, for data from fixed target experiments and from HERA, including the results presented here. While the cross sections decrease at low energies, they rise at higher $W_{\gamma p}$, which can be explained by pomeron exchange.

In the case of the ρ and the φ mesons this rise is measured to be in good agreement with the expectations from the soft pomeron model 2.2.1, $\sigma_{\gamma p} \propto W_{\gamma p}^{0.22}$. It can be seen that in J/ψ photoproduction the cross section rises much more steeply, $\sigma_{\gamma p} \propto W_{\gamma p}^{\sim 0.8}$. At the moment not enough data points are available in the case of the Υ meson, but a strong correlation between the mass of the diffractively produced state and the energy dependence of the cross section is found within the perturbative QCD models [43]. In particular, a considerably stronger rise in energy is predicted for Υ photoproduction ($\sigma \propto W_{\gamma p}^{\sim 1.7}$) than that measured in J/ψ photoproduction ($\sigma \propto W_{\gamma p}^{\sim 0.8}$). The presently available data show good agreement with this expectation.

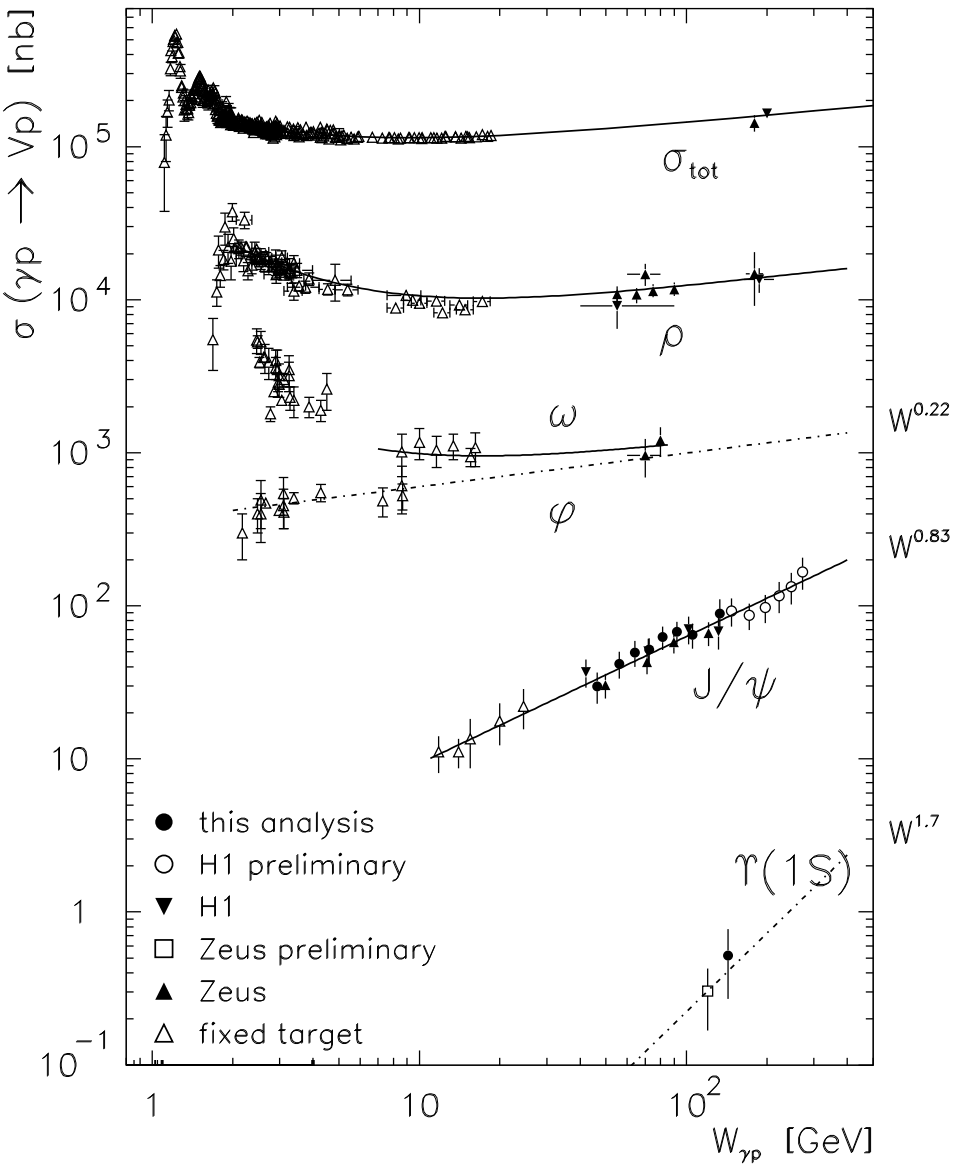

Figure 7.1: Compilation of $\sigma_{\gamma p}^{tot}$ and $\sigma_{\gamma p}$ for various vector mesons. The full lines are fits to the total photoproduction cross section, the elastic ρ, and the elastic φ cross section, using Regge parameterizations and assuming single pomeron exchange [1, 2]. The fit to the J/ψ data is of the form $\sigma_{\gamma p} \propto W_{\gamma p}^{\delta}$, yielding $\delta = 0.83$. The dashed lines visualize a certain energy dependence as indicated on the right hand side.

Appendix A

Detailed Listing of Track Cuts

A.1 Track Selection

A track measured by the H1 tracking system is called a good track if it fulfils one of the following groups of criteria:

Central Tracks:

1. fitted to the primary event vertex,
2. polar angle larger than 20°,
3. the innermost hit is within 44 cm from the beam axis (radial),
4. radial track length larger than 11 cm below 155 ° and larger than 6 cm above,
5. transverse momentum has to be larger than 0.15 GeV,
6. d_{ca} less than 10 cm; d_{ca} is the distance in the $r\varphi$ plane between the vertex and the closest hit assigned to a track.

Forward Tracks:

1. fitted to the primary event vertex,
2. χ^2 of vertex fit less than 50,
3. χ^2 of track fit less than 10,
4. momentum has to be larger than 1 GeV,
5. transverse momentum has to be larger than 0.15 GeV,
6. r_0 less than 10 cm,
7. number of modules for $\vartheta \leq 20^\circ$ is at least 2.

Combined Tracks:

1. fitted to the primary event vertex.

A.2 Muon Track Selection

A track measured by the H1 muon system is called a good track if it fulfils one of the following groups of criteria:

Barrel Tracks:

1. $\rho \leq 100$ cm,
2. at least three layers hit,
3. first layer hit is one of the first five.

Forward Endcap Tracks:

1. $\rho_x \leq 100$ cm,
2. $\rho_y \leq 100$ cm,
3. at least four layers hit,
4. first layer hit is one of the first five.

Backward Endcap Tracks:

1. $\rho_x \leq 100$ cm,
2. $\rho_y \leq 100$ cm,
3. at least three layers hit,
4. first layer hit is one of the first eight.

List of Figures

1.1 Compilation of $\sigma_{\gamma p}^{tot}$ and $\sigma_{\gamma p}$ for various vector mesons prior to the present analysis 3

2.1 Generic graphs for ep collisions 5
2.2 Generic graphs for vector meson production 6
2.3 Reconstruction of kinematic variables 9
2.4 Correlation between $W_{\gamma p}$ and polar angle ϑ_μ 9
2.5 Vector meson production in Regge theory and Vector Meson Dominance 11
2.6 Leading order graph for elastic vector meson production in pQCD based models 14
2.7 Diagram for the exchange of a gluon ladder 18
2.8 Graphs for QED two-photon processes; multi-peripheral 21
2.9 Graphs for QED two-photon processes; Cabibbo-Parisi, Compton-like, Drell-Yan 21

3.1 The storage ring HERA and its pre-accelerators at DESY 23
3.2 Integrated luminosity produced by HERA and measured in H1 (1992-1999) . . 24
3.3 The H1 Detector 25
3.4 The tracking system, side view 26
3.5 The Central Tracking Detector, radial view 27
3.6 The four parts of the Central Muon Detector divided into 64 modules 28
3.7 Schematic structure of the instrumented iron 29
3.8 Schematic side view of the LAr calorimeter 30
3.9 H1 luminosity system 31
3.10 Trigger levels used during 1994 to 1997 data taking 32
3.11 L1 trigger rates for J/ψ triggers 34
3.12 Principle of the z-vertex trigger 35
3.13 Schematic illustration of the L4 scheme 37

3.14 Momentum distribution of decay muons 41
3.15 Schematic illustration of muon identification in the LAr calorimeter 41

4.1 Candidate event for $\gamma p \to J/\psi p, J/\psi \to \mu\mu$ 47
4.2 Candidate event for $\gamma p \to J/\psi Y, J/\psi \to \mu\mu$ 47
4.3 Tagging efficiency of the proton remnant as a function of M_Y 48
4.4 Separation between photoproduction and DIS events 49
4.5 Acceptance in $W_{\gamma p}$ for J/ψ 50
4.6 Distinctive signatures between ep events and cosmic radiation 52
4.7 Diffractive $J/\psi \to \mu\mu$ signal in photoproduction 54
4.8 Comparison between data and Monte Carlo 55
4.9 Trigger element efficiencies, data and Monte Carlo 57
4.10 Muon identification efficiency in the calorimeter in data and Monte Carlo . . . 59
4.11 Muon identification efficiency in the instrumented iron in data and Monte Carlo 59
4.12 Comparison of the response of forward detectors between data and Monte Carlo 61
4.13 Efficiency of the forward tag for elastic and proton dissociative events 62
4.14 Decomposition of the total efficiency in bins of $|t|$ and $W_{\gamma p}$ 63

5.1 Mass spectra in eight $W_{\gamma p}$ bins for forward untagged data 68
5.2 $\sigma(\gamma p \to J/\psi p)$ versus $W_{\gamma p}$, this analysis 73
5.3 $\sigma(\gamma p \to J/\psi p)$ versus $W_{\gamma p}$, all experiments 74
5.4 $\sigma(\gamma p \to J/\psi p)$ versus $W_{\gamma p}$, two-pomeron fit HERA data 75
5.5 $\sigma(\gamma p \to J/\psi p)$ versus $W_{\gamma p}$, two-pomeron fit all data 75
5.6 $\sigma(\gamma p \to J/\psi p)$ versus $W_{\gamma p}$, pQCD model 76
5.7 Purity in bins of $|t|$ 78
5.8 Uncorrected t distributions in bins of $W_{\gamma p}$, background subtraction 79
5.9 $dN/d|t|$ for the whole $W_{\gamma p}$ range, elastic J/ψ 81
5.10 $dN/d|t|$ in five bins of $W_{\gamma p}$ 83
5.11 b as a function of $W_{\gamma p}$, this analysis 84
5.12 b as a function of $W_{\gamma p}$, different analyses 84
5.13 $dN/d|t|$ for the whole $W_{\gamma p}$ range, proton dissociative J/ψ 85
5.14 Forward untagged $J/\psi \to \mu\mu$ signals in the $W_{\gamma p} - |t|$-plane 87

5.15 $d\sigma/dt$ in five bins of $|t|$ 89
5.16 Regge trajectory for $\gamma p \to J/\psi p$ 90

6.1 Acceptance in $W_{\gamma p}$ for Υ 94
6.2 Invariant mass spectra at different stages of the Υ selection 96
6.3 Comparison between data and simulation for the Υ analysis 97
6.4 Invariant mass spectrum for the elastic Υ selection 100
6.5 Invariant mass spectrum for the diffractive Υ selection; all Q^2 100
6.6 Invariant mass spectra as expected from Υ Monte Carlo mixture (10:2:3) 101
6.7 Invariant mass spectra as expected from Υ Monte Carlo mixture (10:1.1:0.6) . . 101
6.8 Comparison of the measured Υ cross section with pQCD calculations 102

7.1 Compilation of $\sigma_{\gamma p}^{tot}$ and $\sigma_{\gamma p}$ for various vector mesons 107

List of Tables

2.1 Effective scales, Q^2_{eff}, for vector meson production 16
2.2 Contribution of the real part of the amplitude for $\Upsilon(1S)$ production 17
2.3 Steering parameters for J/ψ and Υ event simulation 20

3.1 Full definitions of L1 subtriggers 33
3.2 Input quantities for L2 neural nets 36
3.3 Verification of L1 trigger elements on L4 38
3.4 Hard scale selection on L4 39
3.5 Criteria for *good* central tracks with respect to the *high mass finder* 40
3.6 Muon identification criteria 44

4.1 Luminosity used in analysis 49
4.2 Reduction of the data volume by J/ψ selection cuts 53
4.3 Sources of systematic uncertainties on the J/ψ cross section 64

5.1 Summary of the elastic J/ψ cross section 72
5.2 Systematic uncertainties on b 80
5.3 Summary of the elastic slope parameters b in bins of $W_{\gamma p}$ 82
5.4 Choice of bin sizes in the $W_{\gamma p} - |t|$-plane 88

6.1 Overview of the triggers used in the Υ analysis 94
6.2 Reduction of the data volume by Υ selection cuts 95
6.3 Properties of the Υ mesons 95
6.4 Sources of systematic uncertainties on the Υ cross section 98
6.5 Summary of the elastic Υ cross section 102

Bibliography

[1] A. Donnachie, P. V. Landshoff, Phys. Lett. **B 296** (1992) 227.

[2] G. A. Schuler, T. Sjöstrand, Nucl. Phys. **B 407** (1993) 539.

[3] A. Meyer, *Charmonium Production in Deep Inelastic Scattering at HERA*, Dissertation, Hamburg (1998).

[4] J. A. Crittenden, hep-ex/9704009, DESY-97-068, Berlin, Germany: Springer (1997) 100 p.

[5] A. Levy, talk presented at the XXI International Workshop on the Fundamental Problems of High Energy Physics and Field Theory, Protvino (1998).

[6] E. M. Levin, hep-ph/9808486, talk presented at the Workshop of Diffractive Physics, LISHEP'98, Rio de Janeiro (1998).

[7] E. Fermi, Z. Phys. **29** (1924) 315.

[8] C. F. von Weizsäcker, Z. Phys. **88** (1934) 612.

[9] E. J. Williams, Phys. Rev. **45** (1934) 729.

[10] V. M. Budnev, I. F. Ginzburg, G. V. Meledin, V. G. Serbo, Phys. Rep. **15** (1975) 181.

[11] A. Blondel, F. Jacquet, *Proceedings of the Study of an ep Facility for Europe*, DESY, Hamburg, 2.-4. April 1979, DESY Report **79-048** (1979) 377.

[12] T. Regge, Nuovo Cim. **14** No. 5 (1959) 951; T. Regge, Nuovo Cim. **18** (1960) 957.

[13] P. D. B. Collins, *An Introduction to Regge Theory and High Energy Physics*, Cambridge University Press, Cambridge (1977).

[14] H1 Collaboration, C. Adloff et al., Nucl. Phys. **B 497** (1997) 3;
ZEUS Collaboration, J. Breitweg et al., Phys. Lett. **B 407** (1997) 432.

[15] H1 Collaboration, S. Aid et al., Nucl. Phys. **B 472** (1996) 3.

[16] H. Abramowicz, E. M. Levin, A. Levy, U. Maor, Phys. Lett. **B 269** (1991) 465.

[17] A. Donnachie, P. V. Landshoff, Phys. Lett. **B 296** (1992) 227.

[18] A. Donnachie, P. V. Landshoff, Phys. Lett. **B 348** (1995) 213

[19] A. Donnachie, P. V. Landshoff, Phys. Lett. **B 437** (1998) 408.

[20] J. J. Sakurai, Annals Phys. **11** (1960) 1.

[21] J. J. Sakurai, Phys. Rev. Lett. **22** (1969) 981;
J. J. Sakurai, D. Schildknecht, Phys. Lett. **B 40** (1972) 121.

[22] T. H. Bauer, R. D. Spital, D. R. Yennie, F. M. Pipkin, Rev. Mod. Phys. **50** (1978) 261, and references therein; Erratum ibid. **51** (1979) 407.

[23] B. L. Ioffe, Phys. Lett. **B 30** (1969) 123.

[24] J. Hüfner, B. Z. Kopeliovich, *$J/\psi N$ and $\psi(2S)N$ Cross Sections from Photoproduction Data: Failure of Vector Dominance*, Phys. Lett. **B 426** (1998) 154.

[25] G. F. Chew, S. C. Frautschi, Phys. Lett. **7** (1961) 394.

[26] I. I. Pomeranchuk, Sov. Phys. JETP **34 (7)** (1958) 499.

[27] K. Goulianos, Phys. Rep. **101** (1983) 169.

[28] E710 Collaboration, N. Amos et al., Phys. Lett. **B 301** (1993) 313.

[29] S. J Brodsky, V. S. Fadin, V. T. Kim, L. N. Lipatov, G. B. Pivovarov, hep-ph/9901229 (1999).

[30] V. S. Fadin, E. A. Kuraev, L. N. Lipatov, Phys. Lett. **B 60** (1975) 50;
L. N. Lipatov, Sov. J. Nucl. Phys. **23** (1976) 338;
V. S. Fadin, E. A. Kuraev, L. N. Lipatov, Sov. JETP **44** (1976) 443, **45** (1977) 199;
Y. Y. Balitskii, L. N. Lipatov, Sov. J. Nucl. Phys. **28** (1978) 822.

[31] V. S. Fadin, L. N. Lipatov, Phys. Lett. **B 429** (1998) 127;
G. Camici, M. Ciafaloni, Phys. Lett. **B 430** (1998) 349.

[32] S. J. Brodsky, G. P. Lepage, P. B. Mackenzie, Phys. Rev. **D 28** (1983) 228.

[33] M. G. Ryskin, Z. Phys. **C 57** (1993) 89.

[34] NMC Collaboration, D. Allasia et al., Phys. Lett. **B 258** (1991) 493.

[35] E. M. Levin, A. D. Martin, R. G. Roberts, M. G. Ryskin, Z. Phys. **C 76** (1997) 231.

[36] J. C. Collins, D. E. Soper, G. Sterman, Nucl. Phys. **B 308** (1988) 833.

[37] S. J. Brodsky, L. Frankfurt, J. F. Gunion, A. H. Mueller, M. Strikman, Phys. Rev. **D 50** (1994) 3134.

[38] L. Frankfurt, W. Koepf, M. Strikman, Phys. Rev. **D 54** (1996) 319.

[39] L. Frankfurt, W. Koepf, M. Strikman, Phys. Rev. **D 57** (1998) 512.

[40] H1 Collaboration, C. Adloff et al., *Observation of* Υ *Production at HERA*, contributed paper 574 to ICHEP 1998, Vancouver.

[41] ZEUS Collaboration, G. Abbiendi et al., *Measurement of Elastic* Υ *Photoproduction at HERA*, DESY-98-089 (1998).

[42] J. R. Cudell, I. Royen, Nucl. Phys. **B 545** (1999) 505.

[43] L. Frankfurt, M. Strikman, M. McDermott, JHEP **9902** (1999) 2.

[44] A. D. Martin, M. G. Ryskin, T. Teubner, hep-ph/9901420 (1999).

[45] A. Martin, M. G. Ryskin, Phys. Rev. **D 57** (1998) 6692.

[46] *GEANT — Detector Description and Simulation Tool*, CERN Program Library Long Writeup W5013.

[47] B. List, *Diffraktive* J/ψ*-Produktion in Elektron-Proton-Stössen am Speicherring HERA*, Diploma thesis, Techn. Univ. Berlin, unpublished (1993).

[48] R. M. Barnett et al., Phys. Rev. **D 54** (1996) 1.

[49] T. Sjöstrand, Comput. Phys. Commun. **82** (1994) 74.

[50] S. P. Baranov, O. Dünger, H. Shooshtari, J. A. M. Vermaseren, *LPAIR: A Generator for Lepton Pair Production*, in: Physics at HERA, Proceedings of the Workshop, Vol.3, 1478, Hamburg (1991);
O. Dünger, *Untersuchung der Myonpaar-Erzeugung durch Photon-Photon-Kollision am ep-Speicherring HERA*, Dissertation, DESY F11/F22-94-01, Hamburg (1994).

[51] H1 Collaboration, I. Abt et al., Nucl. Instr. and Meth. **A 386** (1997) 310 and Nucl. Instr. and Meth. **A 386** (1997) 348.

[52] U. P. Krüger, *Untersuchung der Erzeugung schwerer Quarks durch ihren Zerfall in Myonen im H1-Detektor bei HERA*, Dissertation, Hamburg (1994).

[53] J. Krepke, *Untersuchung zur Ortsbestimmung von Spuren im H1-Myon-Detektor mit Hilfe der kalorimetrischen Informationen*, Diploma thesis, Hamburg (1994).

[54] H1 Calorimeter Group, B. Andrieu et al., Nucl. Instr. and Meth. **A 344** (1994), 492.

[55] M. Fleischer et al., *Performance and Upgrade of H1 Calorimeters: LAr Calorimeter, SpaCal and VLQ*, DESY Report 98-005 (1998).

[56] H1 SpaCal Group, R. D. Appuhn et al., Nucl. Instr. and Meth. **A 386** (1997), 397.

[57] A. Meyer, *Measurement of the Structure Function* $F_2(x, Q^2)$ *of the Proton at low* Q^2 *with the H1-Detector at HERA Using the New Detector Components Spacal and BDC*, Dissertation, Hamburg (1997).

[58] H1 Collaboration, S. Aid et al., *Luminosity Measurement in the H1 Experiment at HERA*, contributed paper pa17-026 to ICHEP 1996, Warsaw.

[59] H. Bethe, W. Heitler, Proc. Roy. Soc. **A 146** (1934) 83.

[60] R. Prosi, *The 1994 L4 Filter Farm Selection Algorithm*, Internal H1 Note H1-03/95-433 (1995).

[61] K. Müller, R. Beyer, *1996 L4 Filter Farm Selection Algorithm*, Internal H1 information (1996).

[62] S. Mohrdieck, private communication (1998).

[63] A. Schwank, *Effizienzbestimmung von Detektorkomponenten des H1-Experiments mit Hilfe kosmischer Strahlung*, Diploma thesis, Hamburg (1998).

[64] G. Schmidt, *Untersuchung der diffraktiven Photoproduktion von J/ψ-Mesonen im H1-Detektor bei HERA*, Dissertation, Hamburg (1997).

[65] S. Schiek, *Untersuchung der inelastischen Photoproduktion von J/ψ-Mesonen im H1-Detektor bei HERA*, Dissertation, Hamburg (1997).

[66] B. Naroska, S. Schiek, G. Schmidt, *Lepton Identification in the H1 Detector at Low Momenta*, Internal H1 Note H1-05/97-518 (1997).

[67] C. Caso et al., Review of Particle Physics Volume 3, 1-4 (1998).

[68] S. Levonian, H1 internal information (1997).

[69] H1 Collaboration, C. Adloff et al., Phys. Lett. **B 421** (1998) 385.

[70] H1 Collaboration, S. Aid et al., Nucl. Phys. **B 468** (1996) 3.

[71] H1 Collaboration, C. Adloff et al., *Charmonium Production in Deep Inelastic Scattering at HERA*, submitted to Europ. Journal f. Phys. (1999).

[72] A. Meyer, private communication (1999).

[73] ZEUS Collaboration, J. Breitweg et al., Z. Phys. **C 75** (1997) 215.

[74] H1 Collaboration, C. Adloff et al., *Energy Dependence of the Cross-Section for the Exclusive Photo-Production of J/ψ Mesons at HERA*, contributed paper 572 to ICHEP 1998, Vancouver.

[75] H1 Collaboration, C. Adloff et al., *Elastic Production of J/ψ Mesons in Photoproduction and at High Q^2 at HERA*, contributed paper 242 to HEP 1997, Jerusalem.

[76] E516 Collaboration, B. H. Denby et al., Phys. Rev. Lett. **52** (1984) 795.

[77] E401 Collaboration, M. Binkley et al., Phys. Rev. Lett. **48** (1982) 73.

[78] H1 Collaboration, C. Adloff et al., *Shrinkage in Exclusive J/ψ Photoproduction*, contributed paper 572 to ICHEP 1998, Vancouver.

[79] M. Glück, E. Reya, A. Vogt, Z. Phys. **C 67** (1995) 433.

[80] A. D. Martin, R. G. Roberts, W. J. Stirling, Phys. Lett. **B 387** (1996) 419.

[81] H. L. Lai et al., Phys. Rev. **D 55** (1997) 1280.

[82] H1 Collaboration, C. Adloff et al., *Production of J/ψ mesons with large $|t|$ at HERA*, contributed paper 274 to HEP 1997, Jerusalem.

[83] A. Levy, Phys. Lett. **B 424** (1998) 191.

[84] J. Nemchik, N. N. Nikolaev, E. Predazzi, B. G. Zakharov, V. R. Zoller, Phys. Lett. **B 374** (1996) 199.

[85] CDF Collaboration, F. Abe et al., Phys. Rev. Lett. **75** (1995) 4358.

[86] P. Merkel, *Diffractive Heavy Vector Meson Photoproduction at HERA*, in: Proceedings of the EPS-HEP99, Tampere (1999), to be published.

Danke

Mein Dank gilt allen Menschen bei H1, die mit ihren Diskussionen, Anregungen und ihrer Hilfsbereitschaft zum Gelingen dieser Arbeit beigetragen haben. Ein besonderes Dankeschön geht dabei an Frau Beate Naroska, deren unermüdliche Aufmerksamkeit, beständiges Nachbohren und Aufspüren all derjenigen Schwachstellen, die ich selbst am liebsten ignoriert hätte, meine Arbeit am DESY erst richtig interessant gemacht haben.

Vor allem aber möchte ich mich bei meiner Familie und allen Freunden bedanken, die mit großer Geduld und viel Erfindungsgabe das triste Forscherleben abwechslungsreich aufgelockert und begleitet haben.